Quantum and Semiclassical Scattering Matrix Theory for Atomic Photoabsorption in External Fields

by

Brian Ellison Granger

B.S., Westmont College, 1994

A thesis submitted to the

Faculty of the Graduate School of the

University of Colorado in partial fulfillment

of the requirements for the degree of

Doctor of Philosophy

Department of Physics

2001

This thesis entitled:
Quantum and Semiclassical Scattering Matrix Theory for Atomic Photoabsorption in External Fields
written by Brian Ellison Granger
has been approved for the Department of Physics

Chris H. Greene

John R. Cary

Date

The final copy of this thesis has been examined by the signatories, and we find that both the content and the form meet acceptable presentation standards of scholarly work in the above mentioned discipline.

Granger, Brian Ellison (Ph.D., Physics)

Quantum and Semiclassical Scattering Matrix Theory for Atomic Photoabsorption in External Fields

Thesis directed by Professor Chris H. Greene

The photoabsorption spectra of Rydberg atoms in static, external electric and magnetic fields provide an excellent opportunity to study the properties of a nonintegrable physical system. This thesis develops a general theory for predicting and interpreting the photoabsorption spectra of these systems. Using ideas from both quantum-defect theory and semiclassical approximations, such as closed-orbit theory, I introduce scattering matrices to describe the final state of an electron in a photoabsorption experiment. The scattering matrices encapsulate all of the important physics of the system, and are related to important observables of the system, such as the bound state spectrum and the photoabsorption cross section.

Initially, the framework for calculating the photoabsorption cross section is presented in complete generality. An exact expression for the energy smoothed photoabsorption cross section is derived and is shown to provide a useful link between quantum-defect theory and semiclassical approximations. Although the formula is an exact result, it already contains many of the physical insights of semiclassical approximations about the time (or action) domain physics of the electron. Both the complications of multielectron atoms and arbitrary configurations of static, electromagnetic fields are included in the theory.

After the basic framework has been developed, semiclassical approximations are introduced for the specific case of an alkali-metal atom in an external magnetic field. I derive a semiclassical S-matrix to describe the scattering of the electron off the combined Coulomb and diamagnetic long-range potentials. The relationship of the semiclassical approximation to accurate quantum calculations is then explored.

Finally, the semiclassical S-matrix is used to construct a semiclassical formula for the photoabsorption cross section. Here, the focus is on the Fourier transformed cross section, or recurrence spectrum, which shows sharp peaks that correspond to certain quantum mechanical paths of the electron as it scatters off the long-range potentials. The semiclassical approximation of the cross section interprets

these quantum paths by correlating them with classical closed orbits of the electron. By taking a surprising cancellation between ghost and core-scattered orbits into account, a resumed semiclassical cross section is derived. This formula gives a convergent, semiclassical theory for the recurrence spectra of nonhydrogenic atoms. Results are presented for diamagnetic lithium and rubidium.

Dedication

To my family with love.

Acknowledgements

Like most things in life, this thesis could not have been completed without the encouragement and support of many people. I want to graciously thank everyone who has been a part of my experience of physics in graduate school.

Most importantly, my advisor, Chris Greene, has been a wonderful teacher and mentor to me. When I began in the group, Chris was bold enough to let me begin a project in an area of atomic theory that was new for both of us. I have appreciated his patience as I have struggled to learn the often tricky semiclassical methods used throughout this thesis. This patience has been a great gift to me and has allowed me to learn the methods well. At the same time, Chris has taught me to think about problems in physics using the ideas and tools of quantum-defect theory. From the beginning, Chris was convinced that semiclassical approximations were closely related to the scattering matrices of quantum-defect theory. This perspective has informed all of the work in this thesis. Most of all, I appreciate Chris's love of theoretical physics. This enthusiasm has rubbed off on me and has made my time in his group completely enjoyable.

I tend to learn physics best by talking with others. This has made the presence of the other members of Chris's group invaluable. Early on, Hugo van der Hart spent many hours teaching me about B-splines and R-matrix theory. In the past few years, I have appreciated many conversations with Edward Hamilton and Dörte Blume as well. In addition, from the day I arrived in Boulder, Fernando Perez has encouraged me towards theoretical physics and a strong life of the mind.

John Delos and his students and postdocs have also been a wonderful resource in this project. At first, the original articles of Du and Delos provided my primary training in semiclassical methods. Since

then I have had numerous enlightening discussions with John about semiclassical physics.

I also want to thank Pam Leland, who was helpful in proofreading the final manuscript.

This research was completed through a grant from the Department of Energy, Office of Basic Energy Sciences.

Contents

List of Figures

Figure

Chapter 1

Introduction

This thesis is concerned with a class of nonintegrable systems from atomic physics: atoms in static, external electromagnetic fields. These systems present a challenge not found in their integrable[1] or near-integrable counterparts, such as the hydrogen atom or the low lying states of atoms and molecules. To illustrate the difficulty with nonintegrable systems I wish to imagine a dialogue between a diligent graduate student and her advisor. The graduate student has been hard at work in the lab taking photoabsorption spectra of an atom having a nonintegrable Hamiltonian. After months of building electronics and tweaking lasers, the graduate student has scans of a region of the spectrum with an excellent signal to noise ratio. The advisor enters the lab to see the new results.

"Yes, I received your email and I wanted to see some of the spectra you have taken."

"Of course," replies the graduate student, as she pulls out the lab notebook containing the newly obtained scans. "Here is the region from 109,700 to 109,900 wavenumbers. At first I thought the spectrum was all noise, but I have repeated the experiment over the same range three times and all of the features are reproducible."

Slightly skeptical, the advisor puts on his eyeglasses to take a closer look at the different scans.

"Wow, they do look identical. I guess after all of the work you have done these might be real absorption peaks."

Pleased by her advisor's confidence, the student replies, "I think they are."

It now becomes clear that the advisor is thinking about the physics of the spectrum. "You have

[1] A quantum system with N degrees of freedom is integrable if there exist N independent operators $\hat{A}_i$ that commute with the Hamiltonian and with each other. This set of operators is sometimes referred to as a "complete set of commuting observables."

been doing a literature search on this system, right? What do we know about this large absorption peak?"

"Which one?" asks the student.

"This one right here that stands out so strongly. You would think this peak would show up in the lower resolution experiments that have been performed previously."

"Oh, yes, I did find this article that mentions a large peak at that energy . . . at about 109793.5 wavenumbers."

Encouraged, the advisor inquires further, "well then what do we know about it?"

With a puzzled look the student hesitates "well . . . uhh . . . it is at that energy there, and it's that high."

"Well obviously, I can see that, but what else do we know?"

The student knows that she should say something, so she stretches, "um . . . it is right next to those two peaks?"

Just as the student is beginning to doubt the reliability of both her literature search and the experimental data, the advisor gets a light in his eye and proclaims,

"Oh, of course, you are right, that's all there is to know about that peak. This system is nonintegrable!"

The point of this dialogue is to emphasize that the only good quantum number of a strongly nonintegrable, autonomous system is its energy. This is in contrast to an integrable or partially integrable system, which has one or more good quantum numbers other than the energy. It is well known [1] that every good quantum number corresponds to a symmetry of the Hamiltonian. Each time a symmetry of a system is strongly broken, the quantum number associated with the symmetry is no longer useful for describing the eigenstates of the system. What is often not appreciated is that the quantum numbers of an eigenstate give us an intuitive picture of the physics of the state. Given the quantum numbers, we immediately have access to information about the nodal structure of the wavefunction and other issues such as degeneracies. Thus, quantum numbers are one of the main ways that we "see" quantum mechanical states. The main difficulty in nonintegrable systems is then in our ability to gain an intuitive picture of the quantum mechanics.

Perhaps the biggest advance towards understanding the quantum mechanics of multi-dimensional, nonintegrable systems has been the development of semiclassical approximations for the solutions of the Schrödinger equation. This is demonstrated in the following brief history of the study of atoms in strong magnetic fields, or diamagnetic atoms.

1.1 Historical background

At the beginning of the 20th century, the newly discovered quantum mechanics diverged from classical mechanics. As Einstein [2] and others realized, quantization using classical trajectories quickly ran into difficulties in multidimensional, nonintegrable systems. The invariant tori used to quantize integrable systems begin to break down as integrability is lost. While the WKB [3] quantization procedure for one dimensional systems and the multidimensional extension for integrable systems (EBK) [2, 4, 5, 6] had limited success, no such semiclassical quantization procedure could be found for nonintegrable systems.

To some extent, the status of nonintegrable systems in quantum mechanics at this point in history is not surprising. A similar impasse existed for nonintegrable classical systems. The difficulties for the classical case were elucidated by the work of Henry Poincaré [7]. The issue at the time was the prediction of the long time behavior of the solar system. Poincaré showed, to the dismay of many, that all classical perturbative expansions of the motion of the solar system contain irremovable singularities due to resonances. Without the benefits of modern computational power, Poincare's theorem shattered the only available method of solution. At the level of both quantum mechanics and classical mechanics, progress on the understanding of nonintegrable systems slowed drastically for about fifty years.

In the 1950s and 1960s, work by Kolmogorov [8], Arnol'd [9, 10] and Moser [11] began to illuminate the nature of classical nonintegrability. The results of their work, known as the KAM theorem [12], gives a detailed account of exactly how the invariant tori in phase space break up as symmetries are broken. Also, beginning with the work of Edward Lorenz [13], computers began to give dramatic new insights into the nature of strongly nonintegrable classical systems. Essentially, classical chaos has been discovered. The breakup of invariant tori into finer and finer phase space structures could now be studied

in detail. It was seen that the invariant structures in the phase space of chaotic systems - periodic orbits - occupied infinitesimally small volumes of phase space. This seemed incompatible with one of the main ideas of quantum mechanics: that phase space volumes are limited by the fundamental constant $\hbar$ through the Heisenberg uncertainty principle. However, as classical chaos was studied more thoroughly in the 1960s and 1970s, it was realized that semiclassical quantization of classically chaotic systems might be possible after all. The major breakthrough came with the work of Balian, Bloch and Gutzwiller. Balian and Bloch [14, 15, 16, 17] showed that oscillations in the density of states of electromagnetic cavities and quantum billiards could be understood in terms of classical periodic orbits. Gutzwiller [18, 19, 20, 21] elaborated on this idea through his derivation of a "trace formula" for the quantum density of states of a smooth nonintegrable Hamiltonian. With Gutzwiller's derivation, classical mechanics reentered the realm of quantum mechanics for good.

Gutzwiller's semiclassical trace formula for the quantum density of states introduced a new way of looking at the spectrum of Hamiltonians having chaotic classical dynamics. Excellent discussions of the trace formula can be found in [22, 23, 24]. In his approach, the density of states is broken up into a smooth, average part $\tilde{g}(E)$, and an oscillating part $\delta g(E)$:

$$g(E) = \sum_n \delta(E - E_n) = \tilde{g}(E) + \delta g(E). \tag{1.1}$$

The famous trace formula,

$$\delta g(E) = \frac{1}{\hbar\pi} \sum_{po} \frac{T_{po}}{\sqrt{\det(\tilde{M}_{po} - 1)}} \cos\left(\frac{1}{\hbar} S_{po}(E) - \sigma_{po} \frac{\pi}{2}\right), \tag{1.2}$$

gives a relationship between the oscillating part of the density of states $\delta g(E)$ and the classical periodic orbits of the system in the limit $S_{po} \gg \hbar$. These **periodic orbits** are solutions of the classical equations of motion that return to an initial point in phase space after a period T_{po}. On the right side of Eq. (1.2), the properties (action $S_{po,}$ Maslov index σ_{po}, and stability matrix $\tilde{M}_{po}$) of these purely classical orbits are seen to provide all of the information about the quantum mechanical density of states. The only signature of the quantum world on the right side of Eq. (1.2) is the appearance of the constant $\hbar$. Although a similar trace formula for integrable systems has been derived by Berry [25, 26], the result of Gutzwiller applies to chaotic systems where the periodic orbits are well isolated in phase space.

The physics in the trace formula (1.2) is manifested when the delta functions $\delta(E - E_n)$ in the exact density of states (1.1) are smoothed over using some convolution function of width ΔE. The resulting smoothed density of states shows dramatic oscillations with energy. The great advance of the trace formula (1.2) is to allow the interpretation of these oscillations in terms of the classical periodic orbits having $T_{po} < \frac{2\pi\hbar}{\Delta E}$. Thus, entire sequences of energy smoothed eigenstates of nonintegrable Hamiltonians can be interpreted with only a few classical periodic orbits of the corresponding classical system. This represents a huge improvement over interpreting the density of states by saying "this eigenstate has an energy of . . . and it is next to this one, this one and this one."

Atoms in external magnetic fields represent one of the most important examples of this type of analysis. The experiments of Garton and Tomkins [27, 28, 29] were the first to show interesting new physics in the spectra of diamagnetic atoms. Their major discovery was that the near threshold photoabsorption spectra of atoms in strong (0-6 Tesla) magnetic fields show dramatic oscillations with energy, which are independent of the atom being studied. The large spacing of these "quasi-Landau" resonances $\frac{3}{2}\hbar B$ (B is the magnetic fields in a.u.), as Edmonds [30] and Starace [31] elucidated, is related to a classical orbit of the Rydberg electron having period $\frac{2}{3}\left(\frac{2\pi}{\hbar B}\right)$. This classical orbit, the quasi-Landau orbit, begins at the nucleus, travels out perpendicularly to the magnetic field and returns to the nucleus after deflecting off the magnetic field. It is ironic that the observation of these global oscillations depended critically on the poor resolution of the experimental spectrum; high resolution spectra recorded later (see [32] for example), when experimental methods improved, show dense sequences of seemingly random absorption lines.

Soon thereafter, experiment and theory showed that the quasi-Landau oscillations were merely the tip of the iceberg. Higher resolution experiments on hydrogen in a 5.96 Tesla field [33, 34, 35] revealed the contributions of additional, longer period classical orbits of the highly excited electron. This experimental work by Welge's group in Bielefeld, Germany demonstrated that the contribution of each such orbit to the photoabsorption cross section could be extracted by taking the Fourier transform of the experimental spectrum. The resulting **recurrence spectrum** shows strong peaks in the time domain at the periods of these newly uncovered classical orbits. A quantitative theory of the recurrence spectrum

was first provided by Du and Delos[2] [37, 38]. This theory and its extensions are known as **closed-orbit theory**.

Closed-orbit theory echoes many of the ideas of Gutzwiller's trace formula (1.2). Like the trace formula for the density of states, the photoabsorption cross section $\sigma(E)$ in closed-orbit theory [38] is written in terms of an average part $\tilde{\sigma}(E)$ and an oscillating part $\delta\sigma(E)$:

$$\sigma(E) = \tilde{\sigma}(E) + \delta\sigma(E). \tag{1.3}$$

Using semiclassical wavefunctions away from the nucleus, Du and Delos showed that the oscillating part of the photoabsorption cross section[3] can be written as a sum over the closed classical orbits of the atomic electron in an external field:

$$\delta\sigma(E) = 8\pi^2\alpha\omega \sum_{co} A_{co} \cos\left(S_{co} - \sigma_{co}\frac{\pi}{2} + \frac{3\pi}{4}\right). \qquad (a.u.) \tag{1.4}$$

As in the trace formula (1.2), the phase of each oscillating term is determined by the classical action S_{co} and Maslov index σ_{co} of each closed orbit. The amplitude A_{co} involves both properties of the classical orbit of the electron (its classical stability and initial and final polar angles) along with properties of the initial quantum state of the atom (dipole matrix elements). The **closed orbits** that determine the physics of $\delta\sigma(E)$ in a semiclassical approximation are classical trajectories of the Rydberg electron that are launched radially outward from the nucleus, scatter off the long range Coulomb and magnetic field and then return radially to the nucleus. Closed orbits, rather than periodic orbits, are relevant in photoabsorption experiments because the initial atomic state is strongly localized near the nucleus.

For light atoms in external magnetic and electric fields, closed-orbit theory has proven to be a quantitative and elegant method of calculating and interpreting recurrence spectra. Over the past two decades, multiple generations of experiments have measured the recurrence spectra of hydrogen [39], lithium [40] and helium [41, 42, 43, 44, 45] in strong magnetic fields. Almost universally, the agreement of these experiments with the predictions of closed-orbit theory has been spectacular; both the location and amplitude of recurrence peaks are predicted to within a few percent. In addition, the closed orbits

[2] A similar treatment was developed simultaneously by Bogomolny [36] although his approach has not received as much attention.

[3] Practitioners of closed-orbit theory often use an oscillator-strength density $Df(E)$ instead of the atomic absorption cross section. The two are related by the formula $\sigma(E) = 2\pi^2\alpha D f(E)$.

underlying each recurrence peak provide a simple interpretation of the time domain physics. Similar agreement is shown in the Stark recurrence spectra of these light atoms subjected to a static electric field [46, 47, 48, 49]. To achieve this level of agreement with experiment, two extensions of closed-orbit theory have been necessary.

First, the effects of a nonhydrogenic ionic core have been included. Following quantum-defect theory [50], the electron-core interactions are characterized by a set of energy independent quantum defects. When combined with semiclassical wavefunctions away from the core [51, 38], these quantum defects permit an extension of closed-orbit theory to single-channel atoms. Such results, obtained by Dando *et al.* [52, 53] and by Shaw and Robicheaux [52, 53, 54], predict the emergence of new recurrence peaks, called core-scattered recurrences, when the quantum defects are turned on (see also [55]). These appear as a result of one primitive closed orbit of period T_1 scattering into another of period T_2 to produce a new peak at the combined period $T_1 + T_2$. For helium [56, 45] and lithium [40], experiments have confirmed the existence of these nonclassical core-scattered features.

Second, artificial divergences associated with bifurcations of closed orbits have been regularized to give a uniform semiclassical approximation [57, 58, 59]. As the external field strength or the energy of the Rydberg electron is increased, bifurcations of the closed orbits occur [39]. These bifurcations cause well known divergences in the semiclassical amplitude A_{co} in Eq. (1.4) at the points where new orbits come into existence . This effect is unphysical as the exact quantum recurrence spectrum is finite everywhere. Delos and coworkers [60, 61] have used normal form theory to investigate the basic types of bifurcations present in diamagnetic atoms. Because each type of bifurcation has a different topology in phase space, a general, uniform semiclassical theory has proven difficult. In spite of this, some progress has been made. Gao and Delos [62] have given a uniform approximation for the bifurcations of certain classes of orbits in an external electric field; those parallel to the field, the “uphill” and “downhill” orbits. Using these results, Shaw and Robicheaux [54] have given the most promising generalization of closed-orbit theory to date, which incorporates both bifurcations and core-scattering for Stark recurrence spectra. The validity of their formulation has been verified by accurate quantum calculations and a recent experiment [49]. For the case of atoms in magnetic fields, the only work on a uniform semiclassical

treatment has been by Main and Wunner [63]. While suggestive, their approach contains additional unphysical divergences below the bifurcation points that must be dealt with (i.e. canceled by hand or ignored). Additionally, their theory has not yet been tested critically. Thus, while there have been some spectacular successes in regularizing bifurcations in closed-orbit theory, much work remains to be performed in this area. For the most part, however, the inclusion of core-scattering and bifurcations into closed-orbit theory enables the prediction of recurrence spectra of light atoms.

Heavier atoms, however, have proven difficult for closed-orbit theory. Thus far, the success of closed-orbit theory has been limited to atoms with at most two nonzero quantum defects. Recent experiments on barium [64, 65, 66] and argon [67] in electric fields show dramatic differences from the predictions of closed-orbit theory. Even when the core-scattering effects described above are included for these atoms, agreement remains dismal. Furthermore, it appears that the presence of three nonzero quantum defects (as in rubidium) causes the expansions of Dando *et al.* [53] and Shaw and Robicheaux [54], which work beautifully for helium and lithium, to diverge. Thus, the presence of multichannel ionic cores and multiple ionization thresholds seem to present a fundamental difficulty for semiclassical approaches.

The difficulty then is the short range interaction between the Rydberg electron and a multichannel positive ion. This is somewhat ironic given the success of multichannel quantum-defect theory [68] in treating this physics. Since its introduction by Seaton [50] in the 1950s, multichannel quantum-defect theory (MQDT) has become one of the mainstays of modern atomic theory. In MQDT, the quantum defects are generalized into a short-range scattering matrix $\underline{S}^{\mathrm{core}}$, which fully characterizes the scattering of the Rydberg electron from the ionic core. The multiple ionization thresholds and inelastic electron-ion scattering characteristic of complex atoms are all handled accurately and elegantly in this fully quantum-mechanical approach. However, because MQDT requires a simple long range potential, a new approach must be found when external fields destroy the simplicity of the electron's motion far from the nucleus.

Thus, there exists a dilemma in the theory of atoms in static, external magnetic and electric fields. While semiclassical methods, such as closed-orbit theory, provide an efficient and elegant way of treating the motion of a Rydberg electron far from the nucleus, they fail when the electron is within a few

Bohr radii of the ionic core of a multichannel atom. On the other hand, quantum-defect theory handles this short range physics without difficulty - but only when the long range physics is integrable. An understanding of multichannel atoms in nonintegrable configurations of external electric and magnetic fields requires that both the short range and long range physics of the Rydberg electron are treated accurately.

One way out of the difficulties (core-scattering, bifurcations) involved in semiclassical approximations is to solve the Schrödinger equation exactly. This approach has been taken by a number of researchers [69, 70, 71, 72, 73, 74] and is important to mention. These methods, which involve large scale quantum-mechanical calculations, have progressed through a combination of increased computer power and efficient algorithms for solving the Schrödinger equation. Typically, a variational approach such as R-matrix theory, along with an expansion of the wavefunction in a basis set (B-splines, Sturmians, finite elements), is used to convert the multidimensional Schrödinger equation to a matrix diagonalization or else to the solution of an inhomogeneous linear system of equations. Accurate recurrence spectra have been calculated for atoms in strong magnetic fields (1-10000 Tesla) using these techniques and show excellent agreement with experiments [32, 43, 44]. Successful applications to date include a number of single channel atoms in magnetic fields, such as the alkali-metal atoms [71, 74, 72, 75], and Ba and Sr [71, 76, 77] at their lowest thresholds. Similar calculations have been performed for multichannel atoms molecules in electric fields [78, 79, 80, 81, 82] using the methods of Harmin [83] and Fano [84]. Here, the long range physics is simpler than the magnetic field case because motion of the Rydberg electron in the combined Coulomb and electric fields is separable in parabolic coordinates.

While these fully quantum mechanical approaches accurately predict the recurrence spectra of many atoms in external magnetic and electric fields, their usefulness remains limited. Unlike closed-orbit theory, exact quantum calculations struggle to yield physical insight into the spectra they provide. We can **predict** the spectra, but the development of qualitative understanding is difficult or seemingly impossible using fully quantum approaches. For integrable systems, this difficulty is overcome by labeling the quantum states with quantum numbers. However, as I have emphasized in this Introduction, quantum number other than “energy” are useless in strongly nonintegrable systems such as atoms in magnetic

fields. Thus, as experiments begin to probe multichannel atoms in external fields, interpretation of the photoabsorption spectra remains the most difficult issue. Examples of this difficulty are provided by recent experiments on Ba [65, 66] and Ar [67] in electric fields, where simple features in the recurrence spectra remain uninterpreted to a large degree.

1.2 Outline of the results

In this thesis I develop a unified theory of complex atoms in external electric and magnetic fields. Using the ideas and methods from both multichannel quantum-defect theory and closed-orbit theory, I describe a complete picture of the photoabsorption process. In such a process, the atomic electron is moved from an initial state $|\psi_0\rangle$ at energy E_0 to a final state $|\psi_f\rangle$ having energy $E = E_0 + \hbar\omega$, after absorbing a photon of frequency ω. Determining the final state wavefunction $|\psi_f\rangle$, is the main task in any calculation of the photoabsorption cross section. In this thesis, I obtain this final state in a roundabout manner. As quantum-defect theory shows, all of the information contained in the quantum state $|\psi_f\rangle$ can be repackaged into one or more scattering matrices. This reformulation of the electron's final state leads to a simple physical picture of the electron's motion. Because every derivation and formula contained in this thesis relies on this physical picture, it is useful to present the picture here:

The state reached by an atomic electron in a photoabsorption experiment is a combination of two time-independent scattering processes. In the first, the electron is launched outward from the nucleus, scatters off the long range fields, and then returns to the nucleus. In the second, the electron travels inward to scatter off the residual ionic core.

Chapters 2 and 3 present this physical picture and a mathematical description that applies to any atom in any configuration of static external electric and magnetic fields. After reviewing the important elements of quantum-defect theory, I introduce two scattering (or S) matrices: one for the scattering of the electron off the long range fields $\underline{S}^{\mathrm{LR}}$, and another for the short range electron-core scattering $\underline{S}^{\mathrm{core}}$. These two scattering matrices completely determine the Rydberg electron's bound state energy eigenvalues. I derive both a quantization condition and a normalization condition for the bound states in terms of the S-matrices. The result is a completely general method for quantizing multichannel atoms

in external fields. Connections with previous treatments such as Harmin's theory of the Stark effect, and Bogomolny's semiclassical quantization scheme are elucidated.

In Ch. 3 a relationship between the S-matrices and the total photoabsorption cross section is derived. Rather than focusing on the infinite resolution spectra, I smooth over the details of individual absorption lines and explore the energy-smoothed spectrum instead. This approach is inspired by the results of closed-orbit theory, and shows that an exact quantum mechanical generalization of closed-orbit theory can be derived in terms of S-matrices. In addition, the result also connects with familiar formulas of quantum-defect theory. The final formula for the photoabsorption cross section, while still an exact quantum-mechanical result, contains much of the physical insight of semiclassical methods like closed-orbit theory. Again, I emphasize that the results of Chs. 2 and 3 are completely general, applying to any atom in any configuration of external electromagnetic fields. Beginning with Ch. 4, however, I specialize to the case of single channel atoms in external magnetic fields. While multichannel atoms can, in principle, be included into my formulation of the photoabsorption process, a number of subtle features about single channel atoms must be understood first.

Chapters 4 and 5 give the details of how the long-range scattering matrix $\underline{S}^{\mathrm{LR}}$ can be calculated in a either a fully quantum mechanical or semiclassical framework. First, In Ch. 4, the methods of variational R-matrix theory are extended to calculate an accurate quantum $\underline{S}^{\mathrm{LR}}$. While these calculations are based on familiar techniques in atomic theory, a few extensions are needed. The most significant of these is the analytic continuation of the long-range S-matrix to complex energies. This is needed to produce the energy smoothed cross section of Ch. 3 and can be accomplished within the framework of R-matrix theory without difficulty. I end Ch. 4 by presenting calculations for an atom in a static magnetic field that implement the methods of the chapter. These calculations show that the long-range S-matrix can be analyzed in the spirit of closed-orbit theory by taking the Fourier transform, or recurrence strength, of its matrix elements. This allows the detection of nonclassical paths, or ghost orbits, of the electron as it scatters off the long-range fields.

In Ch. 5, I introduce semiclassical approximations into my S-matrix theory of photoabsorption. More specifically, I use a semiclassical Green's function to derive a semiclassical long-range S-matrix

for the motion of an atomic electron in a static magnetic field. By writing $\underline{S}^{\mathrm{LR}}$ as matrix elements of an energy domain Green's function, a versatile approach for deriving semiclassical approximations to the S-matrix is achieved. This treatment allows a detailed study of how the closed-orbits are selected to contribute to the recurrence spectra. The generality of my method is demonstrated as it is used to treat a number of special cases where the primitive semiclassical approximation fails, such as near the bifurcations of closed orbits. My results both reproduce and extend the usual treatment of closed-orbit theory.

Chapter 6 uses the semiclassical S-matrices of Ch. 5 and the preconvolved photoabsorption cross section of Ch. 3 to develop a semiclassical theory for the photoabsorption rate. After the failure of a naive approach to the semiclassical approximation is outlined, I use accurate quantum S-matrices to uncover an important relationship between core-scattered orbits, and other nonclassical orbits called ghost orbits. When this relationship is put into mathematical terms, an improved, resummed semiclassical theory can be developed. In contrast to previous semiclassical theories for nonhydrogenic atoms, my result is generally convergent when more than one quantum defect is large. After deriving the final result, it is applied to a number of test cases, including lithium and rubidium in an external magnetic field.

Atomic units ($e = m = \hbar = 1$, $c = 137$) will be used throughout this dissertation unless otherwise stated. One atomic unit of magnetic field is equal to 2.35×10^5 Tesla.

1.3 Scaled variable recurrence spectroscopy

One of the most significant techniques in the study of atoms in external electric and magnetic fields is the use of so-called scaled variables. Because I will use these scaled variables throughout this thesis, their main features are summarized here. A detailed description for the case of hydrogen in static magnetic field can be found in Appendix A.

In standard spectroscopy, cross sections are measured or calculated as a function of the energy E. When an external electromagnetic field is applied to the system under consideration, the field strength is typically held constant while the energy is varied. In this Introduction, I have described how the global features in the energy domain cross section $\sigma(E)$ can be extracted by Fourier transforming the cross

section to the time domain. The resulting recurrence spectra $\sigma(T)$ shows peaks at the periods T_k of certain classical orbits of the system. The main difficulty with this approach is that the classical periods depend on the energy $T_k = T_k(E)$. Thus, even though the Fourier transformed spectrum shows peaks at the periods T_k, the peaks are somewhat washed out by the energy varying timescales of the system.

A beautiful alternative to this approach was first introduced by Welge's group and has become known as **scaled variable recurrence spectroscopy**. Here, instead of varying only the energy E while recording the spectrum, both the energy E and magnetic field B are varied, while holding the scaled energy $\epsilon = EB^{-2/3}$ fixed. The resulting photoabsorption cross section $\sigma(w)$ becomes a function of the scaled magnetic field $w = 2\pi B^{-1/3}$. The advantage of this approach is that the classical periods T_k are replaced by the scaled actions $\tilde{S}_k$ of the classical trajectories, which depend only on the scaled energy ϵ. This can be seen in the thorough exploration of the scaling properties of the classical Hamiltonian found in Appendix A.

It is also seen that the Fourier domain of the variable w is the scaled action $\tilde{S}$. Thus, when the scaled cross section $\sigma(w)$ is Fourier transformed, the resulting scaled recurrence spectrum $\sigma(\tilde{S})$ shows sharp peaks at the scaled actions $\tilde{S}_k$ of the classical orbits. Because the scaled actions themselves do not depend on w, a clean Fourier transformation can be obtained and detailed studies of the scaled action domain physics can be performed. In addition, only a single set of classical orbits (a single value of ϵ) needs to be considered when interpreting or calculating the recurrence spectrum $\sigma(\tilde{S})$.

Other than in the first few experiments on atoms in magnetic fields these scaled variables have been used almost exclusively rather than the physical energy and magnetic field strength (E, B). I follow this usage of scaled variables in this thesis. For the reader unfamiliar with scaled variables I offer a few rules of thumb for thinking about the "scaled" physics of an atomic electron in an external magnetic field. First, the scaled energy ϵ is completely responsible for determining the qualitative features of the electron's motion. As ϵ increases from $-\infty$ to zero, both the classical and quantum Hamiltonians go from being fully integrable (only a Coulomb potential) to being strongly nonintegrable in two dimensions (Coulomb + magnetic field). Second, the scaled magnetic field w functions as the "energy"-like variable when the photoabsorption cross section is measured. The reader is encouraged to ignore the fact that

w is called the "scaled magnetic field" when attempting to gain insight about the qualitative meaning of the scaled variables. Third, the scaled action $\tilde{S}$ becomes the "time"-like variable used to analyze the recurrence spectrum. These general ideas should ease the transition to thinking in terms of scaled variables. Appendix A can be consulted for a more technical discussion of scaled variables.

Chapter 2

Time independent scattering matrices and quantization

Much of atomic physics involves scattering processes. Traditionally, scattering involves the continuum states of particles that collide at a relative energy $E > 0$. However, the tools of scattering theory are also useful in treating bound state physics. This chapter describes how scattering theory, and scattering matrices in particular, can be extended to treat the bound ($E < 0$) and continuum ($E > 0$) states of an atomic electron in external electromagnetic fields.

The use of scattering methods to unify bound and continuum physics is not new. Quantum-defect theory was developed, beginning in the 1950s, by Seaton [85, 86, 87, 88] to describe the interaction of an electron with a positive ion. When the interaction of the electron with the positive ion is encapsulated in a scattering (or S) matrix, diverse phenomena such as photoabsorption, autoionization, electron-ion scattering and dielectronic recombination of atoms can be treated within the same framework. The S-matrices introduced in this chapter and used throughout the following chapters rely heavily on the concepts and methods of quantum-defect theory. Because of this, I begin by reviewing the relevant parts of quantum-defect theory. A more thorough introduction to quantum-defect theory can be found in a number of review articles [50, 68].

After the relevant tools of quantum-defect theory have been introduced, S-matrices for the treatment of atoms in external fields emerge with a few simple extensions. The emphasis in this chapter is on the basic definitions and properties of these S-matrices and the physical picture upon which they are built. The details of how the S-matrices can be calculated are delayed until later chapters. One of the central results of this thesis is the derivation of semiclassical approximations for the S-matrices (Ch. 5).

However, unless otherwise noted, all of the formulas and derivations in this chapter will be exact results. It is important to show how exact, quantum mechanical expressions for observables such as the bound state energies and the photoabsorption cross section of atoms in external fields can be derived in terms of the S-matrices. Even before semiclassical approximations are introduced, much physical insight about these nonintegrable systems can be gained by phrasing everything in terms of the S-matrices of this chapter.

Section 1 reviews the needed tools of quantum-defect theory. Section 2 extends the results of quantum-defect theory to include the effects of external fields applied to the atom. Section 3 concludes with a short discussion of the results of Sec. 2.

2.1 Quantum defect theory

Quantum-defect theory (QDT) relies on many of the same concepts as traditional time-independent scattering theory [89]. The most important of these is the asymptotic region. When two particles collide, most of the complicated physics occurs when the particles are very close to each other. Typically, outside this complicated "interaction" region, the physics between the particles simplifies greatly. For instance, when an electron collides with a positive ion, the complicated many body dynamics between the approaching electron and the particles comprising the ion can be neglected when the electron is farther than about 10-20 Bohr radii away. Beyond this distance the long-range electron-ion interaction is simply a spherically symmetric Coulomb potential. The word "asymptotic" reflects the usual case of particles colliding in the continuum where the physics simplifies as the interparticle separation r (also called the fragmentation coordinate) tends off to infinity.

However, it is not necessary for the fragmentation coordinate to approach infinity to use the tools of scattering theory. Rather, scattering theory is useful as long as the physics simplifies in some region of space. It is this perspective that undergirds the success of QDT. That is, QDT uses the fact that when an atomic electron is in a highly excited bound state, it spends most of its time far from the residual ion in a pure Coulomb potential. Thus, in QDT two regions of space are identified. First, at small distances ($r < 10$ a.u.) the electron interacts strongly with the constituents of the ionic core. In this **core**

region the complicated interactions between the electron and the ionic core, including electron-electron repulsion and the Pauli exclusion principle, are important. Second, at large distances ($r > 10$ a.u.) these complicated interactions are unimportant and the electron moves in a pure Coulomb potential. This constitutes the long-range or **matching region**. Here the full solutions of the Schrödinger equation in the core region are matched to a simple form involving Coulomb functions, channel functions and the core region S-matrix $\underline{S}^{\text{core}}$.

2.1.1 Energy normalized Coulomb functions

Before the S-matrix can be defined, the properties of the Coulomb functions must be outlined. As Seaton points out [50], "the whole of quantum-defect theory hinges on a knowledge of their mathematical properties." The relevant Schrödinger equation for these solutions,

$$\left(-\frac{1}{2}\frac{d^2}{dr^2} + \frac{l(l+1)}{2r^2} - \frac{1}{r}\right) u(r) = Eu(r), \tag{2.1}$$

is that of an electron in an attractive Coulomb potential, where the first derivative with respect to r has been eliminated by the substitution $\psi(r) = u(r)/r$. This second-order linear equation for the Coulomb function $u(r)$ has two linearly independent solutions, which can be chosen in a number of ways. The choice used in this paper (f^+_{El}, f^-_{El}) follows that of [68] and leads to an S-matrix formulation of QDT. For brevity, the explicit energy and l dependence of these functions will often be omitted. These and alternate pairs of linearly independent Coulomb functions have been studied in depth by Seaton [50] and by Greene *et al.* [90, 91].

More details of these Coulomb functions can be found in the above references, but a few of their more important properties are mentioned here. The pair (f^+, f^-) are energy normalized[1] and obey the traveling-wave boundary conditions ($f^{\pm\prime}(r) = \pm ik(r) f^{\pm}(r)$ in a WKB [24] approximation) typical of scattering theory. However, it should be realized that for negative energies, the traveling wave boundary conditions hold only in the classically allowed regions; these functions diverge exponentially at both

[1] Two solutions are energy normalized if $\left\langle f^+_{El} | f^+_{E'l} \right\rangle = \delta(E - E')$.

$r \to \infty$ and $r \to 0$ when $E < 0$. The Wronskians of these functions,

$$\mathrm{W}\left[f_l^-, f_l^+\right] = f_l^- f_l^{+\prime} - f_l^{-\prime} f_l^+ = \frac{2i}{\pi}, \tag{2.2}$$

$$\mathrm{W}\left[f_l^-, f_l^-\right] = \mathrm{W}\left[f_l^+, f_l^+\right] = 0, \tag{2.3}$$

will be used throughout this work. The widely used regular and irregular Coulomb functions[2] of QDT (f, g) are related to the pair (f^+, f^-) by the relation $f^\pm = (-g \pm if)/\sqrt{2}$. Because this thesis deals primarily with highly excited Rydberg states, their zero-energy form [92],

$$f_l^\pm(r) \longrightarrow \pm i\sqrt{r} H_{2l+1}^{(1,2)}(\sqrt{8r}) \qquad (E \to 0), \tag{2.4}$$

will be useful. Furthermore, when l is "small" and r is "large" the asymptotic forms of the Hankel functions in Eq. (2.4) can be used [93]:

$$H_{2l+1}^{(1,2)}(\sqrt{8r}) \longrightarrow \sqrt{\frac{2}{\pi\sqrt{8r}}} e^{\pm i(\sqrt{8r} - \frac{\pi}{2}(2l+1) - \frac{\pi}{4})} \qquad (\text{large } r). \tag{2.5}$$

The semiclassical approximations developed in later chapters will use these approximate forms of the Coulomb functions. Next the other degrees of freedom are addressed.

2.1.2 Channel functions

In quantum-defect theory, all of the information about the ionic core and the spin and angular degrees of freedom of the Rydberg electron is contained in channel functions. These degrees of freedom are typically quantized from the start by expanding the full wavefunction in a discrete set of these channel functions $\phi_i(\Omega)$. Then, in any region, the N linearly independent solutions (labeled by α) of the Schrödinger equation can be written in terms of these channel functions [68] and the multichannel radial wavefunction $F_{i\alpha}(r)$:

$$\psi_\alpha(r, \Omega) = \frac{1}{r} \sum_i \phi_i(\Omega) F_{i\alpha}(r). \tag{2.6}$$

The discrete index i labels the states (or channels) of the ionic core as well as the spin of the Rydberg electron. The continuous coordinate Ω denotes the angular degrees of freedom of the electron. As an

[2] This pair of Coulomb functions (f, g) leads to an alternative form of QDT that involves a real symmetric K-matrix rather than a complex unitary S-matrix.

example, in the alkali-metal atoms the channel functions are most often just the spherical harmonics $Y_{lm}(\theta, \phi)$. Typically, the channel functions form a complete and orthonormal set. When the expansion of the wavefunction (2.6) is used in the Schrödinger equation and the resulting equation is projected onto the channel functions, the radial wavefunction $\underline{F}(r)$ (now written as a matrix) is found to obey the multichannel radial Schrödinger equation:

$$\frac{1}{2}\underline{F}''(r) + (E - \underline{V})\,\underline{F}(r) = 0, \tag{2.7}$$

where the effective potential matrix is defined as:

$$V_{ij}(r) = \left\langle \Phi_i \left| \frac{\vec{L}^2}{2r^2} + V(r, \Omega) \right| \Phi_j \right\rangle. \tag{2.8}$$

At a total energy E there are two qualitatively different types of channels: open channels and closed channels. The ith channel is open when a Rydberg electron in that channel can escape to infinity ($E > E_i$ where E_i is the ionization threshold energy for the ith channel). The ith channel is closed when the electron in that channel is bound ($E < E_i$). In multichannel contexts, the energy in the ith channel will always be measured with respect to the ionization threshold energy E_i in that channel, so that quantities such as the Coulomb functions $f_i^{\pm}$ will be functions of $E - E_i$.

2.1.3 S-matrices in quantum-defect theory

As early practitioners [85, 94] of QDT realized, the most important feature of the energy normalized Coulomb functions is that they allow the results of scattering theory to be continued below threshold to negative energies. The work of QDT begins after the multichannel radial wavefunction $F_{i\alpha}^{\text{core}}(r)$ in the complicated core region has been determined numerically. In the matching region ($r > 10$ a.u.), this function is expressed as,

$$F_{i\alpha}^{\text{core}}(r) = \frac{1}{i\sqrt{2}}\left[f_i^+(r)P_{i\alpha} - f_i^-(r)Q_{i\alpha}\right], \tag{2.9}$$

where the matrices $\underline{P}$ and $\underline{Q}$ encapsulate any non-Coulombic physics of the core region. The multichannel S-matrix state (now written as a matrix) $\underline{M}^{\text{core}}(r)$ is simply a linear combination of these numerically

determined solutions,

$$\underline{M}^{\text{core}}(r) = \underline{F}^{\text{core}}(r)\underline{Q}^{-1} = \frac{1}{i\sqrt{2}}\left[\underline{f}^{+}(r)\underline{S}^{\text{core}} - \underline{f}^{-}(r)\right], \tag{2.10}$$

so that the S-matrix is just $\underline{S}^{\text{core}} = \underline{P}\underline{Q}^{-1}$. This specific linear combination of solutions, then, serves to define the core-region S-matrix. As long as the S-matrix state (2.10) is used in the Coulomb region no approximations are made. For the case of hydrogen ($\underline{S}^{\text{core}} = \underline{1}$) the S-matrix state (2.10) reduces to the regular Coulomb function $f_i(r)$. It is important to mention that at this point, only the physical boundary conditions at $r = 0$ have been imposed, while the boundary condition at $r = \infty$ remain unspecified. The key point of QDT is that because the boundary conditions at $r = \infty$ are not imposed, the S-matrix in Eq. (2.10) varies slowly with energy. In most cases it can be regarded as independent of energy over ranges of about 1 eV. All of the rapid energy dependence of physical observables comes from the properties of the energy normalized Coulomb functions. To illustrate how the boundary conditions at $r = \infty$ can be imposed, I now sketch the derivation of the well known modified Rydberg formula [95, 96],

$$E_{nl} = -\frac{1}{2(n-\mu_l)}, \tag{2.11}$$

for the bound levels of an alkali-metal atom. The μ_l are the quantum defects which vanish for the "non-defective" case of hydrogen. The core-region scattering matrix $\underline{S}^{\text{core}}$ for an alkali-metal atom is diagonal in a spherical representation and can be written in terms of these quantum defects:

$$S^{\text{core}}_{ll'} = \delta_{ll'} e^{2\pi i \mu_l}. \tag{2.12}$$

The boundary condition appropriate for bound states is imposed by equating a linear combination of the wavefunction of Eq. (2.10) to a linear combination of wavefunctions that decay exponentially as $r \to \infty$. The single-channel decaying solution is known as the Whittaker Coulomb function [68] $W_{El}(r)$ and is written in terms of the pair (f^+, f^-) and the Coulomb phase $\beta = \pi(\nu - l)$, where $\nu = 1/\sqrt{-2E}$ is the effective quantum number:

$$W_{El}(r) = \frac{1}{i\sqrt{2}}\left[f^{-}_{El}(r)e^{2i\beta} - f^{+}_{El}(r)\right]e^{-i\beta}. \tag{2.13}$$

The matching equation between Eq. (2.10) and Eq. (2.13),

$$\underline{M}^{\text{core}}(r)\,\overrightarrow{B}^{\,\text{core}} = \underline{W}(r)\,\overrightarrow{B}^{\,\text{LR}}, \tag{2.14}$$

involves undetermined coefficients B_l^{core} and B_l^{LR}. In solving for the vectors of coefficients $\overrightarrow{B}^{\,\text{core}}$ and $\overrightarrow{B}^{\,\text{LR}}$, it is found that the all of the boundary conditions (at both $r = 0$ and $r = \infty$) can be satisfied only when the condition,

$$\det(\underline{1} - \underline{S}^{\text{core}} e^{2i\underline{\beta}(E)}) = 0, \tag{2.15}$$

is true. When $\underline{S}^{\text{core}} = e^{2\pi i \underline{\mu}}$, as for an alkali-metal atom, the Rydberg formula of Eq. (2.11) emerges as the zeros of this equation. For the purposes of this thesis, I regard Eq. (2.15) as the fundamental equation giving the bound state spectrum of the Rydberg states of an atom. In the following section this equation is generalized to include the effects of a static external electromagnetic field applied to the atom. This analysis of the bound state physics applies when all of the channels are closed. For channels that become open as the energy is increased, outgoing-wave boundary conditions at $r = \infty$ must be applied. The formulas appropriate to this case can be found in the standard QDT literature, but are not provided in this review.

To use the methods of QDT to treat atoms in external electromagnetic fields, a difficulty must be faced. When a static field (magnetic, electric, or a combination of them) is applied to an atom, the long range spherical symmetry is broken. The long range potential of the electron then becomes,

$$V = -\frac{1}{r} + \frac{\rho^2 B^2}{8} + Fz, \tag{2.16}$$

where B is the magnetic field in atomic units ($B(\text{Tesla})/2.35 \times 10^5$) and F is the electric field in the same units ($F(V/m)/5.1423 \times 10^{11}$). It is clear that the external fields destroy the simple long-range Coulomb physics that allowed scattering theory to be used below threshold. The following section shows how this difficulty can be overcome.

2.2 S-matrices for atoms in external fields

As discussed above, the main physical requirement for using scattering theory to treat a problem is that the motion simplifies in some region of space. The key point is that such a region exists for an atomic electron in external electromagnetic fields. While external fields do destroy the long-range spherical symmetry of the Rydberg electron's motion, the electronic physics remains simple at intermediate distances ($10 < r < 100$ a.u.), even in the presence of strong external fields. In this intermediate range of radii, both the effects of the ionic core and of the external fields can be neglected, and again the Rydberg electron evolves in a pure Coulomb potential. For example, in a 6 Telsa magnetic field at a distance of $r = 100$ a.u., the ratio of the diamagnetic energy to the Coulomb energy is approximately 10^{-4}. This feature of an atomic electron in external fields was first recognized by Clark and Taylor [70] and has since been used in most theoretical treatments, both quantum and semiclassical, of these systems. This allows the methods of QDT and scattering theory to be extended to the case of a Hamiltonian that is nonintegrable.

With this in mind, this thesis is founded on the following physical picture. The quantum state of a highly excited atomic electron in the presence of external fields can be pictured as a time-independent scattering process. In this process, the electron scatters multiple times off of the ionic core and the long-range fields (Coulomb and external), each time returning to the simple Coulombic region. All of the information about these scattering events is contained in two scattering matrices: a core region scattering matrix $\underline{S}^{\rm core}$ and a nontrivial long-range scattering matrix $\underline{S}^{\rm LR}$. It is important to remember that each S-matrix element is a quantum mechanical amplitude to scatter off the core or long-range region **a single time**. The remainder of this chapter and the next shows how these two S-matrices control the most interesting physics of atoms in external electromagnetic fields.

At this point it is useful to summarize the properties of the three basic regions in which an atomic electron in external fields moves. Figure 2.1 provides a graphical representation of this partitioning of configuration space.

(1) Core region ($r < 10$ a.u.): Here, complicated interactions such as the electron-electron re-

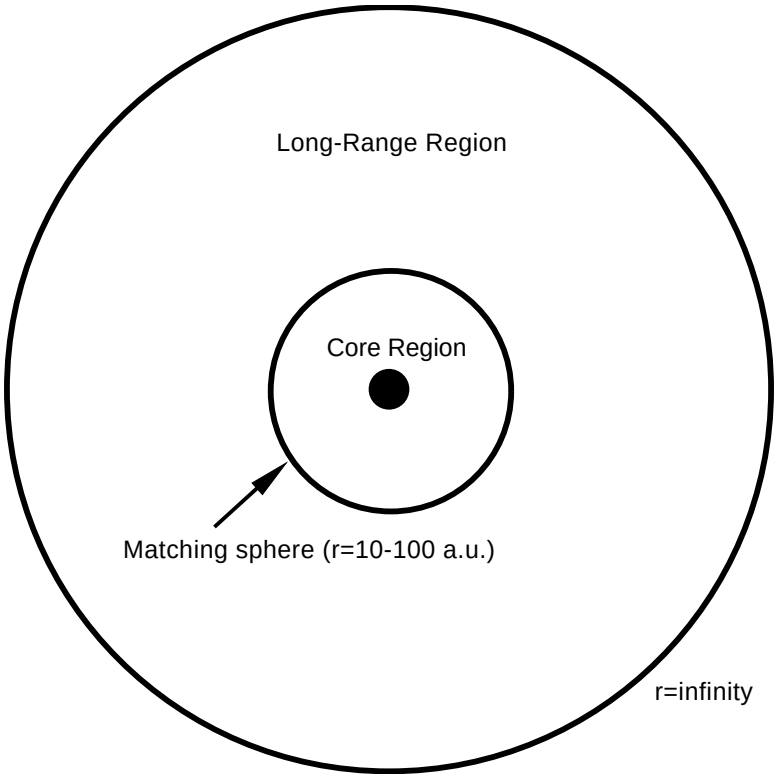

Figure 2.1: The various regions of configuration space in which a Rydberg electron in external electromagnetic fields travels are shown. The core region ($r < 10$ a.u.), matching region ($10 < r < 100$ a.u.), and the long-range region ($r > 100$) are shown as concentric spherical shells. Using the matching region as "home base" the electron scatters either inward off the ionic core (shown as a filled circle at the center), or outward off the long range Coulomb and external field potentials. Each of these scattering processes is encapsulated in a scattering matrix.

pulsion and the Pauli exclusion principle dominate the physics of the Rydberg electron. The external fields can be ignored in this region. As in standard QDT, the physics in this region is encapsulated in an energy independent scattering matrix $\underline{S}^{\text{core}}$.

(2) Matching region ($10 < r < 100$ a.u.): Here, the Rydberg electron sees only a spherically symmetric Coulomb potential. I call it the matching region because solutions from the core and long-range regions are matched in this region to "S-matrix states." Thus, this region functions much like an asymptotic region in traditional scattering theory.

(3) Long-range region ($100 < r < 10^4$ a.u.): Here, the spherically symmetric Coulomb potential and the external electromagnetic fields compete on an equal footing. Depending on what configuration of external fields are applied, the physics can be integrable (electric and Coulomb field only) or nonintegrable (Coulomb field plus magnetic field or magnetic and electric fields). In either case, the Hamiltonian is not separable in the same coordinate system as the core region, if at all. The physics in this region is encapsulated in a long-range scattering matrix $\underline{S}^{\text{LR}}$.

The exact boundaries between these regions are somewhat flexible and depend on factors such as the total energy, external field strengths and details of the ionic core. The important point is that the physics is qualitatively different in each region.

Although this thesis focuses on bound state physics, one further complication that emerges above threshold deserves mention here. Above the ionization threshold, a fourth region is identified beyond $r = 10^4$. Here, the Coulomb field has become far less important, and the external fields dominate the physics. Again, the details of the physics here are determined by the configuration of external fields that are applied. For the case of an external magnetic field, the electron moves out in decoupled Landau channels along the direction of the magnetic field. For an applied electric field, the electron approaches infinity as an outgoing wave in parabolic coordinates. For the cases of parallel or crossed electric and magnetic fields, the physics is more complicated at infinity, but nonetheless is still approximately integrable.

2.2.1 S-matrix states

Now, using this matching region ($10 < r < 100$ a.u.) like an asymptotic region in traditional scattering theory, scattering matrices for an atomic electron in external fields are introduced. As before, all but the radial degree of freedom will be expanded in a set of channel functions $\Phi_i(\Omega)$. Like both QDT and traditional scattering theory, the S-matrices are defined by writing down particular linear combinations of solutions of the Schrödinger equation, the "S-matrix states," in the matching region. However, now there are two S-matrix states. The first, $\underline{M}^{\text{core}}(r)$, is related to the numerically determined solution $\underline{F}^{\text{core}}(r)$ regular at $r = 0$ and determines the core-region S-matrix $\underline{S}^{\text{core}}$. The second, $\underline{M}^{\text{LR}}(r)$, is related to the numerically determined solution $\underline{F}^{\text{LR}}(r)$ having physical boundary conditions at $r = \infty$ and determines the long-range S-matrix $\underline{S}^{\text{LR}}$. In terms of the Coulomb functions and the S-matrices these solutions are:

$$\underline{M}^{\text{core}}(r) = \frac{1}{i\sqrt{2}}\left[\underline{f}^{+}(r)\underline{S}^{\text{core}} - \underline{f}^{-}(r)\right], \tag{2.17}$$

$$\underline{M}^{\text{LR}}(r) = \frac{1}{i\sqrt{2}}\left[\underline{f}^{-}(r)\underline{S}^{\text{LR}} - \underline{f}^{+}(r)\right]. \tag{2.18}$$

These forms of the solutions are only valid in the Coulomb matching region ($10 < r < 100$ a.u.). While it may seem that these S-matrix states are "just another set of linearly independent solutions of the Schrödinger equation," their usefulness will be demonstrated throughout this thesis as they are used to derive a number of important results.

A number of properties of these S-matrices are worth mentioning. By comparing the long-range S-matrix state $\underline{M}^{\text{LR}}(r)$ (2.18) with the Whittaker Coulomb function (2.13) it is seen that the long-range S-matrix with no external fields is simply the diagonal matrix $\underline{S}^{\text{LR}}(E) = e^{2i\underline{\beta}(E)}$. Thus, unlike the core region S-matrix, the long-range S-matrix depends strongly on the energy. When external fields are applied this strong energy dependence remains, but $\underline{S}^{\text{LR}}(E)$ becomes non-diagonal because of the broken spherical symmetry in the long-range region. As in standard scattering theory, both of these S-matrices are unitary and have finite dimension at a given energy E on the real axis. The dimension of the S-matrices is determined by the number of locally open channels in the matching region. For an alkali-metal atom, this number can be estimated by the maximum classically allowed angular momentum l at a

radius r_0 somewhere in the matching region

$$l_{\max} = \sqrt{2r_0^2\left(E + \frac{1}{r_0}\right)} - \frac{1}{2}. \tag{2.19}$$

As stated above, the two S-matrices $\underline{S}^{\text{core}}$ and $\underline{S}^{\text{LR}}$ determine the most interesting properties of atomic Rydberg states in external fields. The first such property that I investigate is the bound state energies of the Rydberg electron.

2.2.2 Quantization using S-matrices

The highly excited eigenstates of a nonintegrable Hamiltonian are characterized by global chaos in the classical domain and a lack of good quantum numbers in the quantum domain. Because much of our intuition about quantum eigenstates relies on the existence of good quantum numbers, physical insight about the eigenstates is more difficult to gain in a nonintegrable system. Some of the traditional methods of quantization (separation of variables, perturbation theory) fail completely for nonintegrable systems. Others, such as variational methods, struggle to give any insight about the highly excited states they provide. Because of this, it is desirable to have a method of quantization that is able to give physical insight as well as accurate eigenvalues.

Here I present an alternative to the traditional methods of quantization; one that involves the two scattering matrices $\underline{S}^{\text{core}}$ and $\underline{S}^{\text{LR}}(E)$. The result derived below,

$$\det\left[\underline{1} - \underline{S}^{\text{core}}\underline{S}^{\text{LR}}(E)\right] = 0, \tag{2.20}$$

was first suggested by Aymar *et al.* [68], but nothing was known at the time about the details of the long-range S-matrix when external fields are applied to the atom. These details turn out to be very significant as any physical insight contained in Eq. (2.20) must be provided by the S-matrices themselves. A detailed discussion of the physics contained in $\underline{S}^{\text{LR}}$ is delayed until Chs. 4 and 5 where I show how to calculate this S-matrix using accurate quantum calculations and semiclassical approximations. As expected, this condition (2.20) is identical to that of QDT (2.15) with the matrix $e^{2i\underline{\beta}}$ replaced by the long range scattering matrix $\underline{S}^{\text{LR}}$. Although the derivation of Eq. (2.20) is not difficult, I record the details here as some of the intermediate results will be useful later on.

To derive the quantization condition (2.20), I construct the linear combination of solutions that satisfies the physical boundary conditions at both $r = 0$ and $r = \infty$. Because the S-matrix states $\underline{M}^{\rm core}(r)$ and $\underline{M}^{\rm LR}(r)$ in Eqs. (2.17) and (2.18) satisfy the needed boundary conditions at $r = 0$ and $r = \infty$ respectively, the physical solution in the matching region must be a linear combination of either of these solutions. The physical linear combinations ($\overrightarrow{\psi}^{\rm core}$ and $\overrightarrow{\psi}^{\rm LR}$) are written in terms of the S-matrix states, Eqs. (2.17) and (2.18), and yet undetermined expansion coefficients $B_i^{\rm core}$ and $B_i^{\rm LR}$:

$$\overrightarrow{\psi}^{\rm core}(r) = \underline{M}^{\rm core}(r)\,\overrightarrow{B}^{\rm core} = \frac{1}{i\sqrt{2}}\left[\underline{f}^{+}(r)\underline{S}^{\rm core} - \underline{f}^{-}(r)\right]\overrightarrow{B}^{\rm core} \tag{2.21}$$

$$\overrightarrow{\psi}^{\rm LR}(r) = \underline{M}^{\rm LR}(r)\,\overrightarrow{B}^{\rm LR} = \frac{1}{i\sqrt{2}}\left[\underline{f}^{-}(r)\underline{S}^{\rm LR} - \underline{f}^{+}(r)\right]\overrightarrow{B}^{\rm LR}\,. \tag{2.22}$$

These two physical solutions must be identical. Thus, equating Eq. (2.21) to Eq. (2.22) somewhere in the matching region ($\overrightarrow{\psi}^{\rm core}(r_0) = \overrightarrow{\psi}^{\rm LR}(r_0)$) yields an equation for the coefficients $\overrightarrow{B}^{\rm LR}$,

$$\left[\underline{1} - \underline{S}^{\rm core}\underline{S}^{\rm LR}(E)\right]\overrightarrow{B}^{\rm LR} = 0, \tag{2.23}$$

along with a two equations relating $\overrightarrow{B}^{\rm core}$ and $\overrightarrow{B}^{\rm LR}$:

$$\overrightarrow{B}^{\rm LR} = -\underline{S}^{\rm core}\overrightarrow{B}^{\rm core} \tag{2.24}$$

$$\overrightarrow{B}^{\rm core} = -\underline{S}^{\rm LR}(E)\,\overrightarrow{B}^{\rm LR}. \tag{2.25}$$

A nontrivial solution of these equations (2.23 and either 2.24 or 2.25) exists at a given energy E only if the following condition is satisfied:

$$\det\left[\underline{1} - \underline{S}^{\rm core}\underline{S}^{\rm LR}(E)\right] = 0. \tag{2.26}$$

The zeros of this equation give the bound energy levels E_n of the atomic electron bound to a multichannel positive ion in the presence of external fields. In these formulas I have explicitly written out the energy dependence of the long-range S-matrix $\underline{S}^{\rm LR}(E)$ to emphasize that it varies rapidly as the energy is changed. The energy dependences of the other quantities, such as $\underline{S}^{\rm core}$, are much weaker and can often be neglected. Additionally, it should be kept in mind that $\underline{S}^{\rm LR}(E)$ is a strong function of the external field strengths B and F, whereas $\underline{S}^{\rm core}$ does not depend on these parameters for the comparatively weak fields ($B < 100$ Tesla) under consideration here. As long as exact quantum mechanical S-matrices are used,

the quantization condition (2.26) is exact. More importantly, when a semiclassical approximation for $\underline{S}^{\mathrm{LR}}$ is used, Eq. (2.26) becomes a semiclassical quantization condition for nonintegrable, multichannel atoms.

A number of researchers [77, 97, 98, 99, 100] have given quantization conditions similar to Eq. (2.26). This body of research shows that the quantization formula (2.26) represents a completely general method for quantizing multidimensional, nonintegrable systems. The only assumption I have made in its derivation is that at some radius (in the matching region), the effects of both the ionic core and the external fields on the electron can be neglected. Works by Prosen [99] and also Rouvinez and Smilansky [100] show that this assumption is not strictly necessary and I outline their approach here. To quantize a nonintegrable Hamiltonian of d spatial dimensions, configuration space is divided into two volumes V_a and V_b, which are separated by a $d-1$ dimensional surface. This surface, called the surface of section, is equivalent to a configuration space version of the classical surface of section introduced by Poincaré to reduce the dynamics of an autonomous Hamiltonian system ($2d$-dimensional phase space) to that of a discrete map of the surface onto itself. This surface of section is then used to define S-matrix states similar to Eqs. (2.17) and (2.18), along with S-matrices $\underline{S}^{\mathrm{a}}$ and $\underline{S}^{\mathrm{b}}$ for the two volumes. Their [99, 100] quantization condition,

$$\det\left[\underline{1} - \underline{S}^{\mathrm{a}}(E)\underline{S}^{\mathrm{b}}(E)\right] = 0, \tag{2.27}$$

is identical to the one I have derived here and shows the general nature of this approach.

However, the first formulation to use a Poincaré surface of section to quantize a nonintegrable Hamiltonian is Bogomolny's T-matrix method [97]. In this breakthrough work, Bogomolny derived a semiclassical quantization condition,

$$\det\left[\underline{1} - \underline{T}(E)\right] = 0, \tag{2.28}$$

for nonintegrable systems in terms of the "transfer matrix" $\underline{T}(E)$, which iterates a quantized version of the Poincaré map. In his work, the matrix $\underline{T}(E)$ is defined only semiclassically and is shown to be finite and unitary in the limit $\hbar \to 0$. Rouvinez and Smilansky [100] have shown that $\underline{T}(E)$ is equal to the product $\underline{S}^{\mathrm{a}}(E)\underline{S}^{\mathrm{b}}(E)$ in the same limit.

These works elucidate some insightful properties of quantization conditions written as a secular determinant involving finite, unitary S-matrices. A few of these properties are presented here for the case studied in this thesis, namely, an atomic electron in external fields. As Bogomolny demonstrates, because the S-matrices are finite and unitary, the secular determinant, Eq. (2.26), can be identified as a dynamical (or Selberg) zeta function [101, 102] $\zeta_s(E)$:

$$\zeta_s(E) = \det\left[\underline{1} - \underline{S}^{\text{core}}\underline{S}^{\text{LR}}(E)\right]. \tag{2.29}$$

It is called a zeta function because it shares many interesting properties with the well known Riemann zeta function [103] $\zeta(s)$ along the line $s = 1/2 + it$. An excellent discussion of these remarkable connections can be found in the text of Brack and Bhaduri [24]. Two such properties that $\zeta_s(E)$ shares with the Riemann zeta function are the existence of a functional equation,

$$\zeta_s(E) = e^{2\pi i\tilde{N}(E)}\zeta_s^*(E), \tag{2.30}$$

and the so called Riemann-Siegel relation,

$$\zeta_s(E) = G(E) + e^{2\pi i\tilde{N}(E)}G^*(E). \tag{2.31}$$

The quantity $\tilde{N}(E)$ is the mean number of states with energy less than E, which is simply

$$\tilde{N}(E) = \int \frac{d^d p\, d^d x}{(2\pi\hbar)^d}\Theta\left(E - H(\vec{p},\vec{x})\right) \tag{2.32}$$

for d degrees of freedom. In general, the $G(E)$ in Eq. (2.31) can be written as a finite sum over traces of powers of the matrix $\underline{S}^{\text{core}}\underline{S}^{\text{LR}}$, $\underline{S}^{\text{a}}\underline{S}^{\text{b}}$ or $\underline{T}$. By no means is this discussion of the dynamical zeta function complete; rather my goal has been to sketch the relationship between my work and that of others. The one new aspect of my work that has not been noted in the literature thus far is that functions such as $\det\left[\underline{1} - \underline{S}^{\text{core}}\underline{S}^{\text{LR}}(E)\right]$ have the properties, Eqs. (2.30) and (2.31), of a dynamical zeta function even when exact quantum mechanical S-matrices are used. Previously, the dynamical zeta function has only been used in the context of semiclassical approximations. Thus, I propose that when exact S-matrices are used, Eq. (2.29) represents a quantum-mechanical zeta function.

One final relationship [100] expresses the density of states,

$$g(E) = \sum_n \delta(E - E_n), \tag{2.33}$$

in terms of the zeta function, Eq. (2.29), and the mean density of states $\tilde{g}(E) = \frac{d\tilde{N}(E)}{dE}$:

$$g(E) = \tilde{g}(E) - \frac{1}{\pi}\mathrm{Im}\,\frac{d}{dE}\ln\det\left[\underline{1} - \underline{S}^{\mathrm{core}}\underline{S}^{\mathrm{LR}}(E)\right]. \tag{2.34}$$

This relationship shows that the matrix $\left[\underline{1} - \underline{S}^{\mathrm{core}}\underline{S}^{\mathrm{LR}}(E)\right]$ controls the oscillating part of the density of states. Now I show that this matrix also controls the normalization of the bound states.

2.2.3 Normalization

At a bound state energy E, the physical wavefunction $\overrightarrow{\psi}_E(r)$ takes the form of the S-matrix states, Eq. (2.21) or (2.22), in the matching region. A study of the normalization of these states gives further insight into the physics of the bound states of the Rydberg electron. The normalization condition derived here is similar to that of Aymar *et al.* [68], and uses the method given in Greene [90]. As with the quantization condition (2.26), an important feature of the normalization condition is that it depends only on the matrix $\left[\underline{1} - \underline{S}^{\mathrm{core}}\underline{S}^{\mathrm{LR}}\right]$. The beginning point of the derivation is the familiar normalization condition, written in terms of the multichannel radial wavefunction $\overrightarrow{\psi}_E(r)$ (either Eq. 2.21 or 2.22):

$$\int_0^\infty \mathrm{d}r\ \left|\overrightarrow{\psi}_E(r)\right|^2 = 1. \tag{2.35}$$

Integrals (or sums) over the angular and spin degrees of freedom are not present because the channel functions are assumed to be orthonormal. At first glance it appears that this integral requires the physical wavefunction at all radii. A well known trick of QDT uses Green's theorem to convert the volume integral to a surface integral in the matching region [90]. This is advantageous because the S-matrix forms, Eqs. (2.21) or (2.22), of $\overrightarrow{\psi}_E(r)$ can then be used. The transformation to a surface integral,

$$\begin{aligned}\int_a^b dr\ \overrightarrow{\psi}^{\dagger}_E(r)\,\overrightarrow{\psi}_E(r) &= \lim_{E'\to E}\int_a^b dr\ \overrightarrow{\psi}^{\dagger}_{E'}(r)\,\overrightarrow{\psi}_E(r) \\ &= \lim_{E'\to E}\frac{1}{2(E'-E)}\mathrm{W}\left[\overrightarrow{\psi}^{*}_{E'},\,\overrightarrow{\psi}_E\right]_a^b,\end{aligned} \tag{2.36}$$

involves the Wronskian,

$$\mathrm{W}\left[\overrightarrow{\psi}^{*}_{E'},\overrightarrow{\psi}_{E}\right]=\overrightarrow{\psi}^{\dagger}_{E'}\frac{d\overrightarrow{\psi_E}}{dr}-\frac{d\overrightarrow{\psi}^{\dagger}_{E'}}{dr}\overrightarrow{\psi}_{E}, \tag{2.37}$$

evaluated at the end points $[a,b]$ of the integration range. This formula is derived by first writing down the Schrödinger equations for $\overrightarrow{\psi}_{E}$ and $\overrightarrow{\psi}^{\dagger}_{E'}$:

$$\frac{1}{2}\overrightarrow{\psi}''_{E}+(E-\underline{V})\overrightarrow{\psi}_{E} = 0 \tag{2.38}$$

$$\frac{1}{2}\overrightarrow{\psi}^{\dagger\prime\prime}_{E'}+\overrightarrow{\psi}^{\dagger}_{E'}(E'-\underline{V}) = 0. \tag{2.39}$$

Left multiplying Eq. (2.38) by $\overrightarrow{\psi}^{\dagger}_{E'}$ and right multiplying Eq. (2.39) by $\overrightarrow{\psi}_{E}$, subtracting the two and using Green's theorem on the result gives Eq. (2.36). To use Eq. (2.36) to normalize the wave function (2.35) the range of integration is broken up into two integrals,

$$\int_0^\infty dr\,\left|\overrightarrow{\psi}_{E}(r)\right|^2=\int_0^{r_0}dr\,\left|\overrightarrow{\psi}^{\text{core}}_{E}(r)\right|^2+\int_{r_0}^\infty dr\,\left|\overrightarrow{\psi}^{\text{LR}}_{E}(r)\right|^2, \tag{2.40}$$

where the intermediate radius r_0 is chosen to be somewhere in the matching region. When Eq. (2.36) is used for each term on the right side of Eq. (2.40), the normalization condition for a bound state at energy E_n becomes:

$$1=\lim_{E'\to E}\frac{1}{2\left(E'-E_n\right)}\left(\mathrm{W}\left[\overrightarrow{\psi}^{\text{core}*}_{E'}(r_0),\overrightarrow{\psi}^{\text{core}}_{E_n}(r_0)\right]-\mathrm{W}\left[\overrightarrow{\psi}^{\text{LR}*}_{E'}(r_0),\overrightarrow{\psi}^{\text{LR}}_{E_n}(r_0)\right]\right). \tag{2.41}$$

To obtain this result one must use the fact the wavefunctions $\overrightarrow{\psi}^{\text{core}}_{E_n}$ and $\overrightarrow{\psi}^{\text{LR}}_{E_n}$ vanish at $r=0$ and $r=\infty$ respectively. Because r_0 is in the matching region, the S-matrix forms of $\overrightarrow{\psi}^{\text{core}}$ (2.21) and $\overrightarrow{\psi}^{\text{LR}}$ (2.22) can be used in Eq. (2.41) along with Eq. (2.24), $\overrightarrow{B}^{\text{LR}}=-\underline{S}^{\text{core}}\overrightarrow{B}^{\text{core}}$, to give:

$$1=\lim_{E'\to E_n}\frac{1}{2(E'-E_n)}\overrightarrow{B}^{\text{core}\dagger}\left(\underline{\mathrm{W}}_1-\underline{S}^{\text{core}\dagger}\underline{\mathrm{W}}_2\underline{S}^{\text{core}}\right)\overrightarrow{B}^{\text{core}}, \tag{2.42}$$

$$\underline{\mathrm{W}}_1 = -\frac{1}{2}\mathrm{W}\left[\underline{f}^{-}_{E'}\underline{S}^{\text{core}*}-\underline{f}^{+}_{E'},\underline{f}^{+}_{E_n}\underline{S}^{\text{core}}-\underline{f}^{-}_{E_n}\right], \tag{2.43}$$

$$\underline{\mathrm{W}}_2 = -\frac{1}{2}\mathrm{W}\left[\underline{f}^{+}_{E'}\underline{S}^{\text{LR}*}(E')-\underline{f}^{-}_{E'},\underline{f}^{-}_{E_n}\underline{S}^{\text{LR}}(E_n)-\underline{f}^{+}_{E_n}\right]. \tag{2.44}$$

The matrices $\underline{\mathrm{W}}_1$ and $\underline{\mathrm{W}}_2$ can then be simplified using the definition of the Wronskian (2.37) and the Wronskians of $\underline{f}^{\pm}$ given in Eqs. (2.2) and (2.3). Finally, the limit $E'\to E_n$ is taken using l'Hospital's

rule. After some algebra, and using Eq. (2.23), the final form of the normalization condition reads:

$$1 = \frac{1}{2\pi} \vec{B}^{\mathrm{LR}\dagger} \frac{d}{dE} i \left(\underline{1} - \underline{S}^{\mathrm{core}} \underline{S}^{\mathrm{LR}} \right) \vec{B}^{\mathrm{LR}}. \tag{2.45}$$

As in the quantization condition, the matrix $\left(\underline{1} - \underline{S}^{\mathrm{core}} \underline{S}^{\mathrm{LR}} \right)$ controls the normalization of the bound states. As Harmin's work [83] on the Stark effect demonstrates, normalization constants such as this matrix are closely related to the density of states of the physical system. This is consistent with Eq. (2.34) that relates the quantum density of states to this matrix. In addition, in the next chapter the matrix $\left(\underline{1} - \underline{S}^{\mathrm{core}} \underline{S}^{\mathrm{LR}} \right)^{-1}$ appears as a "density of states matrix" in the atomic photoabsorption cross section.

Alternatively, as Aymar *et al.* [68] point out, the normalization condition (2.45) can be expressed in terms of the Hermitian time delay matrices [104] for the core and long-range regions:

$$\underline{Q}^{\mathrm{core(LR)}} = i \underline{S}^{\mathrm{core(LR)}} \frac{d \underline{S}^{\mathrm{core(LR)}\dagger}}{dE}. \tag{2.46}$$

The result,

$$1 = \frac{1}{2\pi} \vec{B}^{\mathrm{LR}\dagger} \left(\underline{Q}^{\mathrm{core}\dagger} - \underline{Q}^{\mathrm{LR}} \right) \vec{B}^{\mathrm{LR}},$$

shows that the normalization of the bound states involves a sort of balance between the physical time scales (encapsulated in $\underline{Q}^{\mathrm{LR}}$ and $\underline{Q}^{\mathrm{core}}$) in the core and long-range regions.

2.3 Discussion

In the previous section, ideas from scattering theory and QDT were used to study Rydberg states of atoms in static external electromagnetic fields. The following picture of the electron's motion undergirds this approach: the state of the Rydberg electron is pictured as a time-independent scattering process where the electron scatters repeatedly off the core and long-range regions each time returning to a radius in the "matching region" where it sees a pure Coulomb potential. The S-matrix states, Eqs. (2.17) and (2.18), formalize this idea by introducing two unitary S-matrices $\underline{S}^{\mathrm{core}}$ and $\underline{S}^{\mathrm{LR}}$. Using these S-matrix states I have derived a quantization condition (2.20) and a normalization condition (2.45) for the bound states of the Rydberg electron. These two equations, which are the main results of this chapter, begin to show that the most important physics of the electron is contained in the matrix $\left(\underline{1} - \underline{S}^{\mathrm{core}} \underline{S}^{\mathrm{LR}} \right)$.

This approach of dividing configuration space into two regions and defining an S-matrix for each region is advantageous for a number of reasons. First, S-matrices are ideally suited to semiclassical approximations. In Ch. 5 I derive such an approximation for the long-range S-matrix using a semiclassical Green's function. Semiclassically, $\underline{S}^{\mathrm{LR}}$ is written as a sum over classical orbits, closed-orbits, that are launched outward from a sphere in the matching region, scatter off the long-range fields and then return to the sphere after time T. I show that the classical action S_k (not to be confused with the matrix $\underline{S}^{\mathrm{LR}}$) of each such orbit contributes to the phase of the S-matrix in the form (see Eq. (5.39)):

$$\underline{S}^{\mathrm{LR}}(E) = \sum_k \underline{A}_k e^{iS_k(E)}. \tag{2.47}$$

The matrix $\underline{A}_i$ of each orbit depends on the stability, Maslov index, and initial and final angles of the orbit. While the results of this chapter can be written in terms of either K-matrices or R-matrices, the semiclassical approximations for these matrices are needlessly cumbersome compared to that of the S-matrix (2.47).

Second, S-matrices give important physical insight not available in other approaches. This can be seen by looking at the trace of the time delay matrix for the long-range region in a semiclassical approximation. A substitution of the semiclassical form of $\underline{S}^{\mathrm{LR}}$, Eq. (2.47), into the definition of the time delay matrix, Eq. (2.46), gives,

$$\mathrm{Tr}\left(\underline{Q}^{\mathrm{LR}}(E)\right) = \mathrm{Tr}\left(i\underline{S}^{\mathrm{LR}}\frac{d\underline{S}^{\mathrm{LR}\dagger}}{dE}\right) = \sum_k T_k(E)\alpha_k, \tag{2.48}$$

where $T_k(E) = \frac{dS_k}{dE}$ denotes the period of the kth classical orbit and $\alpha_k = \mathrm{Tr}(\underline{A}_k\underline{A}_k^\dagger)$ is a number indicating the relative importance of the orbit. This shows that the S-matrix $\underline{S}^{\mathrm{LR}}$ gives direct access to the time domain physics of the Rydberg electron. Chs. 4 and 5 show that the quantitative details of this time domain physics in $\underline{S}^{\mathrm{LR}}$ can be extracted by Fourier transforming $\underline{S}^{\mathrm{LR}}(E)$ into the time domain.

Third, and finally, dividing configuration space into two regions leads to an efficient approach. Once the long-range S-matrix has been calculated for a given configuration of external fields, the observables of many different atoms in that configuration of fields can be calculated by simply using the $\underline{S}^{\mathrm{core}}$ appropriate to each atom.

Of course, the best argument for formulating the theory in terms of S-matrices is their usefulness. This chapter has begun to build a case for this viewpoint by showing that the S-matrices $\underline{S}^{\mathrm{LR}}$ and $\underline{S}^{\mathrm{core}}$ determine the bound state physics of an atomic electron in the presence of an external electric or magnetic field. In the next chapter, I continue along these lines, exploring the relationship between the S-matrices and the atomic photoabsorption cross section.

Chapter 3

Coarse grained photoabsorption spectra

The physical observable focused on in this thesis is the photoabsorption cross section of atoms in external electromagnetic fields. This observable has provided both theorists and experimentalists a rich way of probing a classically chaotic Hamiltonian. The goal of this chapter is to forge a link between the important energy observable and this scattering matrices $\underline{S}'^{\mathrm{LR}}$ and $\underline{S}^{\mathrm{core}}$ of the previous chapter.

The near-threshold photoabsorption cross section of atoms in external fields presents a difficulty for the traditional approach of spectroscopy. Typically, the low lying spectra of atoms are interpreted by assigning a set of quantum numbers to each absorption line. While at times these quantum numbers are only approximate, this program gives a complete description of the atomic states when the density of states is sufficiently low. However, near the ionization threshold of atoms in external fields, this approach fails as the density of state becomes enormous. Even for hydrogen, the simple Rydberg series present with no external fields becomes an unrecognizable tangle of closed spaced absorption lines when an external magnetic field is applied. Even when approximate quantum numbers can be found, such as in the Stark effect, the prospect of labeling thousands of quantum states is daunting.

An alternative to interpreting each bound state individually is to directly focus on the energy-smoothed cross section. In the earliest diamagnetic Rydberg state experiments [30], this approach was necessary because the experimental resolution was insufficient to resolve individual lines near threshold. However, as theoretical methods such as closed-orbit theory [37, 38, 36] progressed, it was realized that this approach of studying the large-scale energy structures in the cross section was actually the preferred way to study these systems; even when experimental resolution allowed the identification of

individual lines. In the spirit of Gutzwiller's semiclassical theory for the energy-smoothed density of states [19, 18, 20, 21], Delos and coworkers showed that the global oscillations of the cross section with energy could be related to certain classical orbits in the system. These classical orbits, closed-orbits, begin at the nucleus, scatter off the long-range fields and return to the nucleus a time T_k later. As discussed in the introduction, the main result of closed-orbit theory [38] is a formula for the near-threshold, energy-smoothed cross section that involves an oscillating term $A_k \cos(ET_k)$ for each such orbit. This gives a simple interpretation of the global oscillations in the energy domain cross section.

The approach in this chapter follows that of closed-orbit theory. The goal will not be to predict the infinite resolution photoabsorption cross section; rather the focus is on obtaining the energy-smoothed, or "preconvolved" cross section directly. This work is meant to extend and generalize closed-orbit theory to a more general class of systems. Whereas closed-orbit theory and its extensions have been limited to single channel atoms with a single ionization threshold, the approach given here lays the foundation for the treatment of multichannel atoms with multiple escape thresholds in any configuration of external fields.

As with the previous chapter, the focus here is on the exact quantum mechanics of an atomic electron in external electromagnetic fields. The subtleties of introducing semiclassical approximations into the cross section are addressed in Ch. 6. It is important to see how the physical insights of semiclassical methods are, to a great extent, already present in the exact quantum-mechanical cross section. Section 3.1, using Robicheaux's preconvolved quantum-defect theory [105] for guidance, develops an exact expression for the preconvolved photoabsorption cross section of an atom in external electromagnetic fields. In Sec. 3.2, this cross section is interpreted and its general properties are discussed.

3.1 Preconvolved quantum-defect theory

To obtain an energy-smoothed photoabsorption cross section, one can proceed in two different ways. The first is to calculate the infinite resolution cross section $\sigma(E)$ on a fine energy mesh and then perform a numerical convolution with some smoothing function of width Γ to obtain the smoothed cross section $\sigma^{\Gamma}(E)$. An alternative approach is to convolve the cross section analytically, before any

quantities are calculated. This method of "preconvolution" avoids the costly calculation of the infinite resolution cross section altogether and gives $\sigma^{\Gamma}(E)$ directly in terms of simple parameters of QDT.

The first such example of a preconvolved photoabsorption cross section was derived by Robicheaux [105]. His result for the convolved cross section $\sigma^{\Gamma}(E)$ shows that preconvolution is handled elegantly in the context of multichannel QDT. Robicheaux begins by writing the convolved cross section in terms of a generalized Green's function. After that, the tools of QDT are used to find the relevant Green's function in terms of familiar elements of QDT. The final formula,

$$\sigma^{\Gamma}(E) = 4\pi^2\alpha\omega\,\mathrm{Re}\,\vec{d}\left[\underline{1} - \underline{S}^{\mathrm{core}}e^{2i\underline{\beta}}\right]^{-1}\left[\underline{1} + \underline{S}^{\mathrm{core}}e^{2i\underline{\beta}}\right]\vec{d}^{\dagger}, \tag{3.1}$$

depends only on the core-region S-matrix $\underline{S}^{\mathrm{core}}$, the long-range Coulomb phase $e^{2i\beta_j(E)}$ in each channel, and a vector of dipole matrix elements $\vec{d}$ between the initial atomic state and energy-normalized final states. By analyzing the properties of the Coulomb functions in the complex plane, Robicheaux showed that convolving the exact cross section with a Lorentzian of width Γ was equivalent to evaluating the QDT parameter $\beta_j(E)$ at a complex energy $E + i\Gamma/2$. More specifically, in Eq. (3.1), $\beta_j(E)$ takes the values,

$$\begin{aligned} \beta_j(E) &= \frac{\pi}{\sqrt{-2(E + i\Gamma/2 - E_j)}} \quad E < E_j, \\ &= i\infty \quad E > E_j, \end{aligned} \tag{3.2}$$

above and below the threshold energy E_j. Because the dipole vector $\vec{d}$ and the S-matrix $\underline{S}^{\mathrm{core}}$ can be calculated on a coarse mesh of real energies, Eq. (3.1) yields an extremely efficient method for the calculation $\sigma^{\Gamma}(E)$.

Although efficient and elegant, the result of Eq. (3.1) is only valid when the long-range field of the electron is a pure Coulomb potential. The methods used to derive it rely critically on the properties of Coulomb functions at large distances. Because external electromagnetic fields destroy the long-range spherical symmetry, a new approach for the preconvolved cross section must be found for this case. On the other hand, the quantization formula, Eq. (2.26), of the previous chapter suggests that a simple replacement of the matrix $e^{2i\underline{\beta}}$ by the long-range S-matrix $\underline{S}^{\mathrm{LR}}$ in Eq. (3.1) could give the desired gener-

alization. In the next section, I derive an expression for the preconvolved photoabsorption cross section for an atom in external fields and show that this naive guess is indeed correct.

3.1.1 Energy smoothing of the cross section

The first step in deriving a convolved cross section is to relate the convolved cross section to a Green's function evaluated at complex energies. Following Robicheaux [105], the convolved cross section $\sigma^{\Gamma}(E)$ is defined as the integral of the exact cross section $\sigma(E)$ with a Lorentzian of full width at half maximum (FWHM) Γ :

$$\sigma^{\Gamma}(E) = \frac{\Gamma}{2\pi} \int dE' \frac{\sigma(E')}{(E-E')^2 + \Gamma^2/4}. \tag{3.3}$$

While other convolution functions can be used, the Lorentzian leads to an elementary result,

$$\sigma^{\Gamma}(E) = \sigma(E + i\Gamma/2), \tag{3.4}$$

which is obtained by performing the integration in Eq. (3.3) by the method of contour integration. Because the exact cross section has only simple poles on the real energy axis, only the residue of the integrand at the pole of the Lorentzian, $E' = E + i\Gamma/2$, is needed when the contour is closed in the upper half of the complex plane. The standard expression for the atomic photoabsorption cross section in a perturbative laser field [1],

$$\sigma(E) = 4\pi^2 \alpha (E - E_0) \sum_i \left| \left\langle \psi_0 \left| \hat{D} \right| \psi^-_{E,i} \right\rangle \right|^2, \tag{3.5}$$

serves as the starting point in finding $\sigma(E + i\Gamma/2)$. The atom is taken to be in the initial quantum state $|\psi_0\rangle$ with energy E_0 before it makes a transition to the energy-normalized final states $\left|\psi^-_{E,i}\right\rangle$ having outgoing-waves in the ith channel only. The dipole operator $\hat{D}$ is given in terms of the photon polarization vector $\hat{\epsilon}$ and the position operator $\vec{r}$:

$$\hat{D} = \hat{\epsilon} \cdot \vec{r}. \tag{3.6}$$

As usual, the rule of averaging over indistinguishable initial states and summing over indistinguishable final states is implied in Eq. (3.5). In addition, $\omega = E - E_0$ is the frequency of the laser used to excite the transition.

Next, the photoabsorption cross section is written in terms of the outgoing-wave Green's function. Once this step is accomplished, the methods of QDT can be used to calculate the final result. As an operator [106], the outgoing-wave Green's function is defined as:

$$\hat{G}^{+}(E) = \lim_{\epsilon \to 0^{+}} (E + i\epsilon - \hat{H})^{-1}. \tag{3.7}$$

The relationship between this operator (3.7) and the cross section (3.5),

$$\sigma^{\Gamma}(E) = -4\pi\alpha\omega \,\mathrm{Im}\left\langle \hat{D}\psi_0 \left| \hat{G}^{+}(E + i\Gamma/2) \right| \hat{D}\psi_0 \right\rangle, \tag{3.8}$$

is well known and is derived in a number of articles [38, 106]. An important feature of this form of the cross section is that it is valid both above and below the ionization threshold. With this equation (3.8), the calculation of the convolved photoabsorption cross section has been reduced to the calculation of the Green's function $\hat{G}^{+}(E)$ at complex energies. In the next subsection (3.1.2) I give the details of how this Green's function can be computed when an external field is applied to the atom. The casual reader is encouraged to skip ahead to the final result, which is presented in subsection 3.1.3.

3.1.2 Finding the Green's function

The goal then, is to derive an expression for the outgoing-wave Green's function $G^{+}(\vec{x}, \vec{x}'; E)$ (3.7) at complex energies. The derivation presented here is the first to include the nontrivial effects of external fields in the long-range region. While it lacks rigor at certain points, the main ideas are present and provide a framework for future work. A discussion of the remaining open questions follows the derivation.

As stated in the previous chapter, the result is expected to involve the all important matrix $\left[\underline{1} - \underline{S}^{\mathrm{core}}\underline{S}^{\mathrm{LR}}\right]$. This is achieved by using the S-matrix states, Eqs. (2.17) and (2.18), to construct the required Green's function. This follows the standard method in the theory of Green's functions [107] of using solutions of the homogeneous equation to build the Green's function, which satisfies the inhomo-

geneous equation[1] ,

$$\left(\frac{1}{2}\nabla_x^2 + E - V(\vec{x})\right) G(\vec{x},\vec{x}';E) = \delta(\vec{x}-\vec{x}'). \tag{3.9}$$

In this approach, the boundary conditions on $G(\vec{x},\vec{x}';E)$ are imposed by constructing it out of solutions $\psi_\alpha(\vec{x})$ of the homogeneous equation (Eq. (3.9) with $\delta(\vec{x}-\vec{x}') \rightarrow 0$) that satisfy the same desired boundary conditions. Again, the desired Green's function derived here is regular at $r = 0$ and has outgoing-wave boundary conditions at $r = \infty$. I mention this because in future chapters this same approach will be use to find Green's functions obeying different boundary conditions. It is important to remember, that while all of the these Green's functions satisfy the same equation, Eq. (3.9), they are not identical. The details of the derivation are more straightforward when channel expansions of the wavefunction,

$$\psi_\alpha(r,\Omega) = \frac{1}{r}\sum_i \Phi_i(\Omega) M_{i\alpha}(r), \tag{3.10}$$

and the Green's function,

$$G(\vec{x},\vec{x}';E) = \frac{1}{rr'}\sum_{i,j} \Phi_i(\Omega)\tilde{G}_{ij}(\vec{x},\vec{x}';E)\Phi_j^*(\Omega'), \tag{3.11}$$

$$\tilde{G}_{ij}(r,r';E) = rr' \left\langle \Phi_i \left| G(\vec{x},\vec{x}';E) \right| \Phi_j \right\rangle, \tag{3.12}$$

are used. The multichannel Green's function, Eq. (3.12) (now written as a matrix $\underline{\tilde{G}}$), is a solution of the equation,

$$\frac{1}{2}\underline{\tilde{G}}''(r,r';E) + (E - \underline{V}(r)) = \underline{1}\delta(r-r'), \tag{3.13}$$

with the multichannel wavefunction $\underline{M}(r)$ obeying a similar, but homogeneous equation (2.7). The matrix $\underline{V}(r)$ is the multichannel effective potential of Eq. (2.8).

The solutions of the homogeneous equation satisfying the desired boundary conditions are the S-matrix states, Eqs. (2.17) and (2.18), of the previous chapter. The core-region state, $\underline{M}^{\text{core}}(r)$, is regular

[1] Some authors define the Green's function with an additional minus sign in front of the delta function in Eq. (3.9). I use this convention as it is consistent with what is typically used in semiclassical approximations [24].

at the origin and takes the form,

$$\underline{M}^{\text{core}}(r) = \frac{1}{i\sqrt{2}}\left[\underline{f}^{+}(r)\underline{S}^{\text{core}} - \underline{f}^{-}(r)\right], \tag{3.14}$$

in the matching region. The long-range state, $\underline{M}^{\text{LR}}(r)$, is an outgoing wave at infinity (although not necessarily in spherical channels) and takes the form,

$$\underline{M}^{\text{LR}}(r) = \frac{1}{i\sqrt{2}}\left[\underline{f}^{-}(r)\underline{S}^{\text{LR}} - \underline{f}^{+}(r)\right], \tag{3.15}$$

in the matching region. Outside the matching region, the numerical forms of these solutions must be used; this is implied when they are written as $\underline{M}^{\text{core}}(r)$ and $\underline{M}^{\text{LR}}(r)$. Now an ansatz for the Green's function,

$$\begin{aligned} \underline{\tilde{G}}(r,r') &= \underline{M}^{\text{LR}}(r)\underline{A}(r') \qquad r > r', \\ &= \underline{M}^{\text{core}}(r)\underline{B}(r') \qquad r < r', \end{aligned} \tag{3.16}$$

is given in terms of undetermined coefficients $\underline{A}(r')$ and $\underline{B}(r')$. These coefficients are determined by requiring that the Green's function is continuous at $r = r'$ and has a discontinuity in the first derivative given by,

$$\lim_{\epsilon\to 0^{+}} \frac{d}{dr}\underline{\tilde{G}}(r,r')\Big|_{r=r'-\epsilon}^{r=r'+\epsilon} = 2. \tag{3.17}$$

These requirements upon the ansatz (3.16) are enforced in the matching region where the S-matrix states, Eq. (3.14) and (3.15), can be used. This leads to a set of linear equations,

$$\left(\underline{f}^{-}\underline{S}^{\text{LR}} - \underline{f}^{+}\right)\underline{A} - \left(\underline{f}^{+}\underline{S}^{\text{core}} - \underline{f}^{-}\right)\underline{B} = 0, \tag{3.18}$$

$$\left(\underline{f}^{-\prime}\underline{S}^{\text{LR}} - \underline{f}^{+\prime}\right)\underline{A} - \left(\underline{f}^{+\prime}\underline{S}^{\text{core}} - \underline{f}^{-\prime}\right)\underline{B} = 2i\sqrt{2}, \tag{3.19}$$

for the coefficient matrices $\underline{A}(r')$ and $\underline{B}(r')$. A long but straightforward algebra gives the solutions:

$$\underline{A}(r') = 2\pi i\left[\underline{1} - \underline{S}^{\text{core}}\underline{S}^{\text{LR}}\right]^{-1}\underline{S}^{\text{core}}\underline{M}^{\text{core}\dagger}(r'), \tag{3.20}$$

$$\underline{B}(r') = 2\pi i\underline{S}^{\text{LR}}\left[\underline{1} - \underline{S}^{\text{core}}\underline{S}^{\text{LR}}\right]^{-1}\underline{M}^{\text{LR}\dagger}(r'). \tag{3.21}$$

These coefficients, Eqs. (3.20) and (3.21), along with the ansatz for the Green's function, Eq. (3.16),

determine the Green's function:

$$\begin{aligned}\underline{\tilde{G}}(r,r';E) &= 2\pi i\underline{M}^{\mathrm{LR}}(r)\left[\underline{1}-\underline{S}^{\mathrm{core}}\underline{S}^{\mathrm{LR}}\right]^{-1}\underline{S}^{\mathrm{core}}\underline{M}^{\mathrm{core}\dagger}(r') \quad r>r,' \\ &= 2\pi i\underline{M}^{\mathrm{core}}(r)\underline{S}^{\mathrm{LR}}\left[\underline{1}-\underline{S}^{\mathrm{core}}\underline{S}^{\mathrm{LR}}\right]^{-1}\underline{M}^{\mathrm{LR}\dagger}(r') \quad r>r'.\end{aligned} \tag{3.22}$$

It is desirable to simplify this form of the Green's function. Until now, all of the steps that have been taken have been well justified; the result is thus far exact. To use this Green's function to calculate the cross section, it is useful to write the long-range solution $\underline{M}^{\mathrm{core}}(r)$ in Eq. (3.22) in terms of the core-region solution $\underline{M}^{\mathrm{LR}}(r)$. At a bound state energy, two such relationships can be derived using Eqs. (2.21), (2.22), (2.24), and (2.25) of the previous chapter (Ch. 2):

$$\underline{M}^{\mathrm{LR}}(r) = -\underline{M}^{\mathrm{core}}(r)\underline{S}^{\mathrm{core}\dagger}, \tag{3.23}$$

$$\underline{M}^{\mathrm{LR}}(r) = -\underline{M}^{\mathrm{core}}(r)\underline{S}^{\mathrm{LR}}. \tag{3.24}$$

I now assume that these relationships, Eqs. (3.23) and (3.24), hold between the bound state energies as well. This is a reasonable assumption if the S-matrix solutions (3.14) and (3.15) vary slowly with energy. Using these relationships, Eqs. (3.23) and (3.24), in the expression for the Green's function, Eq. (3.22), gives the simple result,

$$\underline{\tilde{G}}(r,r';E) = -2\pi i\underline{M}^{\mathrm{core}}(r)\underline{S}^{\mathrm{core}\dagger}\left[\underline{1}-\underline{S}^{\mathrm{core}}\underline{S}^{\mathrm{LR}}\right]^{-1}\underline{S}^{\mathrm{core}}\underline{M}^{\mathrm{core}\dagger}(r'). \tag{3.25}$$

Because $\underline{M}^{\mathrm{core}}(r)$ appears symmetrically for both r and r' in this expression, the restrictions $r>r'$or $r<r'$ can be dropped. A subtle point about this Green's function (3.25) is that it is only part of the outgoing-wave Green's function. As Robicheaux documents, an additional "smooth" Green's function must be added to Eq. (3.25) to form the outgoing-wave Green's function. The smooth Green's function can be obtained by a physical argument (see [105]) about the above threshold cross section and reads:

$$\underline{\tilde{G}}^{s}(r,r';E) = i\pi\underline{M}^{\mathrm{core}}(r)\underline{M}^{\mathrm{core}\dagger}(r'). \tag{3.26}$$

Adding $\underline{\tilde{G}}^{s}(r,r';E)$ (3.26) to Eq. (3.25), the final form of the outgoing-wave Green's function is obtained:

$$\underline{\tilde{G}}^{+}(r,r';E) = -i\pi\underline{M}^{\mathrm{core}}(r)\underline{S}^{\mathrm{core}\dagger}\left[\underline{1}-\underline{S}^{\mathrm{core}}\underline{S}^{\mathrm{LR}}\right]^{-1}\left[\underline{1}+\underline{S}^{\mathrm{core}}\underline{S}^{\mathrm{LR}}\right]\underline{S}^{\mathrm{core}}\underline{M}^{\mathrm{core}\dagger}(r'). \tag{3.27}$$

As expected, this Green's function depends on the ubiquitous matrix $\left[\underline{1} - \underline{S}^{\rm core}\underline{S}^{\rm LR}\right]$ and the core-region S-matrix states $\underline{M}^{\rm core}(r)$ that will be used to define dipole vectors.

There are two unresolved questions in this derivation. First, I have used the relationships, Eqs. (3.23) and (3.24), away from bound state energies where they are known to be valid. Although I expect this to be an excellent approximation, this needs to be justified in a more rigorous manner. Second, the full nature of the smooth Green's function $\underline{\tilde{G}}^{s}(r, r'; E)$ and its relationship to the outgoing-wave Green's function needs to be explored further. In spite of these remaining questions, there is little doubt that the Green's function, Eq. (3.27), derived here is the outgoing wave Green's function needed for the cross section. This is because the matrix $\left[\underline{1} - \underline{S}^{\rm core}\underline{S}^{\rm LR}\right]$, which vanishes at the bound state energies E_n, ensures that the Green's function of Eq. (3.27) has the same pole structure in the complex energy plane as the outgoing wave Green's function, Eq. (3.7). Using the ideas of Labastie *et al.* [106] it is also possible to show that the normalization condition, Eq. (2.45), ensures that the residues of these poles coincide with those of Eq. (3.7). Thus, based on the analytic properties of Eq. (3.27) in the complex energy plane, the Green's function I have constructed here can differ from the true outgoing-wave Green's function by at most an analytic function of the energy (the smooth Green's function).

3.1.3 Putting it all together

With an expression for the outgoing-wave Green's function, Eq. (3.27), the final form of the convolved cross section can be given. A substitution of the Green's function (3.27) into the expression for the cross section (3.8) gives the generalization of Robicheaux's formula,

$$\sigma^{\Gamma}(E) = 4\pi^2\alpha\omega\,{\rm Re}\,\vec{d}\left[\underline{1} - \underline{S}^{\rm core}\underline{S}^{\rm LR}(E+i\Gamma/2)\right]^{-1}\left[\underline{1} + \underline{S}^{\rm core}\underline{S}^{\rm LR}(E+i\Gamma/2)\right]\vec{d}^{\dagger}, \tag{3.28}$$

which includes the effects of external electric and magnetic fields. As promised, this result is the preconvolved cross section of Eq. (3.1) with the replacement $e^{2i\underline{\beta}} \rightarrow \underline{S}^{\rm LR}$. In addition, the matrix $\left[\underline{1} - \underline{S}^{\rm core}\underline{S}^{\rm LR}\right]^{-1}\left[\underline{1} + \underline{S}^{\rm core}\underline{S}^{\rm LR}\right]$ appears as a generalized density of states matrix in the language of Harmin [83] and others [106], which determines all of the nontrivial aspects of the cross section.

At a more primitive level, the cross section, Eq. (3.28), depends on three basic quantities: the

dipole vector $\vec{d}$ and the S-matrices for the long-range and core regions $\underline{S}^{\mathrm{LR}}$ and $\underline{S}^{\mathrm{core}}$. The dipole vector consists of matrix elements of the dipole operator $\hat{D}$,

$$d_k = \left\langle \psi_0 \left| \hat{D} \right| \psi_k^{\mathrm{core}} \right\rangle, \tag{3.29}$$

between the initial state $|\psi_o\rangle$ and the the energy-normalized S-matrix state[2] , Eq. (3.14):

$$\psi_k^{\mathrm{core}}(r,\Omega) = \frac{1}{r}\sum_i \Phi_i(\Omega) M_{ij}^{\mathrm{core}}(r) S_{jk}^{\mathrm{core}\dagger}. \tag{3.30}$$

This dipole vector $\vec{d}$, along with $\underline{S}^{\mathrm{core}}$ determine the short-range physics of the Rydberg electron. In both cases, it is a good approximation to calculate these on the real energy axis neglecting the external fields.

As in the cross section without external fields applied, Eq. (3.1), the energy smoothing is accomplished by evaluating the long-range S-matrix $\underline{S}^{\mathrm{LR}}(E + i\Gamma/2)$ at complex energies. This energy-smoothed S-matrix contains all of the effects of the external fields applied to the atom and, in general, must be determined by solving the long-range Schrödinger equation at complex energies. In a fully quantum mechanical calculation, this is a particularly difficult task because the nonseparable long-range Schrödinger equation must be solved anew at every energy $E + i\Gamma/2$. Therefore, this method is not particularly efficient when the exact quantum cross section is desired at high resolution. In fact, for single channel atoms, a number of other methods [70, 71, 73, 76] outperform my approach when calculating the infinite resolution cross section.

In spite of this difficulty, Eq. (3.28) is advantageous for a number of reasons. First it represents a completely general formula for treating atoms in external fields. It includes both the complications of a multichannel ionic core and the nonperturbative effect of an arbitrary configuration of external fields. As examples, Eq. (3.28) could be used to calculate anything from the Stark effect in argon to diamagnetism in the alkaline-earth atoms or crossed electric and magnetic field effects in the alkali-metal atoms. Second, Eq. (3.28) is amenable to semiclassical approximations. Although semiclassical approximations to Eq. (3.28) involve a number of unexpected subtleties (see Ch. 6), in the end, a simple result can be obtained. Third, Eq. (3.28) provides a clear picture of the physics involved when an atom

[2] An additional $\underline{S}^{\mathrm{core}\dagger}$ appears in Eq. (3.30) for the state $\left|\psi_k^{\mathrm{core}}\right\rangle$ used to define the dipole vector to be consistent with the dipole vectors used by other researchers [68, 105]. Alternatively, this S-matrix can be absorbed into the density of states matrix. When this is done, the ordering of $\underline{S}^{\mathrm{LR}}$ and $\underline{S}^{\mathrm{core}}$ in the cross section, Eq. (3.28), is reversed.

absorbs a photon in the presence of external fields. This physical insight is the subject of the next section.

The validity of the preconvolved photoabsorption cross section derived in this chapter, Eq. (3.28), can be verified by comparing its predictions with previous calculations and experiment. Such a comparison is given in Figs. 3.1 and 3.2 for hydrogen (deuterium) atoms in a 5.96 Tesla magnetic field. The preconvolved cross section shown in Fig. 3.2 has been calculated by using an accurate long-range S-matrix $\underline{S}^{\rm LR}$ in Eq. (3.28). The required S-matrix was calculated at complex energies ($\Gamma = 1.5 \times 10^{-7}$ a.u.) with the variational R-matrix technique of Ch. 4 to give the convolved cross section directly. The agreement between my calculations (Fig. 3.2) and the previous, infinite resolution calculations of Wunner *et al.* [108] shown in Fig. 3.1 is excellent. Also, the somewhat coarser resolution experimental data agrees with the predictions of both my own and the previous calculations [108].

3.2 Interpretation and discussion

The previous chapter introduced a physical picture of the motion of an atomic electron in external electromagnetic fields. After absorbing a photon, the atomic electron is placed in a quantum state that can be visualized as a combination of two time-independent scattering processes. The first involves the electron being launched inward to scatter off the multichannel ionic core to which it is bound. The second involves the electron being launched outward to scatter off the long-range Coulomb and external field potentials. The scattering matrices of the previous chapter encapsulate the quantum amplitudes for both of these scattering events. My formula, Eq (3.28), for the smoothed photoabsorption cross section shows exactly how this physical picture is manifested in the photoabsorption cross section.

3.2.1 Expansion of the cross section

The physical insight contained in the convolved cross section, Eq. (3.28), can be extracted by expanding the matrix $\left[\underline{1} - \underline{S}^{\rm core}\underline{S}^{\rm LR}\right]^{-1}$ in the cross section as a geometric series. After right multiplying the resulting series by the matrix $\left[\underline{1} + \underline{S}^{\rm core}\underline{S}^{\rm LR}\right]$, the cross section (3.28) becomes:

$$\sigma^{\Gamma}(E) = 4\pi^2\alpha\omega\,{\rm Re}\,\vec{d}\left[\underline{1} + 2\underline{S}^{\rm core}\underline{S}^{\rm LR} + 2\left(\underline{S}^{\rm core}\underline{S}^{\rm LR}\right)^2 + 2\left(\underline{S}^{\rm core}\underline{S}^{\rm LR}\right)^3 + \cdots\right]\vec{d}^{\dagger}. \qquad (3.31)$$

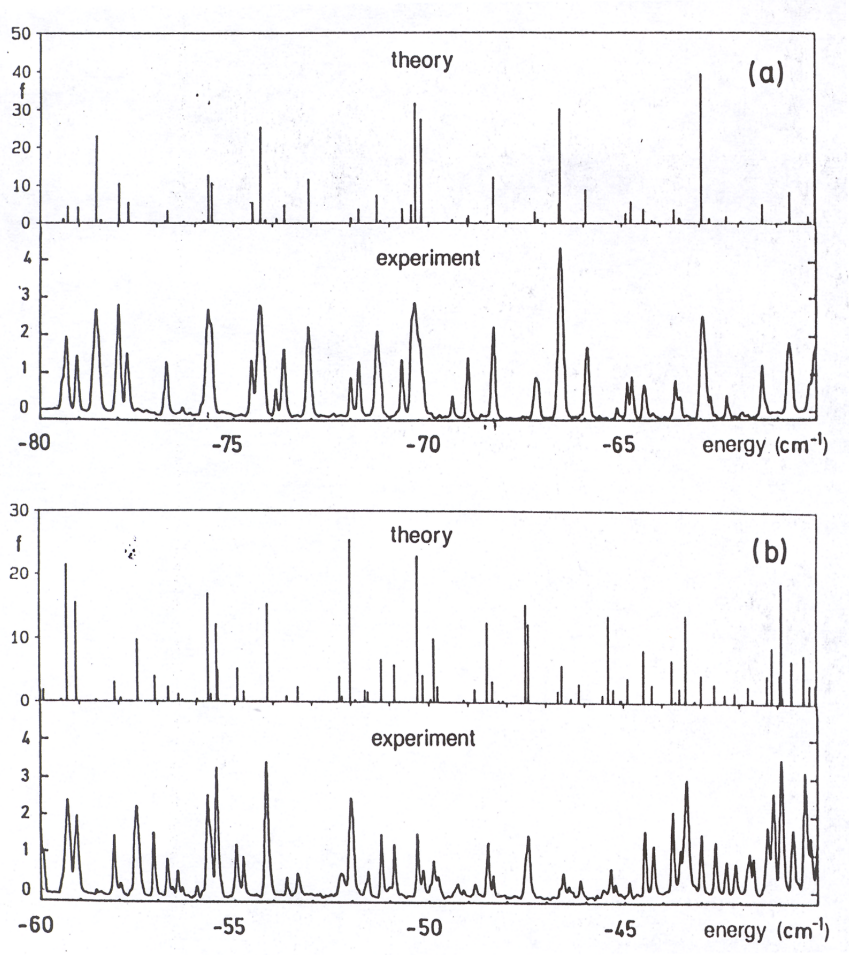

Figure 3.1: The theoretical and experimental photoabsorption spectra are shown for deuterium Rydberg atoms in an external magnetic field of 5.96 Tesla. Both the experiment and theory shown here are for $m = 0$, even parity final states of the electron. The large scale quantum calculations performed by Wunner *et al.* [108] are shown above the experimental spectra of Welge and coworkers [33]. The agreement between theory and experiment is good given the coarse resolution of the experiment. These results are shown for comparison with the method described in this chapter for calculating the photoaborption cross section (see Fig. 3.2). This figure is taken from [108].

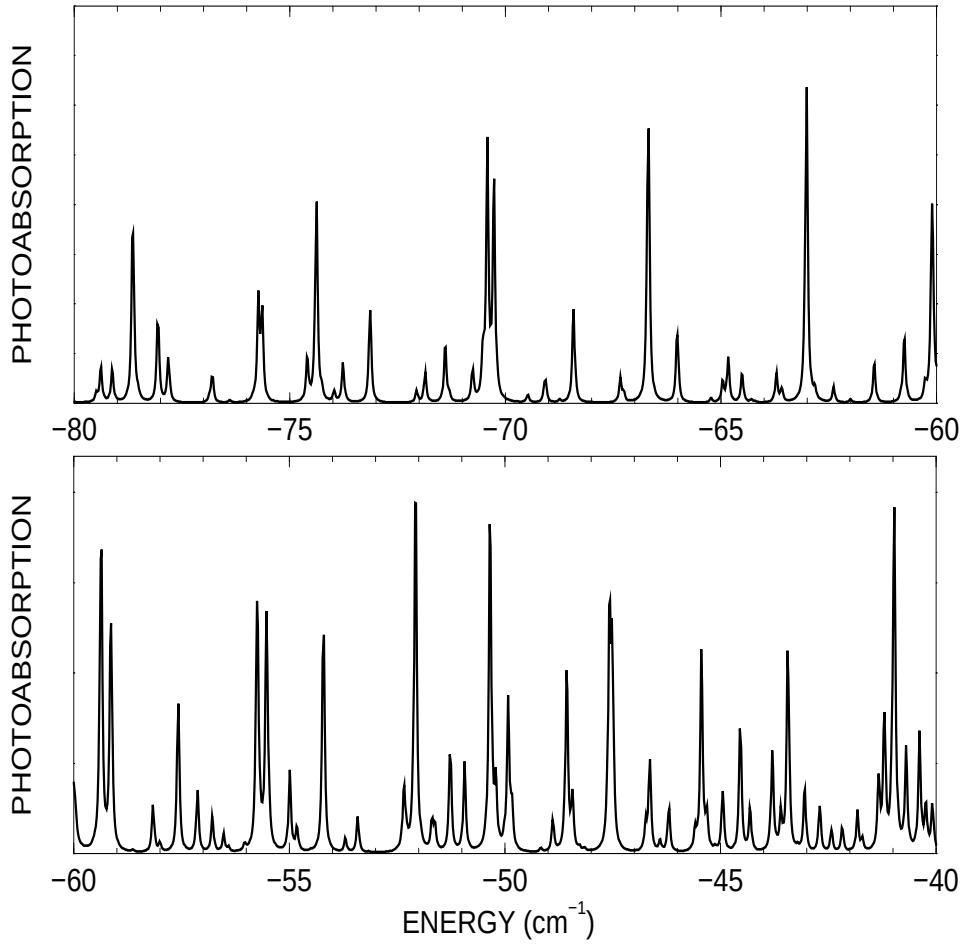

Figure 3.2: The convolved photoabsorption cross section is plotted for $m = 0$, even parity states of hydrogen in a 5.96 Tesla field. These calculations were performed using the accurate quantum S-matrices of Ch. 4 in the formula derived in this chapter, Eq. (3.28), for the cross section. The good agreement between these calculations and the theory and experiments shown in Fig. 3.1 shows that my S-matrix formulation of the photoabsorption process gives quantitatively accurate spectra. The highest energy in the spectrum (-40 cm^{-1}) corresponds to a scaled energy of $\epsilon = -0.4$ where approximately 90% of the classical phase space is chaotic.

This power series expansion of the cross section is the starting point in any interpretation, both semi-classical and quantum mechanical, of the photoabsorption process. As stated in the previous chapter, the S-matrices are simply quantum-mechanical amplitudes to scatter through a region of space a single time. Thus, the cross section can be viewed as an infinite sum over quantum-mechanical amplitudes associated with Feynman paths where the Rydberg electron scatters a single time $\left(\underline{S}^{\text{core}}\underline{S}^{\text{LR}}\right)$ or else multiple times $\left(\underline{S}^{\text{core}}\underline{S}^{\text{LR}}\cdots\underline{S}^{\text{core}}\underline{S}^{\text{LR}}\right)$ off the core and long-range regions. This recognition is the first step in understanding the electron's final state in a photoabsorption experiment.

It is important at this point to establish the convergence of the power series expansion of the cross section of Eq. (3.31). This can be studied by defining the norm of a matrix. The norm of a complex matrix $\underline{A}$ is defined by how it acts on the set of complex vectors $\vec{x}$ that have Euclidean norm less than unity [109]:

$$\|\underline{A}\| = \max_{|\vec{x}|\leq 1} |\underline{A}\vec{x}| \,. \tag{3.32}$$

Using this definition (3.32), the standard definitions of convergent series can be extended to series of matrices. It can be shown (see [109], exercise 3 of Sec. 1.3) that the geometric series of matrices,

$$\sum_{n=0}^{\infty}(\underline{S}^{\text{core}}\underline{S}^{\text{LR}})^n = (\underline{1} - \underline{S}^{\text{core}}\underline{S}^{\text{LR}})^{-1}, \tag{3.33}$$

converges absolutely if the following condition on the S-matrices is met:

$$\left\|\underline{S}^{\text{core}}\underline{S}^{\text{LR}}\right\| < 1. \tag{3.34}$$

Numerical evidence suggests that when the long-range S-matrix $\underline{S}^{\text{LR}}$ is calculated at complex energies with a small, positive imaginary part $i\Gamma/2$, the condition for convergence, Eq. (3.34), is satisfied. A general proof of this observation is still lacking and would be a desired result. This implies that the series expansion of the cross section (3.31) will always converge when accurate S-matrices are calculated as prescribed by the preconvolution theory. Any divergence of the series expansion of the cross section (3.31) should thus be related to inaccurate S-matrices. However, when there are questions about convergence, Eq. (3.34) can be checked once the S-matrices have been calculated.

The convergence of the expansion of the cross section given by Eq. (3.31) is significant in light of

other, semiclassical expansions of the cross section. Two extensions of closed-orbit theory by Dando *et al.* [53] and by Shaw and Robicheaux [54] have given series expansions of the photoabsorption cross section for one electron atoms other than hydrogen. From the start, these methods develop the cross section through a semiclassical approximation to a multiple scattering expansion. That is, their cross sections are derived term-by-term by iterating a semiclassical Born approximation-like scattering series. While these semiclassical expansions have been extremely successful for single channel atoms having one or two nonzero quantum defects, they are known to diverge rapidly for heavier atoms such as rubidium and barium [65]. It is unknown whether the divergences in their cross sections are due to the semiclassical approximation or the formulation of the series itself. Additionally, it is not obvious if their expressions have an exact (and hopefully convergent) quantum-mechanical generalization. My form of the cross section gives this generalization and shows that the exact cross section is naturally expressed as a convergent power series in the S-matrices $\underline{S}^{\mathrm{LR}}$ and $\underline{S}^{\mathrm{core}}$. Furthermore, the first form of the cross section, Eq. (3.28), shows that the power series can be summed to include all orders of scattering automatically.

In some respects, the convergence of the series in Eq. (3.31) is a purely mathematical property of the cross section. On the other hand, having a convergent series expansion of the photoabsorption cross section is physically relevant. Because the expansion given in Eq. (3.31) converges, a reasonable approximation for the full series can be found by including the first few terms of the series. Then each such term can be interpreted individually. This type of analysis is inspired by semiclassical methods such as closed-orbit theory where only a few short time closed orbit are needed to describe global oscillations of the energy domain cross section. As such, it is useful to show how my expansion of the cross section relates to standard closed-orbit theory.

3.2.2 Semiclassical approximations

A brief description of semiclassical approximations to the photoabsorption cross section shows how the series expansion in Eq. (3.31) can be interpreted in a term-by-term manner. A more thorough treatment of semiclassical approximations to the photoabsorption cross section is given in Chs. 5 and 6. The discussion here is only meant to introduce some of the general ideas of a semiclassical approximation

to the photoabsorption cross section.

A recurring theme in this thesis is that S-matrices are ideally suited to semiclassical approximations. Because of this, semiclassical approximations for the cross section will be derived (see Ch. 6) by introducing a semiclassical approximation for the long range scattering matrix, $\underline{S}^{\rm LR}(E)$. All of the short range parameters $(\underline{S}^{\rm core}, \vec{d})$ required for the cross section will typically be calculated in a fully quantum-mechanical framework as semiclassical approximations are not appropriate for these quantities [38]. In Ch. 6, I show that the general semiclassical expression for the long-range S-matrix,

$$\underline{S}^{\rm LR}(E) = \sum_k \underline{A}_k(E) e^{iS_k(E)}, \tag{3.35}$$

involves a sum over all classical trajectories that leave the matching region traveling radially outward, scatter classically of the long-range fields, and eventually return to the matching region after accumulating an action S_k. The matrix $\underline{A}_k(E)$ (see Ch. 5, Eq. (5.42)) is complex and contains information about the classical stability, the Maslov index, and also the initial and final polar angles of each of these trajectories. The number of trajectories summed over in Eq. (3.35) ranges from one with no external fields to infinitely many when an external magnetic field is applied to the atom. Also, it should be remembered that all of the quantities in Eq. (3.35) $(\underline{A}_k, S_k)$ depend on the external fields applied to the atom.

Using the semiclassical expression for $\underline{S}^{\rm LR}$ (3.35) in the expansion of the cross section (3.31) gives the **primitive semiclassical approximation** for the photoabsorption cross section:

$$\sigma^{\Gamma}(E) = 4\pi^2\alpha\omega\,{\rm Re}\,\vec{d}\left(\underline{1} + 2\sum_i \underline{S}^{\rm core}\underline{A}_i e^{iS_i} + 2\sum_{i,j}\underline{S}^{\rm core}\underline{A}_i\underline{S}^{\rm core}\underline{A}_j e^{i(S_i+S_j)}\cdots\right)\vec{d}^{\dagger}. \tag{3.36}$$

When this cross section is plotted in a small interval near an energy E' and Fourier transformed to the time domain, the resulting **recurrence spectrum** shows strong peaks at the periods $T_i(E')$ of primitive closed-orbits and at the combined periods (such as $T_i(E') + T_j(E')$ and $T_i(E') + T_j(E') + T_k(E')$) of those primitive orbits. This is made possible because the amplitudes $\underline{A}_i$ vary slowly with energy. Thus my form of the cross section (3.31), when combined with semiclassical approximations for $\underline{S}^{\rm LR}$ (3.35) reproduces the physical content of closed-orbit theory. A small energy interval about E' is required because the periods $T_i(E)$ depend on the energy. This allows the actions in Eq. (3.36) to be expanded

about the point $\tilde{E}$,

$$S_i(E) \approx S_i(E') + (E - E') \left.\frac{dS_i}{dE}\right|_{E'} = S_i(E') + (E - E')T_i(E'),$$

so that the Fourier transform operates on terms such as $e^{i(E-E')T_i}$ to give the strong peaks in the time domain.

A better alternative to Fourier transforming the spectra with respect to energy is to perform the analysis using scaled variables. This approach was first used by Holle *et al.* [35] to study the recurrence spectrum of diamagnetic hydrogen. In Appendix A, I give the details of this scaling transformation for an electron in an external magnetic field. The only important point here is that the scaling transformation replaces the energy E, magnetic field strength B, and classical action S_i by a scaled field w, scaled energy ϵ, and scaled action $\tilde{S}_i$:

$$w = 2\pi B^{-1/3}, \tag{3.37}$$

$$\epsilon = EB^{-2/3}, \tag{3.38}$$

$$\tilde{S}_i = S_i/w. \tag{3.39}$$

In scaled variable recurrence spectroscopy [35, 39], the photoabsorption cross section is measured or calculated at a fixed scaled energy ϵ as a function of the scaled field variable w. This amounts to varying both the energy E and the field B along lines of fixed ϵ. The resulting cross section $\sigma(w)$,

$$\sigma^{\Gamma}(w) = 4\pi^2\alpha\omega \,\mathrm{Re}\, \vec{d}^{\dagger} \left(\underline{1} + 2\sum_i \underline{A}_i \underline{S}^{\mathrm{core}} e^{iw\tilde{S}_i} + 2\sum_{i,j} \underline{A}_i \underline{S}^{\mathrm{core}} \underline{A}_j \underline{S}^{\mathrm{core}} e^{iw(\tilde{S}_i + \tilde{S}_j)} \cdots \right) \vec{d}. \tag{3.40}$$

is then Fourier transformed with respect the the variable w to obtain the scaled recurrence spectrum. Because the scaled actions $\tilde{S}_i$ do not depend on the variable w (see Appendix A), a clean Fourier transform over a large range of w can be obtained. Like the time domain Fourier transformation, the scaled recurrence spectrum shows peaks at the scaled actions $\tilde{S}_i$ of the primitive closed-orbits, of their repetitions ($\tilde{S}_i + \tilde{S}_i + \cdots$) and of their combinations ($\tilde{S}_i + \tilde{S}_j + \cdots$). Again, I emphasize that my primitive semiclassical approximation to the cross section, Eq. (3.36) or (3.40), echos the physical content of closed-orbit theory; each closed orbit in the long-range region contributes an oscillating term to the total cross sec-

tion. However, as Ch. 6 elucidates, this primitive semiclassical approximation is flawed and needs to be repaired to obtain a quantitatively accurate semiclassical theory for the photoabsorpton cross section.

3.2.3 Conclusion

This final section has explored some of the properties of the main result of the chapter, Eq. (3.28), which gives an expression for the convolved photoabsorption cross section for an atom in external electric and magnetic fields. Specifically, I have introduced a series expansion for the cross section (3.31) and explored its convergence properties and relationship to previous semiclassical approaches. The beauty of semiclassical approaches is that they give a simple interpretation of the time (or scaled action) domain cross section. However, my formula for the convolved cross section is an exact quantum-mechanical result.

Taking hints from semiclassical approaches to interpreting the cross section, a new method of interpreting the exact quantum cross section can be deduced. By using accurate quantum-mechanical S-matrices and Fourier transforming individual terms in the series (3.31) (like $\vec{d}^{\dagger}\underline{S}^{\mathrm{LR}}\underline{S}^{\mathrm{core}}\vec{d}$) one can investigate the separate contributions made by each to the total quantum recurrence spectrum. While it is expected that this quantum analysis will show many features in common with the semiclassical recurrence spectra, other features - nonclassical in nature - can be detected and studied using this approach. An example of this approach will be given in Ch. 6, where I explore the semiclassical approximation to the cross section further. Before this analysis can be given, however, I show how the long range S-matrix $\underline{S}^{\mathrm{LR}}$ can be calculated for an atomic electron in a external magnetic field.

Chapter 4

Quantum scattering matrices

Chapters 2 and 3 have focused on the basic properties of the scattering matrices $\underline{S}^{\rm LR}$ and $\underline{S}^{\rm core}$, and their relationship to the observables of an atom in external electric and/or magnetic fields. Simple formulas for both the bound state spectrum, Eq. (2.26), and the total photoabsorption cross section, Eq. (3.28), have been given in terms of these S-matrices. Clearly, for these results to be useful the S-matrices must be calculated. This chapter and the next give the details of how the long-range S-matrix $\underline{S}^{\rm LR}$ can be calculated using either a fully quantum mechanical approach (this chapter) or a semiclassical approximation similar to closed-orbit theory (Ch. 5).

At this point, it is worth reiterating an important point about the total photoabsorption cross section (3.28) derived in Ch. 3: it is an exact result that applies to any multichannel atom in any configuration of external electric and magnetic fields. This generality of my approach is one of its main strengths. However, to explore the physics contained in the photoabsorption cross section, it is useful to specialize to a narrower class of experiments. Consequently, the remainder of the thesis concentrates on the properties of a single channel atom in a static, external magnetic field. Once the S-matrices have been calculated for this system, the physics of the photoabsorption process can be studied.

For single channel atoms, such as the alkali-metal atoms, the core-region S-matrix is parametrized in terms of the quantum defects μ_l [50]:

$$S^{\rm core}_{ll'} = \delta_{ll'} e^{2\pi i \mu_l}.$$

This is a standard result from quantum-defect theory and the quantum defects for simple atoms are

available in many articles and books [96, 110]. While my formulation of the photoabsorption cross section applies to multichannel atoms, the physics of core-scattered peaks in recurrence spectra must be understood before these difficult cases can be treated. Single channel atoms provide an ideal setting to explore core scattering because all of the effects of the ionic core are parameterized by a few energy independent quantum defects. At this point, I only mention that for multichannel atoms the core-region S-matrix can be determined using well understood methods of quantum-defect theory, R-matrix theory and frame transformations [68]. These techniques are applicable immediately as the external fields are can be neglected in the core-region. Also note that quantum mechanical effects such as spin and the Pauli exclusion principle make semiclassical approximations more difficult for the core-region physics encapsulated in $\underline{S}^{\text{core}}$.

The long-range physics presents more of a challenge than the short range physics. The main difficulty is that in this region, the electronic Hamiltonian,

$$H = -\frac{1}{2}\nabla^2 - \frac{1}{r} + \frac{1}{2}B\hat{L}_z + \frac{1}{8}B^2\rho^2, \tag{4.1}$$

is nonseparable in two dimensions (ρ, z). When an electron is highly excited, the two dimensional Schrödinger equation of Eq. (4.1) must be solved over a vast region of configuration space. More specifically, below the ionization threshold, $\underline{S}^{\text{LR}}$ can be determined after the Schrödinger equation is solved in a spherical shell bounded by the radii $r_0 < r < r_{max}$. Typically r_0 is somewhere in the matching region $r_0 \approx 10 - 100$ a.u. (Ch. 2) and r_{max} is somewhere well beyond the classical turning point of the electron where the wavefunction has decayed to zero. A good estimate for the size of r_{max} is given by the formula,

$$r_{max} \approx 3\nu^2, \tag{4.2}$$

where $\nu = 1/\sqrt{-2E}$ is the effective quantum number of the electron. As an example, for a $\nu = 200$ electron, the outer radius r_{max} is an extraordinary 120,000 a.u. or $\approx 6\,\mu$m. Besides the large region of space required and the two-dimensional, nonseparable Schrödinger equation that must be solved, there are two other difficulties in calculating $\underline{S}^{\text{LR}}$. First, because $\underline{S}^{\text{LR}}$ is a strongly varying function of the energy, the Schrödinger equation must be solved at every energy at which the cross section is

desired. Second, because the preconvolved cross section requires $\underline{S}^{\mathrm{LR}}$ at complex energies $E + i\Gamma/2$, the solutions of the Schrödinger equation will be complex valued. This necessitates the costly use of complex arithmetic in the numerical implementation of the method.

While these difficulties slow computational efforts, no significant conceptual difficulties exist in carrying out the calculations of $\underline{S}^{\mathrm{LR}}$ at complex energies. In fact, a number of researchers have performed similar calculations [71, 76] for diamagnetic atoms using the time tested approach of R-matrix theory [111, 112, 113, 68]. My approach to calculating $\underline{S}^{\mathrm{LR}}$ follows this previous work with two differences. First, to obtain the preconvolved cross section directly from Eq. (3.28) variational R-matrix theory is extended to complex energies. Usually, the infinite resolution cross section is calculated with R-matrix calculations on the real energy axis, after which the convolved cross section is obtained by a numerical convolution. Because my preconvolved S-matrix approach for the cross section requires calculations at complex energies, it is generally slower at calculating the infinite resolution cross section than other approaches. However, the complex energy calculations described in this chapter have a distinct advantage in obtaining the convolved cross section. Second, my treatment is the first to package the solutions of the Schrödinger equation for the long-range region into an S-matrix. Most previous work has used R-matrices instead of S-matrices for this purpose. The main advantage of a long-range S-matrix is that all the interpretive tools of semiclassical approximations can be used to understand the physics contained in the S-matrix. This gives a simple picture of the quantum mechanics associated with the nonintegrable electronic motion. Interpretation of the long range R-matrix is far less transparent.

This chapter develops the necessary extensions of variational R-matrix theory needed to calculate $\underline{S}^{\mathrm{LR}}$ at complex energies for an atom in an external magnetic field. The basic ideas of R-matrix theory can be found in a number of articles so the more familiar parts of the theory will only be sketched. After the method for finding $\underline{S}^{\mathrm{LR}}$ has been described, calculations that implement this method are presented and discussed. The most important result of these calculations is that the physics contained in the exact quantum mechanical $\underline{S}^{\mathrm{LR}}$ can be extracted using the ideas of recurrence spectroscopy. Fourier transformation of $\underline{S}^{\mathrm{LR}}$ then permits an identification of the most important quantum mechanical paths of the electron as it scatters off the long-range fields.

4.1 Variational S-matrix approach

Calculation of the long-range S-matrix involves two steps. The first is to solve the Schrödinger equation,

$$\hat{H}\psi(\vec{x}) = E\psi(\vec{x}), \tag{4.3}$$

in the long-range region for the Hamiltonian of Eq. (4.1). After numerical long-range solutions of Eq. (4.3) are obtained, $\underline{S}^{\mathrm{LR}}$ can be determined by a simple matching procedure. Both of these steps can be carried out using variational R-matrix theory. This technique has been developed [114, 115, 116] as an extension of the R-matrix theory of Wigner and Eisenbud [113]. In most situations, the Schrödinger equation (4.3) is solved (for a bound state) by imposing boundary conditions upon the wavefunction and then finding a discrete set of energy eigenvalues. In variational R-matrix theory this procedure is turned around: here, the **energy** is set beforehand and the Schrödinger equation is solved in a volume V to determine the **boundary conditions** of the wavefunction on the surface S of the volume. This information about the boundary conditions of wavefunction on the surface is encoded in the normal logarithmic derivative $-b$ of the wavefunction on the surface:

$$-b = \frac{\partial\psi}{\partial n}\frac{1}{\psi}. \tag{4.4}$$

Here, $\hat{n}$ denotes the outward unit vector normal to the surface. The main tool of variational R-matrix theory is a variational principle for this logarithmic derivative (4.4). This provides an efficient algorithm for finding the wavefunction ψ and its logarithmic derivative $-b$ on a given surface S. In the following subsection, the details of this approach are sketched for the long-range motion of an atomic electron in an external magnetic field. After that, the long range S-matrix $\underline{S}^{\mathrm{LR}}$ is extracted from the results of the R-matrix calculation.

4.1.1 Solving the Schrödinger equation

The first step in R-matrix theory is to identify the volume V (and surface S) over which the Schrödinger equation (4.3) must be solved. As mentioned before, for a calculation of $\underline{S}^{\mathrm{LR}}$, a spherical

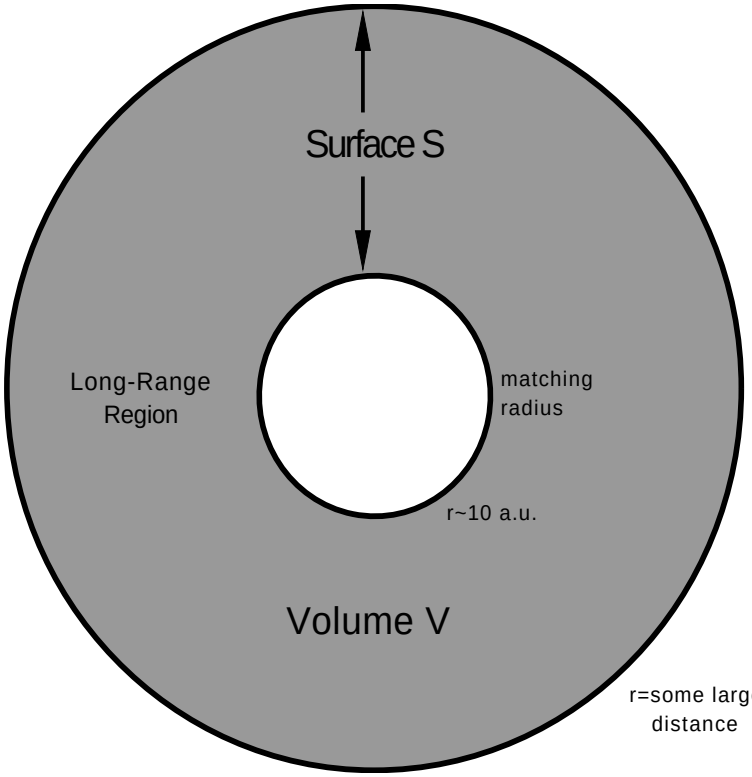

Figure 4.1: This diagram depicts the volume V of configuration space in which the Schrödinger equation must be solved to find the long-range S-matrix. The volume is bounded by the radii r_0 and r_{max}, where r_0 is somewhere in the matching region and r_{max} is a large distance beyond the classical turning point of the electron. The Hamiltonian in this volume, Eq. (4.1), involves both the Coulomb and diamagnetic potentials.

shell bounded by the radii r_0 (in the matching region) and r_{max} (some large distance where the wavefunction has decayed to zero) is appropriate. The surface S of this volume has two parts: a sphere S_1 at $r = r_0$ having $\hat{n} = -\hat{r}$ and a sphere S_2 at $r = r_{max}$ having $\hat{n} = \hat{r}$. This volume used in the R-matrix calculations for $\underline{S}^{\mathrm{LR}}$ is depicted in Fig. 4.1.

The standard formulas of variational R-matrix theory [68] apply to this case without major modifications. This technique begins with a variational principle, first derived by Kohn [117] and later by Greene [116], for the logarithmic derivative $-b$ of the wavefunction ψ on the surface S,

$$b = \frac{2\int dV\psi^*(E-\hat{H})\psi - \int dS\psi^*\frac{\partial\psi}{\partial n}}{\int dS\left|\psi\right|^2}. \tag{4.5}$$

As stated above, the energy E of the electron is a parameter in this equation and has a complex value of $E + i\Gamma/2$ to accomplish the energy preconvolution of the cross section. Here and elsewhere, I use a flexible notation where at times E is the full complex valued energy (as in Eq. (4.5)) and at other times E is only the real part of the energy (implied in $E + i\Gamma/2$). The context will determine which of these meanings is appropriate.

As is true of the Rayleigh-Ritz variational principle for the bound state energies of a Hamiltonian, the variational principle for b (4.5) can be converted to a generalized eigenvalue problem. This is done by expanding the βth linearly independent wavefunction $\psi_\beta(\vec{x})$ in a set of N basis functions $y_i(\vec{x})$ and undetermined coefficients $c_{i\beta}$:

$$\psi_\beta(\vec{x}) = \frac{1}{r}\sum_{i=1}^{N} y_i(\vec{x})c_{i\beta}. \tag{4.6}$$

The resulting eigensystem,

$$\underline{\Gamma}\vec{c}_\beta = b_\beta\underline{\Lambda}\vec{c}_\beta, \tag{4.7}$$

is written in terms of the matrices

$$\Gamma_{ij} = 2\int_V y_i^*(\vec{x})\left(E-\hat{H}\right)y_j(\vec{x})dV - \oint_S y_i^*(\vec{x})\frac{\partial y_j(\vec{x})}{\partial n}dS \tag{4.8}$$

and

$$\Lambda_{ij} = \oint_S y_i^*(\vec{x})y_j(\vec{x})dS. \tag{4.9}$$

It is important not to confuse the matrix $\underline{\Gamma}$ with the smoothing width Γ, which is always a scalar. As usual, the factor $1/r$ is used in the wavefunction of Eq. (4.6) to eliminate the first derivatives $\partial/\partial r$ in the Hamiltonian operator $\hat{H}$ in Eq. (4.8). This explicit $1/r$ factor in the wavefunction has three auxiliary effects on the above expressions. First, the infinitesimal volume element dV in Eq. (4.8) no longer has the usual r^2 factor found in spherical polar coordinates, so that $dV = dr d\theta d\phi \sin\theta$. Second, the logarithmic derivative in Eq. (4.7) is defined with respect to $r\psi_\beta$ rather than simply ψ_β:

$$-b_\beta = \frac{\partial(r\psi_\beta)}{\partial n}\frac{1}{r\psi_\beta}. \tag{4.10}$$

Third, the radial part of the kinetic energy operator in $\hat{H}$ has the form $-(1/2)d^2/dr^2$. Solving the eigensystem of Eq. (4.7) yields the logarithmic derivative b_β (4.10) and the coefficient matrix $c_{i\beta}$ (4.6) of the βth linearly independent solution of the Schrödinger equation in the volume V.

While the eigenvalue system for b_β, Eq. (4.7), can be solved directly, a more efficient approach is to partition the matrices $\underline{\Gamma}$ and $\underline{\Lambda}$ into open and closed subspaces [68]. The open subspace, denoted by a subscript "o," consists of the few (N_o) basis functions that are nonzero on the surface at r_0. The remaining $N_c = N - N_o$ basis functions, denoted by the subscript "c", are zero on this boundary and make up the closed subspace. In this partitioned notation, the eigensystem, Eq. (4.7), becomes,

$$\begin{pmatrix} \underline{\Gamma}_{cc} & \underline{\Gamma}_{co} \\ \underline{\Gamma}_{oc} & \underline{\Gamma}_{oo} \end{pmatrix} \begin{pmatrix} \vec{c}_{c\beta} \\ \vec{c}_{o\beta} \end{pmatrix} = b_\beta \begin{pmatrix} 0 & 0 \\ 0 & \underline{\Lambda}_{oo} \end{pmatrix} \begin{pmatrix} \vec{c}_{c\beta} \\ \vec{c}_{o\beta} \end{pmatrix}. \tag{4.11}$$

This leads to a small eigensystem in the open subspace for the logarithmic derivative b,

$$\underline{\Omega}_{oo}\vec{c}_{o\beta} = b_\beta \underline{\Lambda}_{oo}\vec{c}_{o\beta}, \tag{4.12}$$

where the matrix $\underline{\Omega}_{oo} = \underline{\Gamma}_{oo} - \underline{\Gamma}_{oc}\underline{\Gamma}_{cc}^{-1}\underline{\Gamma}_{co}$ requires a calculation of the inverse $\underline{\Gamma}_{cc}^{-1}$ in the larger closed subspace. The computational advantage of this partitioned notation is that the product $\underline{X}_{cc} = \underline{\Gamma}_{cc}^{-1}\underline{\Gamma}_{co}$ can be found as the solution of the linear system,

$$\underline{\Gamma}_{cc}\underline{X}_{co} = \underline{\Gamma}_{co}. \tag{4.13}$$

All of these results are standard formulas in variational R-matrix theory. The only modification that my calculations require is that the matrix $\underline{\Gamma}$, defined in Eq. (4.8) and used in Eqs. (4.11-4.13), is evaluated at complex energies $E + i\Gamma/2$, so that the final eigenvectors $\vec{c}_\beta$ and logarithmic derivatives b_β are complex.

An important technical detail in solving the R-matrix equations is the choice of an appropriate set of basis functions $y_i(\vec{x})$. To calculate the long-range S-matrix $\underline{S}^{\mathrm{LR}}$, I use L spherical harmonics $Y_{lm}(\theta,\phi)$ for the angular degrees of freedom and P basis splines $B_p(r)$ [118] for the radial degree of freedom:

$$y_i(\vec{x}) = Y_{lm}(\theta,\phi)B_p(r),$$

$$l = \{0, 2, \ldots, 2L-2)\} \quad \text{(even parity)},$$

$$l = \{1, 3, \ldots, 2L-1\} \quad \text{(odd parity)},$$

$$p = \{1, \ldots, P\},$$

$$i = \{l, m, p\} = \{1, \ldots, N = LP\}.$$

Only one value of m is present in the expansion of the wavefunction because the Hamiltonian, Eq. (4.1), is symmetric under rotations about the z-axis. And, because spin-orbit and hyperfine effects are neglected, the Hamiltonian (4.1) is invariant under the parity operation $z \rightarrow -z$ so that only odd or else only even parity spherical harmonics are needed. The spherical harmonics are convenient because they also serve as channel functions on the sphere at $r = r_0$, where the physics is purely Coulombic.

The basis (or B) splines are a convenient set of locally defined functions that can represent the radial part of the wavefunction. Here, only their properties that are relevant for solving the Schrödinger equation for the case at hand are presented. The reader is referred to the text of de Boor [118] for a formal discussion of their many mathematical properties. Examples of their use in atomic physics can be found in the article of Sapirstein and Johnson [119]. For the radial wavefunction, a set of P B-splines of order k is used. These splines, which are polynomials of order k locally, are defined on a radial mesh of N_r points on the interval $[r_0, r_{max}]$. Given the number of mesh points N_r and the order of spline k, the number of splines is constrained to be $P = N_r + k - 1$. The details of the splines are determined by how the set of mesh points is chosen. I use a convention where the mesh points at the limits of the interval

are repeated k times. With this choice, there is a single spline nonzero at each boundary ($B_1(r_0) = 1$ and $B_P(r_{max}) = 1$), and all others are zero at r_0 and r_{max}. The advantage of choosing the splines in this manner is that the boundary conditions on the wavefunction at r_0 and r_{max} can be imposed without difficulty. Below threshold, the wavefunction must vanish at the outer radius r_{max}. This is accomplished by excluding the last spline B_P from the expansion of the wavefunction. At the inner boundary r_0 there are two possibilities. For channels in the closed subspace, the wavefunction is zero on the surface $r = r_0$ so that the nonzero spline B_1 is again excluded for these channels. However, in the open channels, this spline must be kept to represent finite values of the logarithmic derivatives b_β on the surface.

This choice of basis functions leads to an efficient method of solving the large linear system, Eq. (4.13), and the smaller eigensystem, Eq. (4.12), of R-matrix theory. This is the case because the spherical harmonics and B-splines lead to a highly banded matrix structure for the large matrix $\underline{\Gamma}_{cc}$. The only term in the Hamiltonian that is nondiagonal in the spherical harmonic basis is the diamagnetic term $\frac{1}{8}B^2r^2\sin^2\theta$, which couples angular momentum l to $l \pm 2$. The angular matrix elements of the diamagnetic term can be worked out analytically in terms of the 6j coefficients [120]:

$$\left\langle lm \left| \sin^2\theta \right| l'm \right\rangle = \frac{2}{3}\left(\delta_{ll'} - (-1)^m \sqrt{(2l+1)(2l'+1)} \begin{Bmatrix} l & l' & 2 \\ 0 & 0 & 0 \end{Bmatrix} \begin{Bmatrix} l & l' & 2 \\ -m & m & 0 \end{Bmatrix} \right).$$

The radial matrix elements in $\underline{\Gamma}$ (4.8) and $\underline{\Lambda}$ (4.9) involve integrals over the B-splines and their derivatives. These matrix elements are calculated numerically using Gaussian quadrature. The values of the B-splines and their derivative needed for the integrals can be generated rapidly using the Fortran routines listed in the text of de Boor [118]. Most importantly, for kth order splines, each spline overlaps with only $k-1$ other splines. These properties of the spherical harmonics and B-splines lead to a matrix $\underline{\Gamma}_{cc}$ with a total bandwidth of $4P + 2k - 9$. Thus, even though the matrix $\underline{\Gamma}_{cc}$ is of order $L \times P$, the linear system involving this matrix, Eq. (4.13), can be solved efficiently using the banded matrix routines found in the LAPACK Fortran library [121].

In numerical tests I have found that for an electron at energy $E = -1/2\nu^2$ using $\nu/2$ spherical harmonics of a given parity ($L = \nu/2$) and 4ν B-splines ($P = 4\nu$) gives about 4 digits of accuracy in the long-range S-matrix. Almost always, B-splines of order $k = 5$ are sufficient. These guidelines

for picking the number of basis functions (and the order of splines) leads to a closed subspace of order $N_c \approx 2\nu^2$ and a total bandwidth of $16\nu + 2k - 9$ for the matrix $\underline{\Gamma}_{cc}$. As an example, for $\nu = 50$, the solution of the large linear system, Eq. (4.13), at each energy takes ≈ 30 seconds of CPU time and ≈ 150 Mb of memory on a 633 Mhz Compaq Alpha workstation. Because the open subspace is typically of order $N_o \approx 5 - 10,$ the small eigenvalue problem, Eq. (4.12), takes only a fraction of a second. Next I describe how the long-range S-matrix $\underline{S}^{\rm LR}$ can be found, once the R-matrix equations have been solved to give b_β and $c_{i\beta}$.

4.1.2 Finding the S-matrix

Solution of the R-matrix equations above constitutes the main computational work involved in calculating the long-range S-matrix. Once these calculations have been performed, the multichannel radial wavefunction $F_{i\beta}(r)$ on the surface $r = r_0$ takes the simple form:

$$F_{i\beta}(r_0) = c_{i\beta}. \tag{4.14}$$

Furthermore, this form of the wavefunction (4.14), along with the definition of the logarithmic derivative $-b_\beta$ (4.10) yields the radial derivative of the wavefunction on the boundary:

$$\frac{\partial F_{i\beta}(r_0)}{\partial r} = c_{i\beta} b_\beta, \tag{4.15}$$

where one must take into account that $\hat{n} = -\hat{r}$ on the surface $r = r_0$ to get this result. As described in Ch. 2, $\underline{S}^{\rm LR}$ emerges when this numerically determined solution is matched to the S-matrix state, Eq. (2.18):

$$\underline{M}^{\rm LR}(r) = \frac{1}{i\sqrt{2}} \left[\underline{f}^-(r) \underline{S}^{\rm LR} - \underline{f}^+(r) \right]. \tag{4.16}$$

In the matching region, where the electron moves in a pure Coulomb potential, the numerical wavefunction, Eq. (4.14), can be written in terms of the Coulomb functions (f_l^+, f_l^-) and constant coefficient matrices $\underline{P}$ and $\underline{Q}$ (see Eq. (4.17)):

$$F_{i\beta}(r_0) = c_{i\beta} = \frac{1}{i\sqrt{2}} \left[f_i^+(r_0) P_{i\beta} - f_i^-(r_0) Q_{i\beta} \right]. \tag{4.17}$$

Taking the Wronskian of this wavefunction (4.17) with $f_i^+(r)$ and $f_i^-(r)$ gives the coefficient matrices $\underline{P}$ and $\underline{Q}$ in terms of the R-matrix solution matrix $c_{i\beta}$:

$$P_{i\beta} = \frac{\pi}{\sqrt{2}} \quad \mathrm{W}\left[f_i^+, c_{i\beta}\right]_{r_0} = \frac{\pi}{\sqrt{2}}\left(f_i^+(r_0)b_{i\beta} - f_i^{+\prime}(r_0)\right)c_{i\beta}, \tag{4.18}$$

$$Q_{i\beta} = \frac{\pi}{\sqrt{2}} \quad \mathrm{W}\left[f_i^-, c_{i\beta}\right]_{r_0} = \frac{\pi}{\sqrt{2}}\left(f_i^-(r_0)b_{i\beta} - f_i^{-\prime}(r_0)\right)c_{i\beta}. \tag{4.19}$$

Finally, the long-range S-matrix can be written in terms of these numerical coefficients, Eqs. (4.18) and (4.19):

$$\underline{S}^{\mathrm{LR}} = \underline{P}\underline{Q}^{-1}. \tag{4.20}$$

I emphasize that all of the quantities in the above discussion (b_β, $c_{i\beta}$, $P_{i\beta}$ and $Q_{i\beta}$) are strongly varying functions of both the magnetic field B and the complex valued energy $E + i\Gamma/2$. Thus, this entire procedure must be repeated at each energy. In principle, the Coulomb functions (f_l^+, f_l^-) and their derivatives in Eqs. (4.18) and (4.19) must also be evaluated at complex energies. However, at the moderate distances in the matching region ($10 < r_0 < 100$) the Coulomb functions at complex energies can be approximated by their values on the real energy axis without any sacrifice in the accuracy in the final S-matrix, Eq. (4.20). A justification of this approximation is given in Fig. 4.2, which plots the regular and irregular Coulomb functions at a complex energy typical of what is required for the preconvolution of the S-matrix and cross section. The upper graph shows the imaginary parts of (f, g), which vanish at real energies. Because these imaginary parts are orders of magnitude smaller that the real parts the Coulomb functions $f^\pm = (-g \pm if)/\sqrt{2}$ in the matching region can be calculated on the real energy axis. However, if the complex energy Coulomb functions are needed, they can be calculated with formulas given by Robicheaux [105].

One final detail about the numerically calculated $\underline{S}^{\mathrm{LR}}$ needs to be addressed. A certain amount of flexibility exists in how the dimensionality of $\underline{S}^{\mathrm{LR}}$ is chosen. When $\underline{S}^{\mathrm{LR}}$ is initially calculated, it must include all of the channels that are locally open (classically allowed) and weakly closed on the surface at $r = r_0$. This number of channels N_o determines the size of the open subspace in the R-matrix calculations and is typically a few more than the maximum classical allowed angular momentum l_{max}

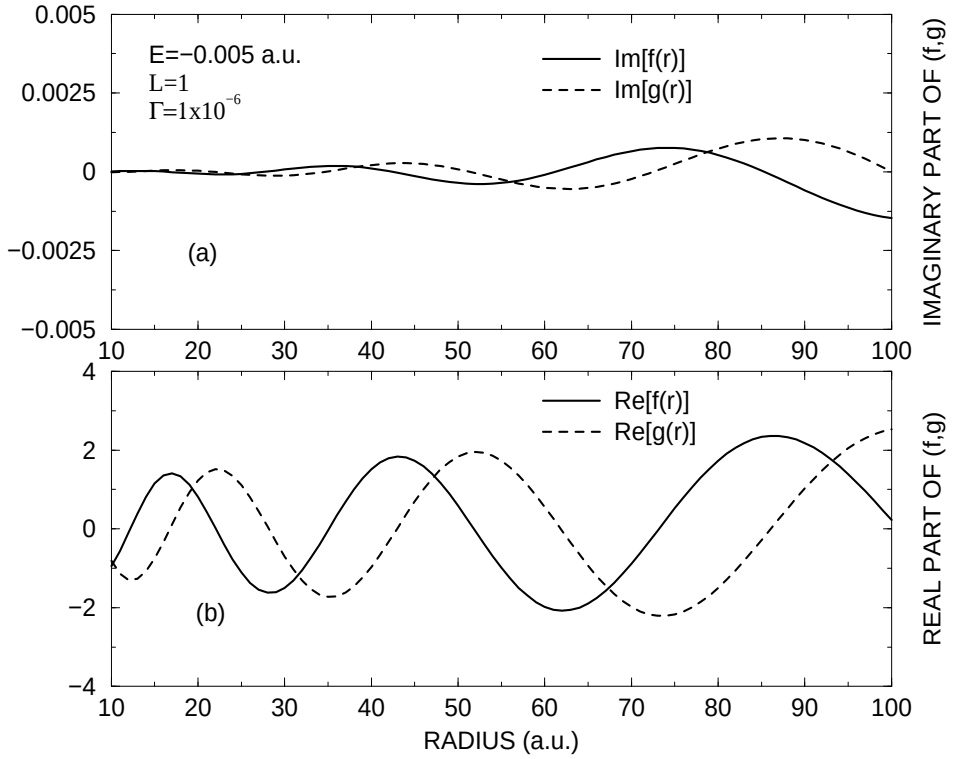

Figure 4.2: The real (bottom) and imaginary (top) parts of the regular (solid line) and irregular (dotted line) Coulomb functions (f, g) are plotted at a complex energy $E = -0.0005 + 0.5 \times 10^{-6} i$ and angular momentum $l = 1$. On the real energy axis, these two Coulomb functions are real-valued. This figure shows that when the energy is complex, these Coulomb functions develop small imaginary parts that increase with the radius r. The traveling wave Coulomb functions used in Eqs. (4.18) and (4.19) to find the long-range S-matrix are related to these functions through the relation $f^{\pm} = (-g \pm if)/\sqrt{2}$. Technically, the complex energy Coulomb functions shown in this figure should be used (through $f^{\pm}$) to find the preconvolved S-matrix $\underline{S}^{\mathrm{LR}}$. However, because the imaginary parts of (f, g) are orders of magnitude smaller than the real parts, it is a good approximation to use the Coulomb functions at real energies. It is important to note that this approximation is only good at small radii; as r is increased, the imaginary parts of f and g eventually overtake the real parts. Thus, by keeping the matching radius small ($r_0 \approx 10$ a.u.), the complications of calculating the Coulomb functions at complex energies can be avoided.

on the matching surface:

$$l_{\text{max}} = \sqrt{2r_0^2\left(E + \frac{1}{r_0}\right)} - \frac{1}{2}. \tag{4.21}$$

However, all of these $N_o \approx l_{max}$ channels are not needed explicitly in the formula for the photoabsorption cross section, Eq. (3.28). This is because the short range parameters $\vec{d}$ and $\underline{S}^{\text{core}}$ used in the cross section are typically trivial (0 or 1) beyond the first few channels. For example, in Li the quantum defects are $\mu_s = 0.4$ and $\mu_p = 0.04$; all others are smaller than 0.01. As Harmin [83] has shown, the "extra" channels in $\underline{S}^{\text{LR}}$ can be eliminated using the tools of quantum-defect theory. This is desirable because the wavefunction in these weakly closed channels becomes exponentially large at small distances. Labeling the unwanted channels by the subscript "x" (for extra) and those to be maintained by the subscript "p" (for physical), $\underline{S}^{\text{LR}}$ can be written in a partitioned notation,

$$\underline{S}^{\text{LR}} = \begin{pmatrix} \underline{S}^{\text{LR}}_{pp} & \underline{S}^{\text{LR}}_{px} \\ \underline{S}^{\text{LR}}_{xp} & \underline{S}^{\text{LR}}_{xx} \end{pmatrix}, \tag{4.22}$$

where the total dimension of $\underline{S}^{\text{LR}}$ is $N_o = N_p + N_x$. The physical long-range S-matrix $\underline{S}^{\text{LR,phys}}$ having dimension N_p can be found in terms of the partitions of the raw S-matrix, Eq. (4.23):

$$\underline{S}^{\text{LR,phys}} = \underline{S}^{\text{LR}}_{pp} + \underline{S}^{\text{LR}}_{px}\left(\underline{1} - \underline{S}^{\text{LR}}_{xx}\right)^{-1}\underline{S}^{\text{LR}}_{xp}. \tag{4.23}$$

The advantage of using this smaller S-matrix $\underline{S}^{\text{LR,phys}}$ is that it shows a weaker dependence on the matching radius r_0 than the raw S-matrix $\underline{S}^{\text{LR}}$. It is important, however, to note that both $\underline{S}^{\text{LR,phys}}$ and $\underline{S}^{\text{LR}}$ give identical photoabsorption cross sections when used in Eq. (3.28). In addition, while both these S-matrices depend weakly on r_0, the total photoabsorption cross section is found to be independent of r_0. It is often useful to study the long-range S-matrix directly rather than the total photoabsorption cross section. When this type of analysis is performed, it is more sensible to use $\underline{S}^{\text{LR,phys}}$ which is nearly independent of the radius r_0. In fact, for the remainder of this thesis, I will always use $\underline{S}^{\text{LR,phys}}$ when an accurate quantum S-matrix is needed; the superscript "phys" will subsequently be dropped.

4.1.3 Scaled variable S-matrices

This section has described a method for calculating the long-range S-matrix for the motion of an atomic electron at energy E in a static magnetic field of strength B. In most cases, however, it is more useful to study the physics of such an electron using the scaled variables discussed in the Introduction and Appendix A. In this approach, the cross section and S-matrices are studied at a fixed scaled energy $\epsilon = EB^{-2/3}$ as a function of the scaled magnetic field $w = 2\pi B^{-1/3}$. A simple variable transformation of the numerically calculated $\underline{S}^{\rm LR}(E,B)$ gives the needed scaled variable S-matrix $\underline{S}^{\rm LR}(\epsilon,w)$:

$$\underline{S}^{\rm LR}(\epsilon,w) = \underline{S}^{\rm LR}\left(E\left(\epsilon,w,\right),B\left(\epsilon,w\right)\right), \tag{4.24}$$

$$E(\epsilon,w) = \epsilon\left(\frac{2\pi}{w}\right)^2\left(1-i2\frac{\Delta w}{w}\right), \tag{4.25}$$

$$B(\epsilon,w) = \left(\frac{2\pi}{w}\right)^3. \tag{4.26}$$

This rescaling generates a cross section $\sigma^{\Delta w}(\epsilon,w)$ and S-matrix $\underline{S}^{\rm LR}(\epsilon,w)$ in the w domain that has been preconvolved with a Lorentzian of width Δw. I emphasize that unlike other quantum mechanical methods [75] of calculating the scaled photoabsorption cross section, no recasting of the Schrödinger equation is needed in my approach; the energy and magnetic field of Eqs. (4.25) and (4.26) are simply used in the R-matrix calculations described above.

4.2 Recurrences in the quantum S-matrix

My choice of using scattering matrices to describe the motion of an atomic electron in an external magnetic field is based on two important points. First, the S-matrices $\underline{S}^{\rm LR}$ and $\underline{S}^{\rm core}$ contain all of the important physics of the electron. Second, after they have been calculated, these S-matrices can be used to gain physical insight about the electron's motion. In this chapter, the necessary details for calculating the long-range S-matrix $\underline{S}^{\rm LR}(\epsilon,w)$ have been given for an atom in a static external magnetic field. In this final section, calculations of $\underline{S}^{\rm LR}(w)$ are presented that implement this approach.

The calculations presented here are given in terms of the scaled variables of Appendix A. Thus, the scattering matrix $\underline{S}^{\rm LR}(w)$ has been calculated at a fixed scaled energy ϵ as a function of the "energy"-

like scaled variable w. In the spirit of closed-orbit theory, these accurate quantum S-matrices are then Fourier transformed into the scaled action domain. The information contained in the Fourier transform of the matrix element $S_{ll'}^{\rm LR}(w)$ is best presented in terms of the recurrence strength $R(\tilde{S})$. I define the recurrence strength $R(\tilde{S})$ of some w-domain function $f(w)$ in the interval $[w_1, w_2]$ as the windowed Fourier transform:

$$R(\tilde{S}) = \left| \int_{w_1}^{w_2} f(w) e^{-i\tilde{S}w} e^{-(w-w_0)^2/(2\delta)} dw \right|, \tag{4.27}$$

where $\delta = (w_1 + w_2)/6$ and $w_0 = (w_1 + w_2)/2$. The windowing function $\exp(-(w - w_0)^2/(2\delta))$ is used to eliminate artificial side peaks in the recurrence strength. Note that my definition of $R(\tilde{S})$ involves the absolute value of the Fourier transform rather than absolute value squared as some researchers use. This choice accentuates smaller features in the recurrence strength that are diminished when the result of the Fourier transformation in Eq. (4.27) is squared.

First, calculations of the long-range S-matrix $\underline{S}^{\rm LR}(w)$ at a scaled energy of $\epsilon = -0.7$ are presented. At this scaled energy, the classical dynamics are mostly regular (see Fig A.1, Appendix A). This results in relatively few quantum paths contributing to the long-range S-matrix. By plotting the elements of $\underline{S}^{\rm LR}$ in both the w domain (Fig. 4.3) and in the Fourier domain (Fig. 4.4) the most important quantum mechanical paths of the electron can be "seen." First, Fig. 4.3 shows the real part of the matrix element $S_{00}^{\rm LR}$(w) as a function of the scaled field w. This matrix element shows oscillations with w, indicating that a few features in the scaled action domain are controlling the long-range S-matrix. The calculations presented in Fig. 4.4 confirm the presence of the short action contributions to the S-matrix. Here, the Fourier transforms (recurrence strengths) of the quantities $Re\left(S_{00}^{\rm LR}(w)\right)$, $Re\left(S_{22}^{\rm LR}(w)\right)$ and $Re\left(S_{44}^{\rm LR}(w)\right)$ over the range $w = 100 - 500$ are shown. All of these matrix elements show strong recurrences at the same scaled actions. This shows that the same quantum amplitudes contribute to each element of $\underline{S}^{\rm LR}$ at a given scaled energy. Of course at this point, without borrowing the insights of closed orbit theory, it would difficult to understand exactly to what the recurrences in the matrix $\underline{S}^{\rm LR}$ correspond. The important point of these accurate quantum calculations is that the physics of the long-range S-matrix is controlled by a few features in the scaled action domain. The most that can be said without invoking

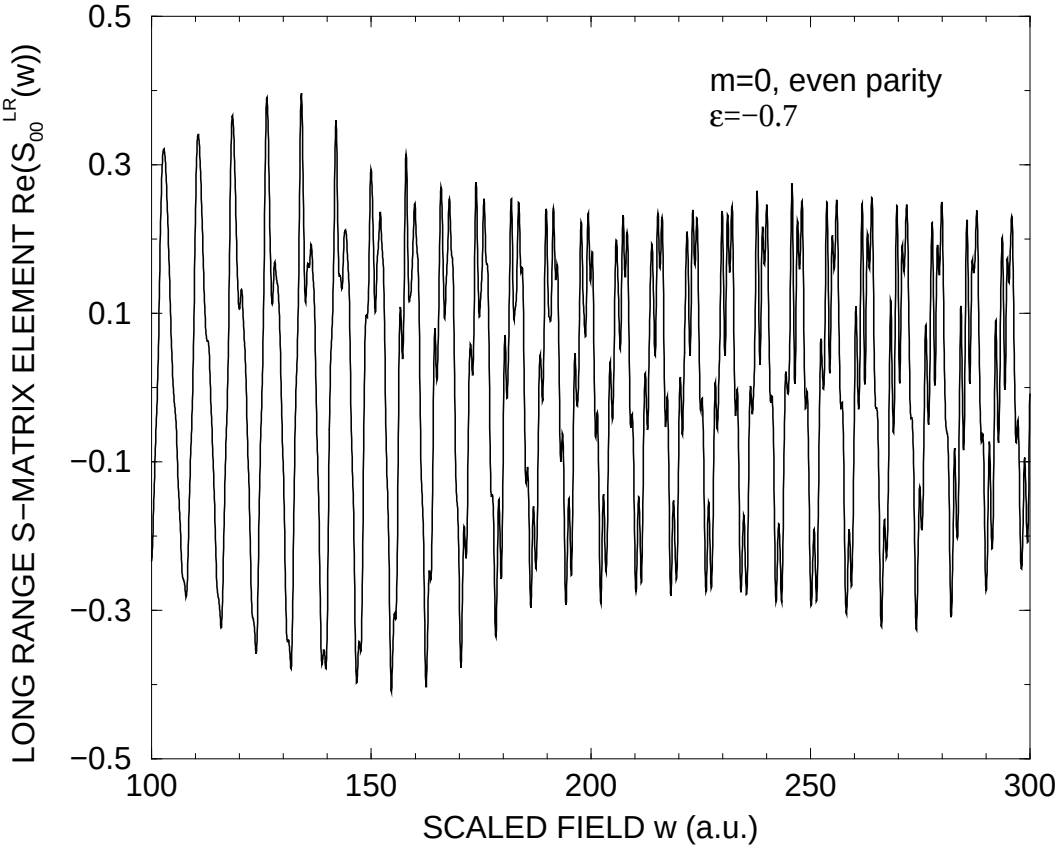

Figure 4.3: The real part of an element of $\underline{S}^{\rm LR}$ is shown as a function of the scaled field w. Here, a low angular momentum piece $Re\left(S^{\rm LR}_{00}(w)\right)$ of the long range S-matrix is plotted at a scaled energy of $\epsilon = -0.7$, where the classical motion is mostly regular. This matrix element, and the others in $\underline{S}^{\rm LR}$, provide a complete description of the electron's motion as it scatters off the long-range Coulomb and diamagnetic potential. This matrix element was calculated using the variational R-matrix method of this chapter, and has been preconvolved with a width $\Delta w = 0.5$ in the w domain. The most important feature of this figure is that the matrix element oscillates with w. High frequency oscillations have been smoothed out with the preconvolution technique, leaving only the largest scale oscillations visible. As a Fourier transform of this matrix element shows (see Fig. 4.4, panel (c)), these oscillations are due to a few quantum mechanical paths of the electron having short scaled actions. The S-matrix shown here is for an $m = 0$, even parity electron.

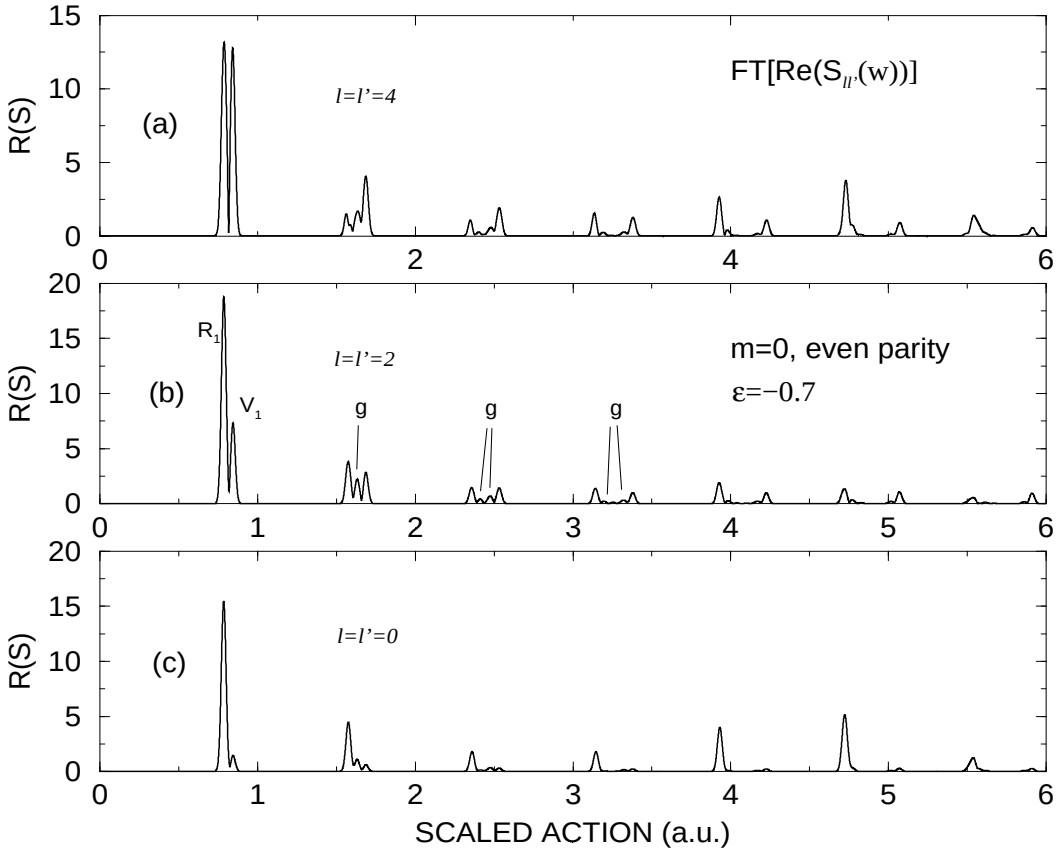

Figure 4.4: The Fourier transforms or recurrence strengths ($R(\tilde{S})$, Eq. (4.27)) of individual elements of the long range S-matrix are shown. As in Fig. 4.3, a scaled energy of $\epsilon = -0.7$ is used here. The recurrence strength of the matrix element plotted in Fig. 4.3 ($Re\left(S_{00}^{\rm LR}(w)\right)$) is shown in the lower panel (c). The middle panel (b) and upper panel (a) give the recurrence strength for higher angular momentum elements ($Re\left(S_{44}^{\rm LR}(w)\right)$ and $Re\left(S_{22}^{\rm LR}(w)\right)$ respectively) of the same long range S-matrix. All three matrix elements exhibit the same sharp peaks in the scaled action domain, with only the amplitudes varying with the angular momentum. The semiclassical methods of the following chapter correlate most of these recurrence peaks with classical closed orbits of the electron. For instance, the shortest action recurrence peak in this graph, labeled R_1, corresponds to the quasi-Landau orbit observed in the first experiments by Garton and Tomkins [27]. The next longest action peak (V_1) is correlated with the electron's motion parallel to the magnetic field. The contributions of harmonics, or repetitions, of these two short action paths are also seen. Because these are recurrence strengths of an accurate quantum S-matrix, some of the recurrence peaks are nonclassical. More specifically, the peaks labeled with the letter "g" - for ghost - have no radially returning classical closed orbits associated with them. Again, the S-matrix shown is for an $m = 0$, even parity electron.

the ideas of closed-orbit theory is this: because the S-matrix elements are quantum mechanical amplitudes for the electron to scatter off the long-range potential, the recurrence peaks in the elements of $\underline{S}^{\mathrm{LR}}$ correspond to different quantum mechanical paths that the electron has taken in its scattering process. The semiclassical approximations of the following chapter (Ch. 5) will link these quantum paths to the chaotic classical closed orbits of the electron.

Itis also interesting to see how the recurrence structures in the long-range S-matrix evolve with the scaled energy ϵ. In the classical motion of the electron, this parameter controls whether the dynamics are regular ($\epsilon < -0.9$) or chaotic ($\epsilon \rightarrow 0$). Figure 4.5 shows the recurrence strength of the quantity $Re\left(S_{44}^{\mathrm{LR}}(w)\right)$ at seven scaled energies ranging from $\epsilon = -0.9 \rightarrow = -0.3$. At the lower scaled energies, the recurrence strength is dominated by two short action quantum paths (labeled R_1 and V_1 after the closed orbits they represent) and their harmonics. As the scaled energy increases, additional recurrence peaks appear. This proliferation of recurrence peaks is one of the manifestations of the underlying classical chaos.

One of the main advantages of having accurate quantum scattering matrices to analyze is that nonclassical paths can be detected and studied. A recurrence peak is nonclassical if there is no classical closed orbit available to explain the recurrence. In the literature, these nonclassical features in the recurrence strength are often called ghost orbits. The most common place to see their presence is just below the scaled energies where new closed orbits bifurcate. Then, the ghost orbits can be viewed as the electron tunneling into an almost allowed classical trajectory. In both Figs. 4.4 and 4.5, I have marked the nonclassical features with the letter “g” - for ghost. Of course, the only way to distinguish between a real orbit and a ghost orbit is to perform a search for classical closed orbits. The results of such a search is given in Appendix B for scaled energies from $\epsilon = -0.4 \rightarrow 0.0$. After the classical search has been completed, any recurrence peaks in the quantum S-matrix $\underline{S}^{\mathrm{LR}}$ having no corresponding closed orbit can be labeled as a ghost orbit.

This chapter has shown that it is possible to calculate and study accurate long-range S-matrices $\underline{S}^{\mathrm{LR}}$ for the motion of an atomic electron in an external magnetic field. While the techniques for calculating this S-matrix are familiar tools of atomic theory, the use of complex energies to accomplish a

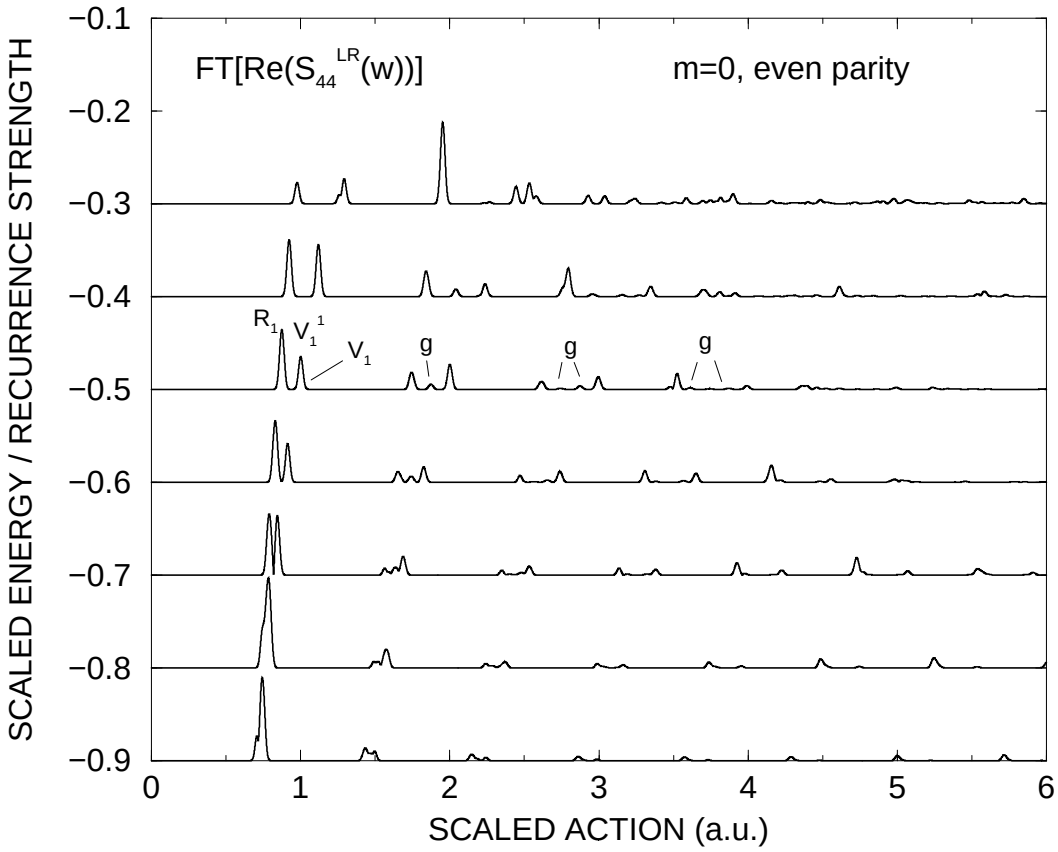

Figure 4.5: Recurrence strengths of the matrix element $Re(S_{44}^{\mathrm{LR}}(w))$ are plotted for multiple scaled energies. This shows how the recurrence peaks (each associated with one quantum path) evolve as the classical dynamics of the electron make a transition from being regular ($\epsilon = -0.9$) to chaotic ($\epsilon = -0.3$). Although the recurrence strength shown here is from an accurate variational R-matrix quantum calculation, the signatures of the underlying classical chaos can be seen in the increased number of recurrence peaks at higher scaled energies. Semiclassical approximations correlate most of the recurrence peaks in this figure with classical closed orbits of the electron. The three shortest action peaks are labeled with the closed orbit to which they correspond. Appendix B gives information about these closed orbits. Nonclassical recurrence peaks that are not related to any closed orbit are marked with the letter "g" - for ghost. The numbers on the vertical axis give the values of the scaled energy for each scan. The recurrence strengths have been scaled to allow multiple scaled energies to be shown on the same graph.

preconvolution of the S-matrix is novel. In addition, using scaled variables along with ideas from closed-orbit theory, the recurrences in the long-range S-matrix can be studied. This analysis allows the detection of nonclassical, or ghost, orbits that contribute to the long range physics. In Ch. 6, it will be seen that these ghost orbits play a critical role in the semiclassical photoabsorption cross section. I emphasize that in previous quantum calculations, only the recurrences of total photoabsorption cross section have been studied. My formula for the photoabsorption cross section shows that the cross section is complicated by multiple scatterings of the electron off the long-range and core regions. Being able to directly study the long-range S-matrix allows recurrences to be studied without the complications of the multiple scattering event that make up the cross section. The full interpretation of the recurrences, however, relies on the introduction of semiclassical approximations to the long-range S-matrix. The next chapter develops such approximations again, for an atomic electron in an external magnetic field.

Chapter 5

Semiclassical S-matrices

So far, this thesis has studied the quantum mechanics of Rydberg atoms in a time-independent external electromagnetic field. The preceding chapters have derived a fully quantum mechanical framework for calculating and interpreting the photoabsorption cross section of such an atom. The main tools in this framework are the scattering matrices $\underline{S}^{\mathrm{LR}}$ and $\underline{S}^{\mathrm{core}}$, which describe the electron's motion in the long-range and core regions respectively. In the previous chapter, a method was described for calculating the long-range S-matrix for the case of an external magnetic field. These large scale quantum calculations yield an accurate S-matrix $\underline{S}^{\mathrm{LR}}(w)$ that can be studied using ideas from scaled variable recurrence spectroscopy. The Fourier transforms of the matrix elements $S^{\mathrm{LR}}_{ll'}(w)$ show sharp peaks in the scaled action domain, suggesting that certain quantum mechanical paths dominate the motion of the electron as it scatters off the long range potential.

As closed-orbit theory has shown [38, 37], the full interpretation of these quantum paths seen in the Fourier transform of $\underline{S}^{\mathrm{LR}}(w)$ emerges when semiclassical approximations are made in the long-range region. In this chapter I develop such an approximation for the long-range S-matrix. The main result, Eq (5.39), is a semiclassical formula for $\underline{S}^{\mathrm{LR}}$ that describes the motion of an atomic electron in an external magnetic field. My formula shows that, in the semiclassical limit, $\underline{S}^{\mathrm{LR}}$ can be constructed using the properties of the closed classical orbits of the electron. These closed orbits, which also appear in closed-orbit theory, are classical trajectories that are launched radially outward from a sphere in the matching region, scatter off the long range Coulomb and diamagnetic potentials and then return radially to the sphere.

Semiclassical scattering matrices have been used in other contexts previously. The idea of a semiclassical S-matrix originated with the work of Miller and coworkers in the 1970's [122]. In his approach, the S-matrix is written in terms of matrix elements of an energy-dependent Green's function. This theory has been used to treat a number of problems in molecular scattering theory [122]. These semiclassical ideas have been extended to atomic scattering problems, such as electron-hydrogen impact ionization [123], by Rost [124]. In a different field of physics, the ballistic conduction of electrons through quantum billiards has been studied using a semiclassical scattering matrix [125, 126, 127, 128, 129] alongside the Landauer formula [130] for the conductance. These diverse works share one thing in common: the semiclassical S-matrix is written in terms of a semiclassical Green's function.

My derivation of the semiclassical approximation to $\underline{S}^{\mathrm{LR}}$ follows this same route. First, the long-range S-matrix is written in terms of matrix elements of an energy dependent Green's function (Sec. 5.1). Then, after the semiclassical Green's function of Gutzwiller [22] has been introduced, the required matrix elements are calculated using the method of stationary phase (Sec. 5.2). This final step is both the most difficult and interesting one in the derivation. It is difficult because there are a number of assumptions needed to use the stationary phase technique - or at least the simple version of it - successfully. When these assumptions break down, the stationary phase integrals must be revisited with additional care. This is the case for the classical trajectory parallel to the magnetic field, for high angular momentum elements of $\underline{S}^{\mathrm{LR}}$, and for bifurcations of closed orbits. In all of these cases, the general approach of using a semiclassical Green's function to extract the semiclassical S-matrix still applies. However, the naive stationary phase approximation for calculating the matrix elements of the Green's function must be modified. These special cases are treated in Sec. 5.3 and show the generality of the semiclassical approximation - when handled with care.

In spite of being subtle and difficult, the stationary phase integrals provide interesting information about the long-range S-matrix. Initially, the S-matrix is written as a sum over infinitely many classical trajectories that scatter off the long-range Coulomb and diamagnetic potentials. These infinitely many trajectories both leave and return to a sphere in the matching region with arbitrary values of the classical angular momentum p_θ. The stationary phase integration essentially encodes the information about **all** of

these trajectories into a smaller subset of trajectories: the closed orbits that leave and return to the sphere with zero classical angular momentum ($p_\theta = 0$). Thus, the stationary phase integrals place the closed orbits in a proper perspective. The closed orbits are **not** the only important trajectories for the long range S-matrix. Rather, the closed orbits are the orbits chosen to **represent** all others. This represents an important advance, as the closed orbits emerge rather mysteriously in standard closed-orbit theory.

It should be mentioned that, while closed-orbit theory contains the same closed orbits that will appear in the semiclassical S-matrix, a direct comparison with closed-orbit theory is difficult at this point. This is because closed-orbit theory only gives the photoabsorption cross section, whereas this chapter focuses on the the long-range S-matrix, which is not present in closed-orbit theory. Of course, the scattering matrices of this chapter can be used, along with the formula for the photoabsorption cross section to calculate the photoabsorption rate. This will be the topic of Ch. 6. Thus, I delay comparisons between my method and closed-orbit theory until then.

5.1 The S-matrix and the Green's function: an exact relationship

The first step in deriving the semiclassical approximation to $\underline{S}^{\mathrm{LR}}$ is to relate this S-matrix to the energy dependent Green's function for the system [122]. In this section, I derive such a relationship between $\underline{S}^{\mathrm{LR}}$ and a Green's function obeying certain boundary conditions at a sphere ($r = r_0$) in the matching region. To allow for the subsequent use of semiclassical approximations, the boundary conditions on the sphere will be chosen to coincide with those of the semiclassical Green's function.

The desired relationship between the Green's function and $\underline{S}^{\mathrm{LR}}$ can be derived by constructing the Green's function out of solutions of the homogeneous Schrödinger equation. This approach follows that of Ch. 3, where the outgoing-wave Green's function needed for the photoabsorption cross section was constructed. Because the techniques of Ch. 3 are used with little modification, the current derivation is presented in outline form only; more details of the method can be found in Ch. 3. The only difference in the current derivation is the boundary conditions imposed on the Green's function. For calculating $\underline{S}^{\mathrm{LR}}$ it is appropriate to impose traveling wave boundary conditions on the Green's function at a sphere

in the matching region ($r = r_0$) that are consistent with the long-range S-matrix state of Ch. 2:

$$\underline{M}^{\mathrm{LR}}(r) = \frac{1}{i\sqrt{2}} \left[\underline{f}^{-}(r) \underline{S}^{\mathrm{LR}} - \underline{f}^{+}(r) \right]. \tag{5.1}$$

The multichannel S-matrix state, Eq. (5.1), can be incorporated into the Green's function once a channel expansion of the Green's function has been introduced:

$$G(\vec{x}, \vec{x}'; E) = \frac{1}{rr'} \sum_{i,j} \Phi_i(\Omega) \tilde{G}_{ij}(\vec{x}, \vec{x}'; E) \Phi_j^*(\Omega'), \tag{5.2}$$

$$\tilde{G}_{ij}(r, r'; E) = rr' \left\langle \Phi_i \left| G(\vec{x}, \vec{x}'; E) \right| \Phi_j \right\rangle. \tag{5.3}$$

As in Ch. 3, the multichannel Green's function $\underline{\tilde{G}}(r, r'; E)$ obeys the inhomogeneous differential equation, Eq. (3.13), is continuous at $r = r'$, and has a discontinuity in its first derivative at $r = r'$ given by Eq. (3.17). The ansatz for the multichannel Green's function with the desired boundary conditions is given in terms of the long-range S-matrix state, Eq. (5.1):

$$\begin{aligned} \underline{\tilde{G}}(r, r') &= \left[\underline{f}^{-}(r) \underline{S}^{\mathrm{LR}} - \underline{f}^{+}(r) \right] \underline{A}(r') \qquad r > r', \\ &= \left[-\underline{f}^{-}(r) \underline{S}^{\mathrm{LR}} \right] \underline{B}(r') \qquad r < r'. \end{aligned} \tag{5.4}$$

The conditions on the Green's function at $r = r'$ give equations for the matrices $\underline{A}(r')$ and $\underline{B}(r')$,

$$\left(\underline{f}^{-} \underline{S}^{\mathrm{LR}} - \underline{f}^{+} \right) \underline{A} + \underline{f}^{-} \underline{S}^{\mathrm{LR}} \underline{B} = 0, \tag{5.5}$$

$$\left(\underline{f}^{-\prime} \underline{S}^{\mathrm{LR}} - \underline{f}^{+\prime} \right) \underline{A} + \underline{f}^{-\prime} \underline{S}^{\mathrm{LR}} \underline{B} = 2, \tag{5.6}$$

which can be readily solved:

$$\underline{A}(r') = i\pi \underline{f}^{-}(r'), \tag{5.7}$$

$$\underline{B}(r') = -i\pi \left[\underline{f}^{-}(r') - \underline{S}^{\mathrm{LR}\dagger} \underline{f}^{+}(r') \right]. \tag{5.8}$$

Because the S-matrix $\underline{S}^{\mathrm{LR}}$ describes electron flux being launched outward from a sphere in the matching region, the source radius r' will be fixed to the matching radius r_0 and the observation radius r will be in the long range region so that $r > r'$. The relevant Green's function is obtained from Eqs. (5.4) and (5.7) and reads:

$$\underline{\tilde{G}}(r, r_0) = i\pi \left[\underline{f}^{-}(r) \underline{S}^{\mathrm{LR}} - \underline{f}^{+}(r) \right] \underline{f}^{-}(r_0). \tag{5.9}$$

Note that this form of the Green's function (5.9) is only valid in the matching region where the S-matrix state, Eq. (5.1), can be used.

The desired expression for the long-range S-matrix can be obtained by inverting Eq. (5.9) to find $\underline{S}^{\mathrm{LR}}$ in terms of the multichannel Green's function, Eq. (5.3). Two issues must be addressed before this step can be performed. First, the observation radius r must also be taken to the matching radius r_0, where the returning scattered wave will be observed (through the S-matrix elements). Second, the boundary conditions on the Green's function must be handled carefully. An inspection of Eq. (5.9) shows that the Green's function satisfies both incoming wave $(-\underline{f}^{+}(r))$ and outgoing wave $(\underline{f}^{-}(r)\underline{S}^{\mathrm{LR}})$ boundary conditions in the observation coordinate r. The incoming wave term in Eq. (5.9) corresponds to electron flux traveling an infinitesimal distance from r_0 to r (recall that the limit $r \to r_0$ is also being taken) without scattering off the long-range region. The outgoing wave term in Eq. (5.9) corresponds to electron flux that travels outward into the long-range region where it then evolves in the long-range Coulomb and diamagnetic potential before being scattered back to the observation radius $r \approx r_0$. Clearly, because the long-range S-matrix describes this scattering process, $\underline{S}^{\mathrm{LR}}$ is related to the Green's function having **outgoing wave** boundary conditions on the sphere in the matching region. With this in mind, the outgoing wave part of Eq. (5.9) can be inverted to give an exact expression for the S-matrix, which is manifestly symmetric:

$$\underline{S}^{\mathrm{LR}} = \frac{r_0^2}{i\pi} \left[\underline{f}^{-}(r_0)\right]^{-1} \underline{G}(r_0, r_0) \left[\underline{f}^{-}(r_0)\right]^{-1}. \tag{5.10}$$

It is critical to remember that the multichannel Green's-function matrix $\underline{G}(r_0, r_0) = \underline{\tilde{G}}(r_0, r_0)/r_0^2$ in this equation obeys outgoing wave boundary conditions on the sphere at r_0. Equation (5.10) is an exact, general relationship valid for any atom and any configuration of external fields; all of the nontrivial physics is now encapsulated in the multichannel Green's function. In the absence of external fields, analytical expressions for this Green's function exist, and yield the expected long-range S-matrix $e^{2i\underline{\beta}}$ for the motion of an electron in a pure Coulomb potential.

One of the main advantages of the S-matrix formulation of the physics of the photoabsorption process now begins to emerge. The incoming wave boundary conditions of the Green's function in

Eq. (5.10) are precisely those obeyed by the semiclassical Green's function of van Vleck and Gutzwiller. Thus, the semiclassical Green's function can be used directly in Eq. (5.10) without modification, leading to an elegant method of deriving the semiclassical $\underline{S}^{\rm LR}$. According to Eq. 5.10 the position space Green's function only needs to be projected onto the channel functions to find the S-matrix. The following section (Sec. 5.2) gives the semiclassical expression for the Green's function $G(\vec{x},\vec{x}';E)$ and shows that this projection step can be carried out using stationary phase integration to obtain the multichannel Green's function $\underline{G}(r_0,r_0)$ needed in Eq. (5.10).

5.2 Surface projections of the Green's function by the method of stationary phase

To derive the semiclassical $\underline{S}^{\rm LR}$, the only remaining task is to introduce the semiclassical Green's function and project it onto the channel functions at a sphere in the matching region. If the required projection integrals are done numerically, this final step is fairly mundane, although very difficult. However, when the projection integrals are done, as in this section, by the method of stationary phase, this final step yields significant physical insight. The stationary phase treatment described below shows how certain classical orbits are selected over all others to encapsulate the contributions to the long-range S-matrix. In most cases, the significant orbits are the closed-orbits, which are launched from and return to the nucleus radially. I will call these classical orbits **radial trajectories** (also closed orbits). However, other nonradially launched orbits also contribute to the S-matrix. In some cases, such as near bifurcations or for high angular momenta element of the S-matrix, these nonradially launched orbits dominate over the radial ones.

A major advantage of the semiclassical S-matrix approach described in this chapter is that it enables a systematic exploration of the nonradial trajectories. In standard closed-orbit theory the emergence of the radial trajectories is somewhat obscured by the complicated formulas of the theory. Furthermore, this has made it difficult for researchers to extend closed-orbit theory to more accurately take the nonradial trajectories into account. The current section develops the basic tools used in performing the stationary phase integrals. The most elementary case is treated here: when the nonradial orbit do not

need to be **explicitly** included in the semiclassical S-matrix. However, the effects of the nonradial trajectories will be taken into account approximately when the Green's function is projected onto the channel functions. The more difficult cases, where the primitive stationary phase integrations fail, are presented in the following section.

While Eq. (5.10) is a general result, it is again useful to specialize to the case of a single channel atom in an external magnetic field along the z-axis. Then, the channel functions are simply the spherical harmonics, so that the projection integral needed to obtain $\underline{G}(r_0, r_0)$ is:

$$G_{lm,l'm'}(E) = \int d\theta d\theta' d\phi d\phi' \sin\theta \sin\theta' Y^*_{lm}(\theta,\phi) G(\vec{x},\vec{x}';E) Y_{l'm'}(\theta',\phi'). \tag{5.11}$$

Because both the source and observation radii r and r' are fixed to the matching radius r_0, the explicit radial dependence of the Green's function is omitted in the following pages. A more convenient form of the projection integral, Eq. (5.11), is obtained by separating the integrals over θ and θ',

$$G_{lm,l'm'}(E) = \int d\theta d\theta' \sin\theta \sin\theta' Y^*_{lm}(\theta,\phi) G_{m,m'}(\theta,\theta';E) Y_{l'm'}(\theta',\phi'), \tag{5.12}$$

from the integrals over ϕ and ϕ',

$$G_{m,m'}(\theta,\theta';E) = \int d\phi d\phi' e^{-im\phi} G(\theta,\phi,\theta',\phi';E) e^{im'\phi'}. \tag{5.13}$$

Now the issue of symmetry must be addressed. The general approach in this section will be to perform the integrals of Eqs. (5.12) and (5.13) using the method of stationary phase. The success of this method depends critically on the existence of well-isolated stationary phase points in the angles $(\theta,\phi,\theta',\phi')$. If continuous families of stationary phase points exist, the stationary phase approximation will fail. This occurs when there is a continuous symmetry that leaves the long-range Hamiltonian invariant. For the case of an atomic electron in an external magnetic field, there is one such continuous symmetry: rotation about the z-axis, which is often called azimuthal symmetry. This symmetry results in the Green's function being diagonal in the corresponding quantum number m. Because the stationary phase technique for the (ϕ,ϕ') integrals (5.13) fails for this case, these integrals must be done exactly. Note that when there are no symmetries in the Hamiltonian, as in the case of a Rydberg electron in crossed electric and magnetic fields, this complication is not present and all of the projection integrals in

Eqs. (5.12) and (5.13) can be done using the stationary phase approach. Given the recent experiments on hydrogen in perpendicular magnetic and electric fields, this would be an interesting case to investigate but it is not pursued here.

When the azimuthal symmetry is present, the integrals over (ϕ, ϕ') can be done analytically by using separation of variables on the full three dimensional Green's function $G(\vec{x}, \vec{x}'; E)$. Alternative, semiclassical approaches for handling continuous symmetries in the Green's function and in trace formulas have been given by Magner *et al.* [131] and by Creagh and Littlejohn [132, 133] respectively. Because these semiclassical methods are needlessly complicated and often subtle, I follow Delos and coworkers [38] and Bogomolny [36] in using separation of variables. The axial symmetry of a Rydberg electron in an external magnetic field is handled easily with the following ansatz for the Green's function in cylindrical coordinates (ρ, z, ϕ):

$$G(\vec{x}, \vec{x}') = \frac{1}{2\pi\sqrt{\rho\rho'}} \sum_m e^{im(\phi-\phi')} G_m(\rho, z, \rho', z'), \tag{5.14}$$

Then, the integrals over (ϕ, ϕ') in Eq. (5.13) can be done analytically:

$$G_{m,m'}(\theta, \theta') = \delta_{mm'} \frac{2\pi}{\sqrt{\rho\rho'}} G_m(\rho, z, \rho', z'). \tag{5.15}$$

As expected, the symmetry reduced Green's function, Eqs. (5.13) and (5.15), is diagonal in the azimuthal quantum number m. The factor $1/\sqrt{\rho\rho'}$ is used in Eq. (5.14) to eliminate the first derivatives $(\partial/\partial\rho)$ in the inhomogeneous equation for $G_m(\rho, z, \rho', z')$, which reads:

$$\left(\frac{1}{2}\frac{\partial^2}{\partial\rho^2} + \frac{1}{2}\frac{\partial^2}{\partial z^2} - \frac{m^2 - 1/4}{2\rho^2} + E - V(\rho, z) \right) G_m(\rho, z, \rho', z') = \delta(\rho - \rho')\,\delta(z - z'). \tag{5.16}$$

Finally, semiclassical approximations for the remaining nonintegrable motion in the Cartesian-like coordinates $(\rho\, z)$ can be made. The two-dimensional semiclassical Green's function of Guztwiller [18, 19, 20, 21] applies directly to Eq. (5.16):

$$G_m(\rho, z, \rho', z'; E) \approx \sum_{\text{class.traj.}} \frac{2\pi}{(2\pi i)^{3/2}} \sqrt{\left| \det \frac{\partial(p'_\rho, p'_z, t)}{\partial(\rho, z, E)} \right|} \exp\left(iS(\rho, z, \rho', z') - i\frac{\mu\pi}{2} \right). \tag{5.17}$$

Here, the sum includes all two-dimensional classical trajectories that propagate from (ρ', z') to (ρ, z) under the dynamics of the Langer-corrected [83] classical Hamiltonian $H = p_\rho^2/2 + p_z^2/2 + m^2/2\rho^2 +$

$V(\rho, z)$. The classical action associated with a particular trajectory is given as the integral,

$$S(\rho, z, \rho', z') = \int_{(\rho', z')}^{(\rho, z)} \left(p''_\rho d\rho'' + p''_z dz'' \right). \tag{5.18}$$

The Maslov index μ [24] is related to the topology of each orbit and is given by the number of sign changes in the determinant in Eq. (5.17) along each orbit. Furthermore, this determinant in Eq. (5.17) provides a measure of the stability of each orbit. More details about this determinant can be found in Appendix C.

When the semiclassical Green's function, Eq. (5.17) is inserted into Eq. (5.15), a semiclassical approximation to the symmetry-reduced Green's function is obtained:

$$G_{mm'}(\theta, \theta') = \delta_{mm'} \sqrt{2\pi} \sum_{\text{traj}} \frac{1}{r_0^2 \left| \dot{r} \right|} \frac{1}{\sqrt{\sin\theta \sin\theta'}} \sqrt{|A_1|} \exp\left(iS(\theta, \theta') - i\frac{\mu\pi}{2} - i\frac{3\pi}{4} \right), \tag{5.19}$$

where the classical stability A_1 is the partial derivative:

$$A_1 = \left. \frac{\partial p'_\theta}{\partial \theta} \right|_{\theta'}. \tag{5.20}$$

According to Eq. (5.12), projecting the polar angle dependence (θ, θ') of this Green's function, Eq. (5.19), onto the spherical harmonics $(Y^*_{lm}(\theta, 0), Y_{l'm'}(\theta', 0))$ gives the multichannel Green's function matrix $G_{lm,l'm'}(E)$ (5.12) needed for the long-range S-matrix (5.10). In the following subsections, these projection integrals are done using the method of stationary phase. For this part of the derivation it is convenient to combine Eqs. (5.19) and (5.12) and write the result in the form:

$$G_{lm,l'm'}(E) = \sum_{\text{traj}} \int d\theta d\theta' \Lambda_{ll'}(\theta, \theta') \sqrt{|A_1(\theta, \theta')|} e^{i\left(S(\theta,\theta') - \mu(\pi/2)\right)}, \tag{5.21}$$

$$\Lambda_{ll'}(\theta, \theta') = \frac{\sqrt{2\pi \sin\theta \sin\theta'}}{r_0^2 \left| \dot{r} \right|} e^{-i(3\pi/4)} Y^*_{lm}(\theta, 0), Y_{l'm'}(\theta', 0). \tag{5.22}$$

This shows that the multichannel Green's function needed for the long-range S-matrix (5.10), can be constructed by considering all of the classical trajectories that are fired outward from the point (r_0, θ'), scatter off the long-range Coulomb and magnetic fields, and then return to the point (r_0, θ) with a classical action $S(\theta, \theta')$. The contributions of these trajectories are integrated over the surface of the sphere $r = r_0$ with the phase $e^{iS(\theta,\theta')}$ and the angular factor $\Lambda_{ll'}(\theta, \theta')$ to determine the Green's function. At

this point, these classical trajectories are not only the radially launched and returning closed-orbits. In Eq. (5.21), all classical orbits at energy E, even those launched nonradially from the matching sphere, must be included to calculate the semiclassical Green's function and thus the S-matrix $\underline{S}^{\mathrm{LR}}$.

Equations (5.21) and (5.22) for the semiclassical Green's function $\underline{G}(r_0, r_0; E)$ and Eq. (5.10) for the long-range S-matrix $\underline{S}^{\mathrm{LR}}$ represent a halfway point in the derivation for the semiclassical formula for $\underline{S}^{\mathrm{LR}}$. It is interesting to note, that in their current form, these formulas show no artificial divergences at the points where new classical orbits bifurcate. Thus, they provide a useful starting point in treating various scenarios found in the physics of a Rydberg electron in an external magnetic field. In the remainder of this section, the elementary case of well-isolated classical orbits and low angular momenta (l, l') is studied.

5.2.1 Initial angle projection

The method of stationary phase integration is one of the most useful tools in semiclassical physics. This was first seen in Gutzwiller's derivation of the trace formula for the density of states [20]. In his work, the periodic orbits emerge as the stationary phase points of an integrand when the trace of the semiclassical Green's function, Eq. (5.17), is taken using the stationary phase technique. A similar idea will be seen in the projection of the semiclassical Green's function onto the spherical harmonics (5.21). Here, as in the trace formula, the dominant classical orbits - the closed orbits - appear when integrals of the semiclassical Green's function (the projection integrals) are evaluated using the method of stationary phase.

I now assume that the classical orbits contributing to the Green's function, Eq. (5.21), are well isolated. Then the classical action $S(\theta, \theta')$ can be expanded in a Taylor series about the stationary phase points in the initial angle $\theta' = \theta_i$:

$$S(\theta, \theta') = S(\theta, \theta_i) + (\theta' - \theta_i) \frac{\partial S}{\partial \theta'} + \frac{1}{2} (\theta' - \theta_i)^2 \frac{\partial^2 S}{\partial \theta'^2}, \tag{5.23}$$

where the stationary phase points θ_i are defined by the vanishing of the linear term in this expansion:

$$\frac{\partial S}{\partial \theta'} = -p'_\theta(\theta_i) = 0. \tag{5.24}$$

Immediately, it is seen that the stationary phase points correspond to classical trajectories that are launched radially ($p_{\theta'} = 0$) outward from r_0. When a strong external magnetic field is applied to an atom, even a one-electron atom, the classical dynamics becomes chaotic, and there are infinitely many of these stationary phase points. In the end, each stationary phase point will contribute a term to the Green's function (5.21) and to the long-range S-matrix (5.10).

This analysis of the stationary phase points is valid when the other angular factors ($\Lambda_{ll'}(\theta,\theta')$ and $A_1(\theta,\theta')$) in the integrand of Eq. (5.21) vary slowly compared to the classical action $S(\theta,\theta')$. This is true for low angular momentum elements of the Green's function $G_{lm,l'm'}(E)$, where the spherical harmonics in $\Lambda_{ll'}(\theta,\theta')$, Eq. (5.22), oscillate slowly. For high angular momenta, these spherical harmonics oscillate rapidly and their variation must taken into account. The required modifications for higher angular momentum will be developed in the next section (Sec. 5.3). However, for now it is assumed that the spherical harmonics, and consequently the matrix $\Lambda_{ll'}(\theta,\theta')$ vary slowly with the polar angles (θ,θ').

Within the aforementioned approximations, the angular factor $\Lambda_{ll'}(\theta,\theta')$ and the amplitude $A_1(\theta,\theta')$ are evaluated at the stationary phase point $\theta' = \theta_i$ and pulled outside the integral over θ' in the Green's function, Eq. (5.21):

$$G_{lm,l'm'}(E) = \sum_{\text{traj}} \int d\theta \Lambda_{ll'}(\theta,\theta_i)\sqrt{|A_1(\theta,\theta_i)|}e^{i(S(\theta\,\theta_i)-\mu\pi/2)} \times I_1. \tag{5.25}$$

The remaining integral I_1 over the initial angle θ' takes the form:

$$I_1 = \int d\theta' \exp\left(\frac{i}{2}(\theta'-\theta_i)^2\frac{\partial^2 S}{\partial\theta'^2}\right). \tag{5.26}$$

In the stationary phase approach, the limits of this integrand are extended to $\pm\infty$, so that the integral can be done using the formula [24]:

$$\int_{-\infty}^{\infty} dx \exp\left(\frac{i}{2}x^2\alpha\right) = \sqrt{\frac{2\pi i}{\alpha}}. \tag{5.27}$$

As Gutzwiller first showed, sign changes of amplitudes such as $\frac{\partial^2 S}{\partial\theta'^2}$ along each classical trajectory must be taken into account when integrals such as Eq. (5.26) are performed. Labeling the number of sign changes of $\frac{\partial^2 S}{\partial\theta'^2}$ along the classical orbit by the integer ν, and performing the integral I_1 using the general

formula, Eq. (5.27), one obtains:

$$I_1 = \sqrt{2\pi i}\left|\det\frac{\partial^2 S}{\partial\theta'^2}\right|^{-1/2} e^{-i\nu\pi/2}. \tag{5.28}$$

Using this result for I_1 in Eq. (5.25), the channel space Green's function becomes,

$$G_{lm,l'm'}(E) = \sqrt{2\pi i}\sum_{\text{traj}}\int d\theta \Lambda_{ll'}(\theta,\theta_i)\sqrt{|A_2(\theta,\theta_i)|}e^{i(S(\theta,\theta_i)-\mu\pi/2)}, \tag{5.29}$$

where the overall amplitude A_2 is the simple product:

$$A_2 = A_1\left(\frac{\partial^2 S}{\partial\theta'^2}\right)^{-1} = -\left.\frac{\partial p'_\theta}{\partial\theta}\right|_{\theta'}\left.\frac{\partial p'_\theta}{\partial\theta'}\right|_{\theta}^{-1} = \left.\frac{\partial\theta'}{\partial\theta}\right|_{p'_\theta}. \tag{5.30}$$

The careful reader will notice that the index ν, which counts the number of sign changes in the amplitude $\frac{\partial^2 S}{\partial\theta'^2}$ along the classical orbit, has disappeared from the Green's function, Eq. (5.29); only the Maslov index μ appears. As a convention, I will always absorb phases such as ν that are generated in stationary phase integrals into the Maslov index μ for the Green's function. With this convention, the index μ of the Green's function is contextual: it always counts the composite number of sign changes of the amplitude whose square root currently appears in the Green's function. For example, when the classical amplitude of the Green's function is $\sqrt{|A_1|}$ the index μ counts the sign changes of A_1.

In this subsection, I have given the details of how the initial angle dependence of the Green's function can be projected out using the method of stationary phase integration. Because this approach will be used repeatedly in this thesis, the discussion has been lengthy. The resulting Green's function, Eq. (5.29), is written as a sum over classical trajectories that are launched radially ($p'_\theta = 0$) from a sphere $r = r_0$ in the matching region, but return to the sphere at a final polar angle θ with any value of the classical angular momentum p_θ. However, Eq. (5.29) specifies that this final angle dependence should also be projected onto the spherical harmonic $Y_{lm}(\theta, 0)$ (contained in the factor $\Lambda_{ll'}$).

5.2.2 Final angle projection

The final angle projection integral required by Eq. (5.29) for the Green's function $G_{lm,l'm'}(E)$ is performed using the same stationary phase approach described above. First, the classical action $S(\theta, p'_\theta)$

is expanded about the stationary phase point in the final polar angle $\theta = \theta_f$:

$$S(\theta, p'_\theta) = S(\theta_f, p'_\theta) + (\theta - \theta_f)\left.\frac{\partial S}{\partial \theta}\right|_{p'_\theta} + \frac{1}{2}(\theta - \theta_f)^2\left.\frac{\partial^2 S}{\partial \theta^2}\right|_{p'_\theta}. \tag{5.31}$$

It is critical to note that the classical action is now a function of the initial angular momentum p'_θ rather than the initial polar angle θ' at the stationary phase points. This switch from θ' to p'_θ in the classical action is necessary as the initial angle dependence θ' has been projected out of the Green's function, Eq. (5.29), and thus the classical action, already. However, as before, the stationary phase points of the action, Eq. (5.31), are the classical trajectories that travel radially as they return to $r = r_0$:

$$\left.\frac{\partial S}{\partial \theta}\right|_{p_{\theta'}} = p_\theta(\theta_f) = 0. \tag{5.32}$$

Again, assuming that the angular factors $(\Lambda_{ll'}(\theta, \theta_i)\sqrt{|A_2(\theta, \theta_i)|})$ in Eq. (5.29) vary slowly with the final angle θ, they can be evaluated at the stationary phase points θ_f of the integrand. Using the expansion of the classical action, Eq. (5.31), in the Green's function, Eq. (5.29), gives the result:

$$G_{lm,l'm'}(E) = \sqrt{2\pi i}\sum_{\text{traj}} \Lambda_{ll'}(\theta_f, \theta_i)\sqrt{|A_2(\theta_f, \theta_i)|}e^{i(S(\theta_f,\theta_i) - \mu\pi/2)} \times I_2. \tag{5.33}$$

The integral I_2,

$$I_2 = \int d\theta' \exp\left(\frac{i}{2}(\theta - \theta_f)^2\left.\frac{\partial^2 S}{\partial \theta^2}\right|_{p_{\theta_i}}\right) = \sqrt{2\pi i}\left|\frac{\partial^2 S}{\partial \theta^2}\right|^{-1/2}_{p'_\theta} e^{-i\nu\pi/2}, \tag{5.34}$$

can be done using the formula, Eq. (5.27), as long as the sign changes in the amplitude $\left.\frac{\partial^2 S}{\partial \theta^2}\right|_{p'_\theta}$ are kept track of in the index ν.

The final form of the semiclassical approximation to $G_{lm,l'm'}(E)$ is found by inserting Eq. (5.33) into Eq. (5.34):

$$G_{lm,l'm'}(E) = 2\pi i\sum_{\text{traj}} \Lambda_{ll'}(\theta_f, \theta_i)\sqrt{|A(\theta_f, \theta_i)|}e^{i(S(\theta_f,\theta_i) - \mu\pi/2)}. \tag{5.35}$$

Again, the index ν has been absorbed into the Maslov index μ of the Green's function that now tracks the sign changes of the overall amplitude A (rather than A_1 or A_2):

$$A = A_2\left(\left.\frac{\partial^2 S}{\partial \theta^2}\right|_{p_{\theta_i}}\right)^{-1} = \left.\frac{\partial \theta'}{\partial \theta}\right|_{p_{\theta_i}}\left.\frac{\partial p_\theta}{\partial \theta}\right|^{-1}_{p_{\theta_i}} = \left.\frac{\partial \theta'}{\partial p_\theta}\right|_{p_{\theta_i}}. \tag{5.36}$$

This final amplitude A is a simple one dimensional derivative that can be calculated numerically for each classical trajectory without difficulty. Finally, the semiclassical approximation to $\underline{S}^{\rm LR}$ can be written down, using the semiclassical Green's function matrix derived in this section, Eq. (5.35), and the definition of the angular factor $\Lambda_{ll'}(\theta,\theta')$, Eq. (5.22). The result,

$$S^{\rm LR}_{ll',m} = 2^{3/2}\pi^{1/2}\sum_{\rm c.o.}\frac{1}{|\dot{r}|}\sqrt{|A|\sin\theta_i\sin\theta_f}\frac{Y^*_{lm}(\theta_f,0)Y_{l'm}(\theta_i,0)}{f^-_l(r_0)f^-_{l'}(r_0)}\exp\left(iS(\theta_f,\theta_i)-i\mu\frac{\pi}{2}-i\frac{3\pi}{4}\right), \tag{5.37}$$

is a sum over the closed orbits that are launched radially outward from the point (r_0,θ_i) in the matching region, scatter classically off the long range Coulomb and magnetic field and then return to the point (r_0,θ_f) again traveling radially.

One further approximation gives the semiclassical $\underline{S}^{\rm LR}$ that will be used in subsequent numerical calculations. For highly excited electrons with small matching radii r_0 and low orbital angular momenta it is appropriate to use the asymptotic, zero-energy forms of the Coulomb functions in Eq. (5.37). The required formulas can be found in Ch. 2, Eqs. (2.4) and (2.5), and yield:

$$\frac{1}{|\dot{r}|\,f^-_l(r_0)f^-_{l'}(r_0)} \to -i\pi(-1)^{l+l'}e^{2i\sqrt{8r_0}}, \tag{5.38}$$

in which case the long-range S-matrix reads:

$$\begin{aligned} S^{\rm LR}_{ll',m}(E,B) &= (2\pi)^{3/2}(-1)^{l+l'}\sum_{\rm c.o.}\sqrt{|A|\sin\theta_i\sin\theta_f}Y^*_{lm}(\theta_f,0)Y_{l'm}(\theta_i,0) \\ &\times \exp\left(iS+2\sqrt{8r_0}-i\mu\frac{\pi}{2}+i\frac{3\pi}{4}\right). \end{aligned} \tag{5.39}$$

In this expression, the classical amplitude $A = \frac{\partial\theta'}{\partial p_\theta}\Big|_{p'_\theta}$ is also evaluated at the stationary phase points (θ_f,θ_i). The details of calculating the closed orbits and their properties that are required in this **primitive semiclassical S-matrix** are given in Appendix B.

Of course, all of the closed orbits that are used to construct $\underline{S}^{\rm LR}$ (5.39) depend both on the energy E of the electron, and external magnetic field B applied to the atom. In most cases, it is more useful to transform this S-matrix to the scaled variables (ϵ,w) of Appendix A. Before giving the resulting scaled variable S-matrix, the issue of preconvolution must be addressed. When the semiclassical long-range S-matrix is used in the formula for the preconvolved cross section, Eq. (3.28), it is necessary to calculate

the S-matrix at complex energies $E + i\Gamma/2$. As discussed in Ch. 4 (see Eqs. (4.24-4.26)) when scaled variables are used, this translates into evaluating the long-range S-matrix at a complex value of the scaled field. That is, to preconvolve the cross section $\sigma(w)$ or long-range S-matrix $\underline{S}^{\rm LR}(w)$ with a Lorentzian of width Δw in the w domain, the substitution

$$w \rightarrow w + i\frac{\Delta w}{2} \tag{5.40}$$

must be used in the scattering matrix $\underline{S}^{\rm LR}(w)$. With this in mind, and using the relations $S = w\tilde{S}$, $r_0 = \tilde{r}_0(w/2\pi)^2$, and $p_\theta = \tilde{p}_\theta(2\pi/w)$ in Eq. (5.39), the preconvolved, scaled-variable S-matrix becomes:

$$\begin{aligned} S^{\rm LR}_{ll',m}(w) &= (2\pi)^{3/2}(-1)^{l+l'}\left(\frac{2\pi}{w}\right)^{1/2}\sum_{\rm c.o.}\sqrt{\left|\tilde{A}\right|\sin\theta_i\sin\theta_f}Y^*_{lm}(\theta_f,0)Y_{l'm}(\theta_i,0) \\ &\times \exp\left(iw\tilde{S} - i\mu\frac{\pi}{2} + i\frac{3\pi}{4}\right)\exp\left(-\tilde{S}\frac{\Delta w}{2}\right). \end{aligned} \tag{5.41}$$

Note that the extra phase $2\sqrt{8r_0}$ is simply the classical action from r_0 to the origin and back again. Thus, in the scaled S-matrix (5.41) I have absorbed this phase into the scaled action of each orbit $\tilde{S}$. Because the closed classical orbits are completely independent of the scaled field w, the only effect of the complex value of the scaled field is to introduce a **damping factor** $\exp(-\tilde{S}\Delta w/2)$ into the semiclassical S-matrix. This will have important consequences in the convergence of the semiclassical photoabsorption cross section developed in Ch. 6.

It is important to mention the conditions under which the semiclassical S-matrix, Eq. (5.39) or (5.41), is a good approximation. First, the derivation has assumed that the spherical harmonics vary slowly with the polar angles θ and θ' so that the stationary phase points are simply the radially launched and returning orbits. However, I emphasize that the effects of the nonradial trajectories are included approximately through the classical amplitude A of each orbit. Second, it is required that the stationary phase points (the radial orbits) exist, and are well isolated from each other. Lastly, although I have derived the long range S-matrix for an atom in an external magnetic field, the final result, Eq. (5.39), is also valid for an external electric field as well.

5.3 Special cases and improvements

In most cases, the semiclassical S-matrix derived in the previous section (5.39) provides an accurate description of the physics of an atomic electron in an external magnetic field. However, there are a number of situations in which this primitive semiclassical approximation fails. This section demonstrates how the ideas and tools of the previous section can be modified to treat these cases.

In general, one of the difficulties with semiclassical approximations is that when their primitive forms break down, a considerable amount of effort is required to repair them. This was first seen as researchers incorporated bifurcations [57] and continuous symmetries [133] into the semiclassical trace formula of Gutzwiller. The same has been true in semiclassical studies of atoms in external fields. As an example, since the original development of closed-orbit theory in 1988, only a few researchers [62, 54, 63] have attempted to give uniform semiclassical approximations for bifurcations of the closed orbits. Furthermore, because the standard formulation of closed-orbit theory uses semiclassical wavefunctions rather than Green's functions, many of the advances in the Green's function based trace formulas have not been applicable to closed-orbit theory. Thus, while uniform semiclassical approximations have been given for trace formulas, analogous progress in closed-orbit theory has lagged behind.

The approach of this chapter provides a simple solution to the difficulties found in improving the semiclassical approximations of closed orbit theory. In general, the semiclassical Green's function, Eq. (5.17), used to find the S-matrix is a very robust object. It is mainly when this configuration space Green's function is projected onto the channel functions (spherical harmonics) that difficulties arise. This section explores the long-range S-matrix for three cases where the above primitive version of the stationary phase technique given above fails. These instances are: the orbit parallel to the magnetic field, moderately high angular momentum elements of $\underline{S}^{\mathrm{LR}}$, and bifurcations of the closed orbits. In each case, appropriately modified versions of the stationary phase technique give improved semiclassical S-matrices.

5.3.1 Parallel orbit

The most benign type of failure of Eq. (5.39) is when one of the angular factors in the S-matrix ($\sin\theta$ or $Y_{lm}(\theta,\phi)$) vanishes at the initial (θ_i) or final (θ_f) angle of the closed orbit. Then, the contribution of that orbit to the S-matrix will vanish unphysically. The most striking example of this is the closed orbit that is parallel to the magnetic field ($\theta_i = \theta_f = 0$ or π), for which the factor $\sqrt{\sin\theta\sin\theta'}$ vanishes. A second example is the quasi-Landau orbit ($\theta_i = \theta_f = \pi/2$), which gives a vanishing contribution to the S-matrix for odd parity states of the electron. The vanishing of these two orbits is known to be unphysical since both experiments and theory have seen their signatures in recurrence spectra. In both of these cases, the source of the error is in neglecting the angular dependences of factors such as $\sin\theta$ or $Y_{lm}(\theta,\phi)$ when the stationary phase integrals are done. Thus, the solution is to include, at least approximately, the strongest angular dependences of the Green's function in the stationary phase integrals.

This can be accomplished for the parallel orbit in a straightforward manner, beginning with the multidimensional Green's function, Eqs. (5.21) and (5.22), before the projection integrals over θ and θ' have been performed:

$$G_{lm,l'm'}(E) = \sum_{\text{traj}} \int d\theta d\theta' \Lambda^0_{ll'}(\theta,\theta') \sqrt{|A_1| \sin\theta \sin\theta'}\, e^{i\left(S(\theta,\theta') - \mu\pi/2\right)}, \tag{5.42}$$

$$\Lambda^0_{ll'}(\theta,\theta') = \frac{\sqrt{2\pi}}{r_0^2\,|\dot{r}|} e^{-i(3\pi/4)} Y^*_{lm}(\theta,0), Y_{l'm'}(\theta',0). \tag{5.43}$$

Here, the factor $\sqrt{\sin\theta\sin\theta'}$ has been placed explicitly in the Green's function, Eq. (5.42), rather than in the angular factor $\Lambda^0_{ll'}(\theta,\theta')$, Eq. (5.43), because its angular dependence must be included when the stationary phase integrals are performed. A superscript "0" is used on $\Lambda_{ll'}$ in Eq. (5.43) to distinguish the factor for the parallel orbit $\Lambda^0_{ll'}(\theta,\theta')$ (5.43) from that for the other orbits $\Lambda_{ll'}(\theta,\theta')$, Eq. (5.22). The only difference is that $\Lambda^0_{ll'}(\theta,\theta')$ does not contain the factor $\sqrt{\sin\theta\sin\theta'}$. The following discussion will be presented for the parallel orbit having $\theta_i = \theta_f = 0$. However, the formulas also apply to the parallel orbit having $\theta_i = \theta_f = \pi$.

Because the main contribution of the projection integrals will come from the integrand's value

near $\theta = \theta' = 0$, small angle expansions of $\sin\theta \approx \theta$ and $\sin\theta' \approx \theta'$ can be used in Eq. (5.42):

$$G_{lm,l'm'}(E) \approx \int d\theta d\theta' \Lambda^0_{ll'}(\theta,\theta')\sqrt{|A_1|}\sqrt{\theta\theta'}e^{i\left(S(\theta,\theta')-\mu\pi/2\right)}. \tag{5.44}$$

Again, the remaining angular factor $\Lambda^0_{ll'}(\theta\,\theta')$ is assumed to vary slowly and will be evaluated at the stationary point of the integrand ($\theta = \theta_f, \theta' = \theta_i$). From this point, the treatment of the integrals in Eq. (5.44) using stationary phase integration proceeds exactly as in the previous section. First, the integral over the initial angle θ' is performed by expanding the action about the stationary phase point $\theta' = \theta_i = 0$. Again, the resulting stationary phase point is a classical orbit, the parallel orbit, that is launched radially along the direction of the magnetic field. A similar procedure is used for the final angle projection of Eq. (5.44). Both of these projections require the integral,

$$I_3(\alpha) = \int_0^\infty dx\sqrt{x}e^{\frac{i}{2}x^2\alpha} = \frac{1}{\sqrt{2}}e^{i3\pi/8}\Gamma\left(\frac{3}{4}\right)|\alpha|^{-3/4}, \tag{5.45}$$

where $\Gamma(3/4) = 1.22541\ldots$ is the the Gamma function. When the expansions of the action, Eqs. (5.23) and (5.31) are used along with the integral I_3, Eq. (5.45), to evaluate the integrals in Eq. (5.44), the resulting Green's function becomes,

$$G_{lm,l'm'}(E) \approx \frac{1}{2}\Lambda^0_{ll'}(\theta_i,\theta_f)\Gamma\left(\frac{3}{4}\right)^2 e^{i3\pi/4}\left|\frac{\partial p'_\theta}{\partial\theta'}\right|_\theta^{-3/4}\left|\frac{\partial p_\theta}{\partial\theta}\right|_{p'_\theta}^{-3/4}|A_1|^{1/2}\,e^{i(S-\mu\pi/2)}. \tag{5.46}$$

This formula applies to both orbits that move parallel to the external field ($\theta_i = \theta_f = 0$ and π) along the z-axis. The final form of the Green's function and S-matrix for these orbits is obtained by simplifying the combination of amplitudes in Eq. (5.46). This requires a careful handling of the partial derivatives:

$$\begin{aligned}
\left|\frac{\partial p'_\theta}{\partial\theta'}\right|_\theta^{-3/4}\left|\frac{\partial p_\theta}{\partial\theta}\right|_{p'_\theta}^{-3/4}\left|\frac{\partial p'_\theta}{\partial\theta}\right|_{\theta'}^{1/2} &= \left|\frac{\partial(\theta',\theta)}{\partial(p'_\theta,\theta)}\right|^{3/4}\left|\frac{\partial(\theta,p'_\theta)}{\partial(p'_\theta,p_\theta)}\right|^{3/4}\left|\frac{\partial(p'_\theta,\theta')}{\partial(\theta,\theta')}\right|^{1/2} \\
&= \left|\frac{\partial(\theta,\theta')}{\partial(p'_\theta,p_\theta)}\right|^{3/4}\left|\frac{\partial(p'_\theta,\theta')}{\partial(\theta,\theta')}\right|^{1/2} \\
&= \left|\frac{\partial(\theta,\theta')}{\partial(p'_\theta,p_\theta)}\right|^{1/4}\left|\frac{\partial(p'_\theta,\theta')}{\partial(p'_\theta,p_\theta)}\right|^{1/2} \\
&= \left|\frac{\partial(\theta,\theta')}{\partial(p'_\theta,\theta')}\frac{\partial(p'_\theta,\theta')}{\partial(p'_\theta,p_\theta)}\right|^{1/4}\left|\frac{\partial(p'_\theta,\theta')}{\partial(p'_\theta,p_\theta)}\right|^{1/2} \\
&= \left|\frac{\partial(\theta,\theta')}{\partial(p'_\theta,\theta')}\right|^{1/4}\left|\frac{\partial(p'_\theta,\theta')}{\partial(p'_\theta,p_\theta)}\right|^{3/4} \\
&= \left|\frac{\partial\theta}{\partial p'_\theta}\right|_{\theta'}^{1/4}\left|\frac{\partial\theta'}{\partial p_\theta}\right|_{p'_\theta}^{3/4}.
\end{aligned} \tag{5.47}$$

Furthermore, the first amplitude in this result $\left|\frac{\partial\theta}{\partial p'_\theta}\right|_{\theta'}^{1/4}$ can be approximated as,

$$\begin{aligned}\left|\frac{\partial\theta}{\partial p'_\theta}\right|_{\theta'}^{1/4} &= \left|\frac{\partial p_\theta}{\partial\theta'}\right|_{\theta}^{-1/4} \\ &= \left|\left.\frac{\partial p_\theta}{\partial\theta'}\right|_{p'_\theta} + \left.\frac{\partial\theta'}{\partial\theta}\right|_{p_\theta}\left.\frac{\partial p'_\theta}{\partial\theta'}\right|_{\theta}\right|^{-1/4} \\ &\approx \left|\frac{\partial\theta'}{\partial p_\theta}\right|_{p'_\theta}^{1/4}. \end{aligned} \tag{5.48}$$

Combining Eqs. (5.47) and (5.48) for the amplitude, with Eq. (5.46) gives the final form of the semiclassical Green's function for the parallel orbit,

$$G_{lm,l'm'}(E) \approx \frac{1}{2}\Lambda^0_{ll'}(\theta_i,\theta_f)\Gamma\left(\frac{3}{4}\right)^2 e^{i3\pi/4}\,|A|\,e^{i(S-\mu\pi/2)}. \tag{5.49}$$

The manipulations of the classical amplitudes, Eqs. (5.47) and (5.48), are clearly the most difficult aspects of this derivation. In spite of that, the procedure for finding the semiclassical Green's function $G_{lm,l'm'}(E)$ for the parallel orbits is straightforward: the integrals over θ and θ' are performed using the stationary phase technique, but including the angular dependence of the factor $\sqrt{\sin\theta\sin\theta'} \approx \sqrt{\theta\theta'}$.

The final long-range S-matrix for the parallel orbit is constructed using the Green's function (Eq. (5.49)), the angular factor $\Lambda^0_{ll'}(\theta_i,\theta_f)$ (Eq. (5.43)), and the relationship between $\underline{S}^{\rm LR}$ and $\underline{G}(r_0,r_0)$ (Eq. (5.10)):

$$S^{\rm LR}_{ll'} = \sqrt{\frac{\pi}{2}}\Gamma\left(\frac{3}{4}\right)^2 (-1)^{l+l'} Y^*_{lm}(\theta_f,0)Y_{l'm}(\theta_i,0)\,|A|\,\exp\left(iS(\theta_f,\theta_i) + 2i\sqrt{8r_0} - i\mu\frac{\pi}{2} + i\pi\right). \tag{5.50}$$

The asymptotic, zero-energy Coulomb functions, Eq. (5.38), have been used in deriving this result. To rewrite this result in terms of scaled variables, the scaling relationships of Appendix A can again be used. In subsequent calculations, the scaled variable version of Eq. (5.50) will be used for the contribution of the parallel orbits, alongside Eq. (5.41) for the off-axis orbits. In both cases, the preconvolution of the S-matrix introduces the damping factor $\exp(-\tilde{S}\Delta w/2)$ into the long-range S-matrix.

Note that the orbit parallel to the external field was first treated by Gao and Delos [51] using the semiclassical wavefunctions of closed-orbit theory. The approach given here has a similar form as their result, but exhibits a slightly different semiclassical amplitude A. The success of Eq. (5.50) will be seen

in next chapter (Ch. 6), where it is used to calculate the photoabsorption cross section of an atom in an external magnetic field. Also note that Eq. (5.50) is particularly relevant for an atom in an external electric field, where the dominant features in the recurrence spectrum are given by orbits parallel to the electric field.

5.3.2 High angular momentum

A second difficulty occurs for S-matrix elements $S^{\rm LR}_{ll'}$ having moderate and high values of the angular momenta l and l'. As described above, the stationary phase approximation leading to the S-matrices of Eqs. (5.39) and (5.50) assumes that the spherical harmonics vary slowly with the polar angles (θ, θ'). This approximation breaks down for high angular momentum where the spherical harmonics begin to oscillate rapidly.

For very high angular momenta, **all** of the angular dependence of the spherical harmonics can be included in the projection integrals (5.21). In this case, an improved stationary phase approximation leads to the modified stationary phase conditions $p_\theta = \pm(l + 1/2)$ and $p'_\theta = \pm(l' + 1/2)$. In the limit $l, l' \gg 1$, these modified stationary phase conditions represent a correspondence principle (for $p_\phi = 0$) between the quantum (l, l') and classical (p_θ, p'_θ) angular momentum. This approach is a straightforward generalization of the method of the previous section and includes nonradial trajectories explicitly in the final semiclassical S-matrix. In practice, this type of semiclassical approximation for the S-matrix $\underline{S}^{\rm LR}$ would be prohibitive because different S-matrix elements require a calculation of different classical trajectories. Moreover, it should not be necessary unless one is interested in treating initial electronic states with very high angular quantum numbers. For the low lying initial states of complex atoms, only moderate final state angular momenta are typically relevant. For these cases a simpler approximation is appropriate.

As the semiclassical approximation for the parallel orbit demonstrates, a simple way of improving the projection integrals of the Green's function is to include the lowest order variations of the offending angular factor. For moderate angular momentum S-matrix elements, this translates into expanding the spherical harmonics to linear order about the stationary phase points (θ_i,θ_f). This approach is given here

and shows that the resulting correction to the primitive S-matrix (5.39) involves the derivatives of the spherical harmonics and powers of the classical amplitude A, Eq. (5.36), that appears in the primitive semiclassical approximation to $\underline{S}^{\mathrm{LR}}$. Most importantly, the improved semiclassical S-matrix derived here still involves only radial launched and returning trajectories. Thus, the approximation circumvents the computational complications of searching for nonradial closed orbits.

The expansion of the spherical harmonics to linear order about the stationary phase points reads,

$$Y_{l'm}(\theta',0) \approx Y_{l'm}(\theta_i,0) + (\theta'-\theta_i)\left.\frac{\partial Y_{l'm}(\theta',0)}{\partial\theta'}\right|_{\theta_i} \tag{5.51}$$

$$Y^*_{lm}(\theta,0) \approx Y^*_{lm}(\theta_f,0) + (\theta-\theta_f)\left.\frac{\partial Y^*_{lm}(\theta,0)}{\partial\theta}\right|_{\theta_f}. \tag{5.52}$$

The projection integral of the Green's function, Eqs. (5.21) and (5.22), can now be carried out using the stationary phase approach, but with one modification. Rather than performing the integrals over θ and θ' sequentially as before, both integrals are performed simultaneously. This leads to considerable simplifications and requires a two dimensional expansion of the classical action in the variables (θ,θ') about the stationary phase points ($\theta'=\theta_i$,$\theta=\theta_f$). Defining the vector $\vec{\alpha}$

$$\vec{\alpha} = \begin{pmatrix} \theta'-\theta_i \\ \\ \theta-\theta_f \end{pmatrix}, \tag{5.53}$$

the two-dimensional Taylor series for the action reads,

$$S(\theta,\theta') = S(\theta_f,\theta_i) + \vec{\alpha}^{\mathrm{T}}\frac{\partial S}{\partial\vec{\alpha}} + \frac{1}{2}\vec{\alpha}^{\mathrm{T}}\frac{\partial^2 S}{\partial\vec{\alpha}\partial\vec{\alpha}}\vec{\alpha}, \tag{5.54}$$

where

$$\frac{\partial S}{\partial\vec{\alpha}} = \begin{pmatrix} \frac{\partial S}{\partial\theta'} \\ \\ \frac{\partial S}{\partial\theta} \end{pmatrix} = \begin{pmatrix} -p_{\theta}\prime \\ \\ p_\theta \end{pmatrix}, \tag{5.55}$$

$$\frac{\partial^2 S}{\partial\vec{\alpha}\partial\vec{\alpha}} = \begin{pmatrix} \frac{\partial^2 S}{\partial\theta'\partial\theta'} & \frac{\partial^2 S}{\partial\theta'\partial\theta} \\ \\ \frac{\partial^2 S}{\partial\theta\partial\theta'} & \frac{\partial^2 S}{\partial\theta\partial\theta} \end{pmatrix}. \tag{5.56}$$

As before, the stationary phase condition ($\frac{\partial S}{\partial\vec{\alpha}} = 0$) selects radially traveling trajectories, the closed orbits, at small distances.

Next, the expansions of the action, Eq. (5.54), and of the spherical harmonics, Eqs. (5.51) and (5.52), are used in the yet to be projected Green's function, Eqs. (5.21) and (5.22). The term with the product $Y^*_{lm}(\theta_f,0)Y_{l'm}(\theta_i,0)$ simply gives the result (5.39) of the previous section. The only nonvanishing correction term involves the derivatives of **both** of the spherical harmonics (if the angular dependence of $\sqrt{\sin\theta\sin\theta'}$ is again neglected). After the slowly varying part of the integrand,

$$\sqrt{\sin\theta\sin\theta'}\;\frac{\partial Y^*_{lm}(\theta,0)}{\partial\theta}\bigg|_{\theta_f}\;\frac{\partial Y_{l'm}(\theta',0)}{\partial\theta'}.\bigg|_{\theta_i}, \tag{5.57}$$

has been evaluated at the stationary phase points, the remaining integral can be performed:

$$I_2=\int d\alpha_1 d\alpha_2\alpha_1\alpha_2\,\exp\left(\frac{i}{2}\vec{\alpha}\cdot\frac{\partial^2 S}{\partial\vec{\alpha}\partial\vec{\alpha}}\cdot\vec{\alpha}\right)=-2\pi\left|\det\frac{\partial^2 S}{\partial\vec{\alpha}\partial\vec{\alpha}}\right|^{-1/2}\;\frac{\partial\theta'}{\partial p_\theta}\bigg|_{p'_\theta}\;e^{-i\nu\pi/2}. \tag{5.58}$$

As before the index ν counts the number of sign changes of the matrix $\frac{\partial^2 S}{\partial\vec{\alpha}\partial\vec{\alpha}}$ along each trajectory. Using Eq. (5.58) and manipulating the classical amplitudes using Eq. (5.36), an expression for the corrected semiclassical Green's function (5.21) is found:

$$\begin{aligned} G_{ll',m} &= (2\pi)^{3/2} i\sum_{traj}\frac{1}{r_0^2\,|\dot{r}|}\sqrt{|A|\sin\theta_i\sin\theta_f} \\ &\times \left(Y^*_{lm}(\theta_f,0)Y_{l'm'}(\theta_i,0)+|A|\,e^{i\pi(\mu+1/2)}\frac{\partial Y^*_{lm}(\theta_f,0)}{\partial\theta_f}\frac{\partial Y_{l'm}(\theta_i,0)}{\partial\theta_i}\right) \\ &\times \exp\left(iS-i\mu\frac{\pi}{2}-i\frac{3\pi}{4}\right). \end{aligned} \tag{5.59}$$

The corresponding improved $\underline{S}^{\rm LR}$ from Eqs. (5.10) and (5.59), is then,

$$\begin{aligned} S^{\rm LR}_{ll',m} &= (2\pi)^{3/2}(-1)^{l+l'}\sum_{traj}\sqrt{|A|\sin\theta_i\sin\theta_f} \\ &\times \left(Y^*_{lm}(\theta_f,0)Y_{l'm'}(\theta_i,0)+|A|\,e^{i\pi(\mu+1/2)}\frac{\partial Y^*_{lm}(\theta_f,0)}{\partial\theta_f}\frac{\partial Y_{l'm}(\theta_i,0)}{\partial\theta_i}\right) \\ &\times \exp\left(iS+2i\sqrt{8r_0}-i\sigma\frac{\pi}{2}+i\frac{3\pi}{4}\right). \end{aligned} \tag{5.60}$$

The sum over trajectories in these expressions is the same as in the primitive semiclassical long-range S-matrix: each classical trajectory that is launched radially outward from (r_0,θ_i) and returns radially to (r_0,θ_f) after accumulating a classical action $S(\theta_f,\theta_i)$ contributes a term to the semiclassical S-matrix. In addition, the semiclassical amplitude A (5.36) and Maslov index μ are the same as in the primitive semiclassical S-matrix, Eq. (5.39). Although this improved S-matrix, like traditional closed-orbit theory,

still involves only radial trajectories at r_0, it now includes the first-order corrections for higher angular momenta. In fact, by looking at the ratio

$$\eta = \left| \frac{Y^*_{lm}(\theta_f, 0) Y_{l'm'}(\theta_i, 0)}{A \frac{\partial Y^*_{lm}(\theta_f,0)}{\partial \theta} \frac{\partial Y_{l'm}(\theta_i,0)}{\partial \theta'}} \right| \tag{5.61}$$

for each trajectory, the importance of the correction can be ascertained. Notice that when a trajectory lies near the node of a spherical harmonic, as in the above mentioned quasi-Landau orbit for odd parity states, the "correction" actually dominates the S-matrix. The original version of closed-orbit theory gives a vanishing recurrence strength for the odd parity quasi-Landau resonance. Shaw *et al.* [134] have given a similar correction for the quasi-Landau orbit as Eq. (5.60), but their result is only for the quasi-Landau orbit. The derivation presented here shows that such a correction term is present for all closed orbits when the angular momentum is moderate. However, most cases studied in this thesis have sufficiently low angular momentum that the correction derived here is unimportant except for the odd parity quasi-Landau recurrence.

5.3.3 Bifurcations

So far, corrections of the semiclassical S-matrix have been given for cases where the angle-dependent pieces, such as $\sqrt{\sin\theta \sin\theta'}$ and $Y_{lm}(\theta, \phi)$, become important to include in the stationary phase integrals. The corrections given for the parallel orbit and for moderate angular momenta have made a common assumption: the stationary phase points exist and are well isolated from each other. It has been seen that the stationary phase points correspond to closed classical orbits. These orbits are launched radially outward from a sphere $r = r_0$ in the matching region and return to the sphere radially after scattering classically off the long range fields. This radial trajectory approximation includes the effects of nonradial trajectories approximately through the classical amplitude A (5.36) in the semiclassical S-matrix. However, if a stationary phase point does not exist in the first place, the contributions of nearby nonradial orbits will be unrepresented in the long range S-matrix. This occurs near bifurcations of the closed orbits.

Bifurcations are a common feature of classically nonintegrable systems [109, 12]. For an atom

in a strong magnetic field, bifurcations of the closed orbits occur as the scaled energy ϵ is increased [60]. Figure B.1 of Appendix B shows a map of the closed orbits for diamagnetic hydrogen. When the system is integrable ($\epsilon = -\infty$) there is only one closed orbit, the familiar Kepler orbit in the Coulomb potential. As ϵ increases, new orbits are born up until $\epsilon = 0$ where there are infinitely many closed orbits. Delos and coworkers have used normal form theory [60, 61, 61] to analyze and study sequences of bifurcations of closed orbits in an external magnetic field. However, their analysis is purely classical. Only Main and Wunner [63] have attempted to include bifurcations of closed orbits in a semiclassical theory of photoabsorption. Their treatment uses semiclassical wavefunctions, alongside normal form theory, to construct uniform semiclassical approximations for a few types of bifurcations. It should be mentioned that this discussion applies only to the case of an external magnetic field; the bifurcations of closed orbits in external electric fields have been successfully included in a semiclassical formulation [62].

This final subsection sketches how bifurcations of closed orbits can be treated using the semiclassical approximations of this chapter. Because this work is still in progress, the emphasis will be on the qualitative features of the proposed approach rather than on formal derivations. In the language of this chapter, a bifurcation occurs when a new stationary phase point comes into existence at some scaled energy ϵ_b. Thus, below the bifurcation point, the primitive semiclassical approximation for $\underline{S}^{\mathrm{LR}}$ shows no recurrence peak for the (nonexistent) closed orbit. Also, at the bifurcation point, the primitive semiclassical approximation, Eq. (5.39), diverges to infinity. That is, it shows an infinite recurrence strength. Of course, once the closed orbit has bifurcated, the S-matrices developed above are finite and give a good description of the associated recurrence peak. These predictions of the primitive semiclassical approximation are in disagreement with both experiment and accurate quantum calculations. First, below the classical bifurcation points small recurrence peaks are seen [44]. These prebifurcated orbits, ghost orbits, exist because the electron can tunnel into quantum mechanical paths that do not quite exist classically. Examples of these nonclassical paths were seen in the accurate quantum S-matrices of the previous chapter (Ch. 4). Second, quantum calculations and experiments alike show that the recurrence amplitudes are always finite at the bifurcation points. Thus, the divergence of closed-orbit theory, and the primitive semiclassical S-matrix of this chapter at the bifurcations is artificial.

A successful semiclassical theory of bifurcations, then, will include two features. First, the ghost orbits will be predicted. And second, the semiclassical amplitudes will be uniform (finite) as the scaled energy moves through the bifurcation point. The semiclassical theory of Main and Wunner [63] achieves both of these goals for certain types of bifurcations. However, their approach contains two difficulties. To extract the contributions of the prebifurcated ghost orbits, they analytically continue the classical trajectories into the complex plane. This substantially complicates numerical calculations of the closed orbits. When these complex ghost orbits are included into the semiclassical theory, their recurrence strength is seen to decay exponentially below the bifurcation point. However, an additional contribution below the bifurcation point is predicted that diverges exponentially. Main and Wunner handle this new divergence in the following manner [63]:

> "In the above semiclassical formulas this complex-conjugate ghost would produce an unphysical exponential increase of the amplitude at energies below the bifurcation point. Thus we have as a by-product of the derivation of uniform semiclassical formulas that ghost orbits of this type have no physical meaning. In other words, they must not be included in the standard formulas since they do not appear in the asymptotic expansion of the uniform approximation ..."

In other words, certain predictions of their theory are discarded because they are unphysical. In spite of this, most aspects of Main and Wunner's work appear to be well founded. This discussion shows, however, that the semiclassical theory for bifurcations of closed orbits in an external magnetic field is not completely understood.

I now give an outline of how bifurcations of closed orbits can be included in the semiclassical long-range S-matrix. The treatment begins with the Green's function, Eq. (5.29), after the initial angle projection has been performed:

$$G_{lm,l'm'}(E) = \sqrt{2\pi i}\sum_{\text{traj}}\int d\theta \Lambda_{ll'}(\theta,\theta_i)\sqrt{|A_2(\theta,\theta_i)|}e^{i(S(\theta,\theta_i)-\mu(\pi/2))}. \tag{5.62}$$

In general, the amplitude in this formula, $A_2 = \left.\frac{\partial\theta'}{\partial\theta}\right|_{p'_\theta}$, depends on the initial and final angles. The trajectories that contribute to this Green's function are launched radially from a sphere in the matching region. However, when they return to the sphere, the trajectories have many different values of the classical angular momentum p_θ. Next the main idea for treating bifurcations is presented.

Below a bifurcation point, there is simply no orbit that returns to the sphere radially. However, there are orbits that return to the sphere. As long as the sphere has a finite radius, well-behaved classical trajectories can be found that return to the sphere with nonzero angular momentum p_θ. The reason that Main and Wunner have to calculate classical trajectories at complex energies is that they use a sphere having a vanishing radius $r_0 = 0$. Thus, below a bifurcation, no orbits (with real energies) reach their sphere and complex energy trajectories must be used instead. When closed orbits do exist, it is perfectly acceptable to launch trajectories from the origin. Because certain aspects of calculating closed orbits are simplified by this approach, many practitioners of closed-orbit theory have grown used to a sphere of zero radius. However, as Main and Wunner's work shows, insisting upon using a sphere of zero radius leads to considerable complications when radially launched and returning closed orbits do not exist. I emphasize, however, that when trajectories are launched from a finite sphere, the ghost orbits can be understood as simply being related to classical orbits that return to the sphere nonradially.

Figure 5.1 shows an example of the nonradial ghost orbits for scaled energies near the saddle-node bifurcation of the X_1 exotic orbit (see Fig. B.1). Below the bifurcation energy ($\epsilon_b = -0.115$) nonradial orbits are seen to return to the sphere of scaled radius $\tilde{r}_0 = 0.1$. To include nonradial orbits, such as those shown in Fig. 5.1, into the semiclassical S-matrix, two steps are required. First, the graph of the classical action as a function of the final angle is fit to a polynomial form. For example, the classical actions shown in Fig. 5.1 can be approximated by the polynomial:

$$\tilde{S}(\theta_f, \tilde{p}_{\theta_i} = 0) = \tilde{S}(\theta'_f) + (\theta_f - \theta'_f)a(\epsilon) + \frac{1}{2}(\theta_f - \theta'_f)^2 b(\epsilon). \tag{5.63}$$

The expansion point θ'_f used in this approximation is chosen to be the leftmost point of the family of orbits that return to the sphere. The fit parameters $a(\epsilon)$ and $b(\epsilon)$ are functions of the scaled energy, with the most important dependence being contained in $a(\epsilon)$; as $a(\epsilon)$ crosses through zero from below, the new closed orbits bifurcate. Each type of bifurcation will have a different polynomial associated with it [135]. Once the fit of the action, Eq. (5.63), has been found for the bifurcation being studied, it is used in the Green's function, Eq. (5.62), when the final angle projection integral is performed. In general, the angular dependence of the amplitude A_2 must also be taken into account. Although the

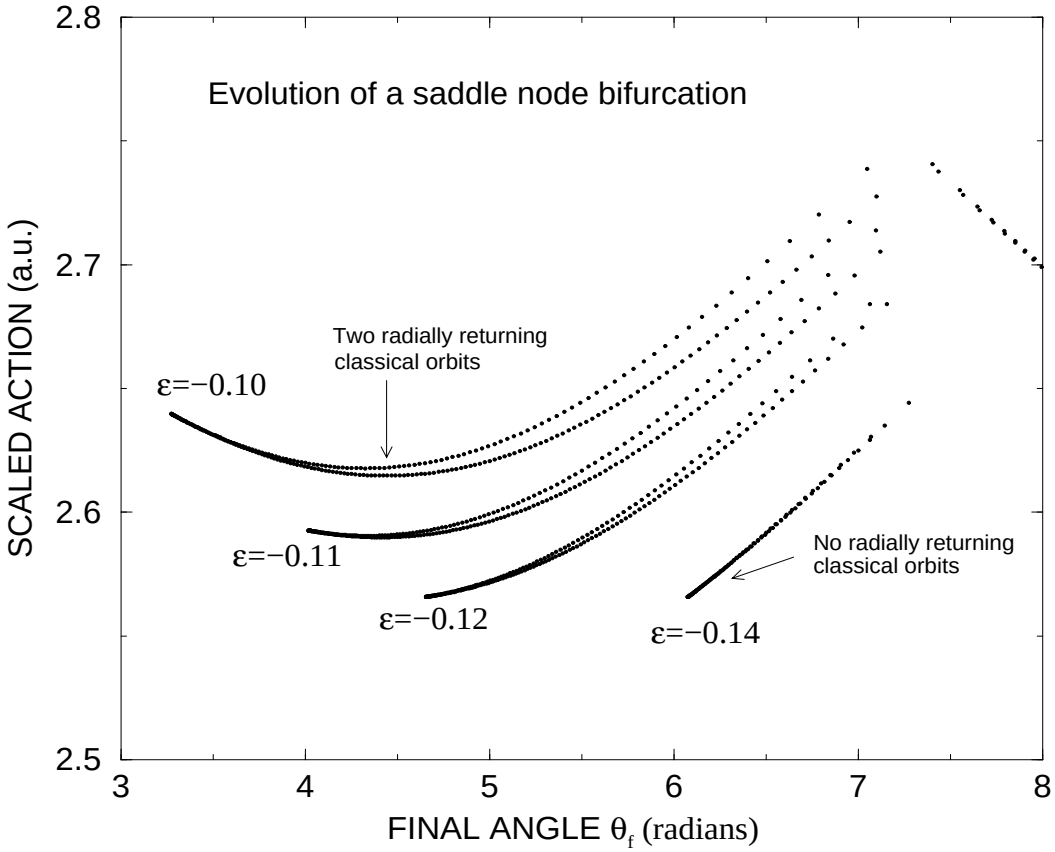

Figure 5.1: The classical scaled action $\tilde{S}(\theta_f)$ is given as a function of the final angle θ_f for trajectories returning to a sphere of scaled radius $\tilde{r}_0 = 0.1$. The trajectories were launched radially outward from the same sphere. At the lower two scaled energies ($\epsilon = -0.14, -0.12$) there is no radially returning orbit (remember that $\tilde{p}_\theta$ is simply the slope of the scaled action in this graph). At a scaled energy of $\epsilon = -0.115$, a pair of exotic orbits (X_{1a}, X_{1b}) bifurcates. These newly existing closed orbits appear as the local minima in the scaled actions at the upper two scaled energies ($\epsilon = -0.11, -0.10$). Most importantly, below the bifurcation energy, nonradial classical trajectories are seen to reach the final sphere.

resulting integrals are typically more complicated than the simple Gaussian forms found in the primitive semiclassical S-matrix, they can often be performed analytically. By carrying out these steps, a uniform semiclassical theory for long-range S-matrix can be derived.

The details of this approach depend strongly on the particular form of the action near the bifurcation. A general study needs to be carried out of the normal forms of the actions near different types of bifurcations. Although Main and Wunner have given such expressions for some types of bifurcations, they use a variable other than the final angle in which to expand the action. It would be useful to transform their normal forms to the final angle representation used here. Many of the details in treating bifurcations still need to be investigated. However, the approach described here provides a beginning point for future investigations. Again, the main advantage of this method is that the classical trajectories do not need to be calculated at complex energies.

5.4 Results

In this chapter, I have developed semiclassical approximations for the long-range S-matrix $\underline{S}^{\mathrm{LR}}$. After the primitive semiclassical approximation to $\underline{S}^{\mathrm{LR}}$ was derived, extensions of the basic method were given for a number of special cases. The main use of the semiclassical scattering matrices of this chapter is to enable a semiclassical approximation for the photoabsorption cross section. This development will be presented in the following chapter (Ch. 6). However, before moving on, it is useful to compare the semiclassical long-range S-matrix, with the accurate quantum S-matrices of the previous chapter (Ch. 4).

Figures 5.2 and 5.3 show such a comparison at a scaled energy of $\epsilon = -0.3$, where the classical dynamics are mostly chaotic. Again, the comparison is performed by studying the recurrences in the matrix elements of $\underline{S}^{\mathrm{LR}}$. Reasonably good quantitative agreement is seen between the semiclassical and quantum results. The main discrepancies are the nonclassical ghost orbits, labeled with the letter “g”, which appear in the quantum recurrence strengths but are absent from the semiclassical. The improved semiclassical formulas for moderate angular momentum and the parallel orbit have been used to obtain these results.

With all of the necessary tools in hand, semiclassical approximations to the photoabsorption cross

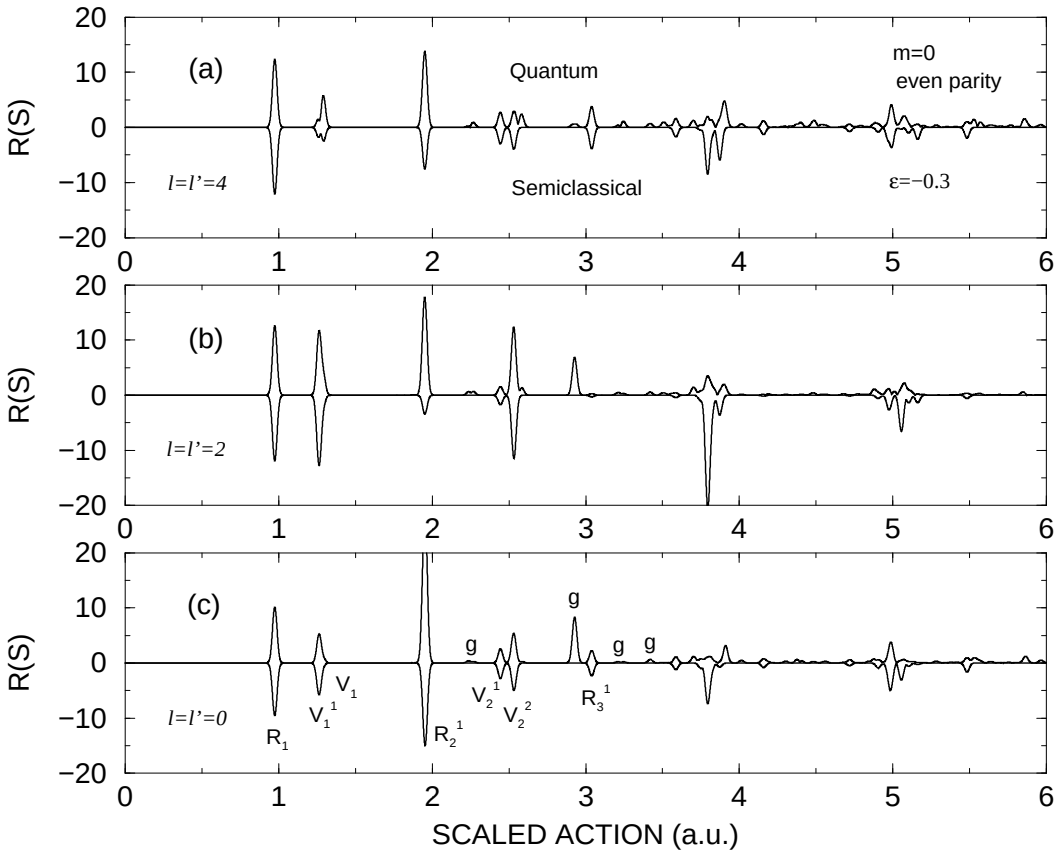

Figure 5.2: A comparison is shown between the quantum (upright) and semiclassical (inverted) recurrence strengths $R(\tilde{S})$ of elements of $\underline{S}^{\rm LR}$. More specifically, the recurrence strengths Eq. (4.27), of $Re(S^{\rm LR}_{00}(w))$ (c), $Re(S^{\rm LR}_{22}(w))$ (b) and $Re(S^{\rm LR}_{44}(w))$ (a), are shown for $m = 0$, even parity states of diamagnetic hydrogen at a scaled energy of $\epsilon = -0.3$. The semiclassical S-matrix has been calculated using the formulas derived in this chapter, Eqs. (5.41) and (5.50). The 26 closed orbits contributing to the semiclassical S-matrix have been calculated numerically. The detailed properties of these closed orbits, including the labeling scheme used here, can be found in Appendix. B. The accurate quantum S-matrix elements were calculated with the variational R-matrix method described in Ch. 4 using a preconvolution smoothing width of $\Delta w = 0.4$. The semiclassical S-matrix has also been preconvolved with the same width. Some of the shorter action closed orbits have been labeled ($R_!, V_1^1, V_1, \ldots$) as have the ghost orbits (g) in the quantum recurrence strengths that correspond to no classical closed orbit. The Fourier transform was carried out over the range of w from 100 to 500.

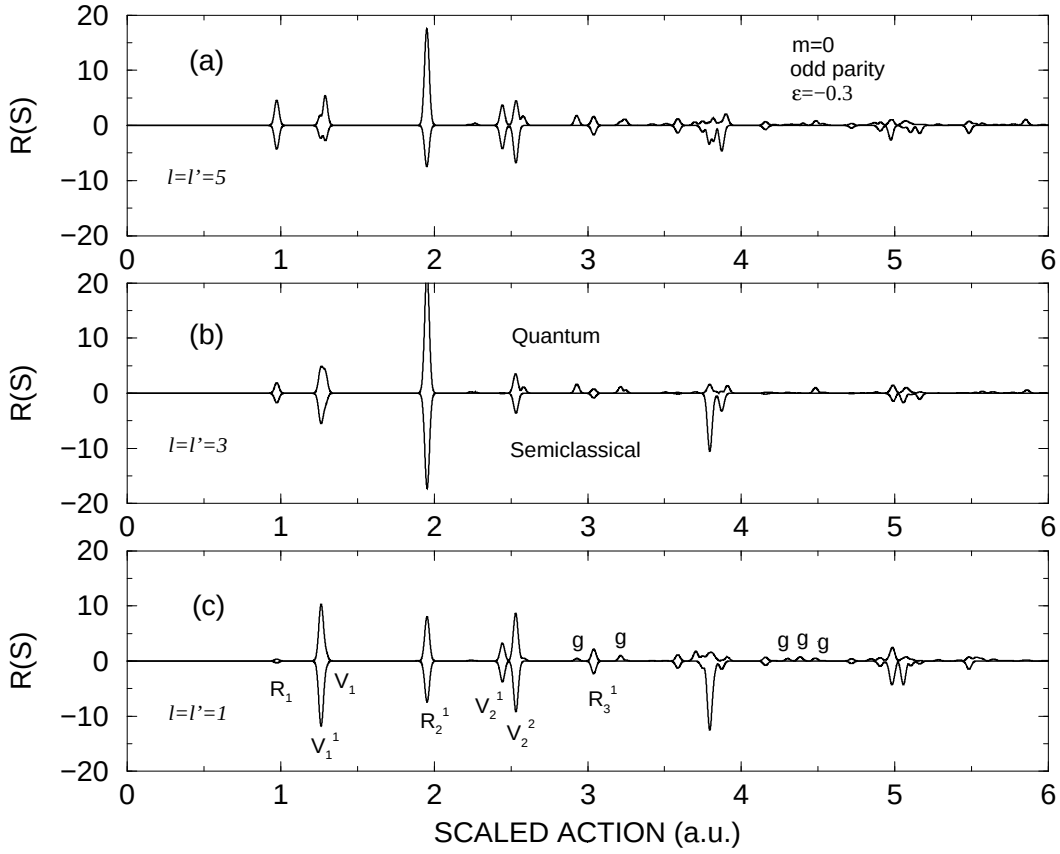

Figure 5.3: A comparison is shown of quantum (upright) and semiclassical (inverted) recurrence strengths for odd parity, $m = 0$, elements of the long-range S-matrix. The Fourier transforms, Eq. (4.27), of the semiclassical and quantum S-matrix elements $Re(S_{11}^{\rm LR}(w))$ (c), $Re(S_{33}^{\rm LR}(w))$ (b) and $Re(S_{55}^{\rm LR}(w))$ (c) shown here were calculated in the same manner as in the even parity case presented in Fig. 5.2. The smoothing width used here is slightly larger, $\Delta w = 0.6$. However, the scaled energy $\epsilon = -0.3$ and range of w values used ($100 - 500$) are the same as in Fig. 5.2. Thus, the same set of closed orbits used for the even parity case also contribute to the recurrence strengths here; only the amplitudes are changed for the different angular momenta. The success of the semiclassical approximation for moderate angular momentum, Eq. (5.60), is seen in the accurate prediction of the odd parity quasi-Landau recurrence peak R_1. The primitive semiclassical approximation gives a vanishing contribution of this orbit because the odd parity spherical harmonics have a node at $\theta_i = \theta_f = \pi/2$.

section can now be studied.

Chapter 6

Ghost orbits and core scattering

In the preceding chapters, a framework has been developed for studying the photoabsorption spectra of atoms in external fields. The main ingredients in the theory are the two scattering matrices $\underline{S}^{\rm LR}$ and $\underline{S}^{\rm core}$, which describe the electron's motion in the long-range and core regions respectively. While the core-region S-matrix is a familiar element of quantum-defect theory, the nontrivial long-range S-matrix $\underline{S}^{\rm LR}$ has been developed in this thesis. Both a quantum mechanical and a semiclassical method for calculating this S-matrix have been given for the case of an atom in a static, external magnetic field.

As closed orbit theory has shown, the ideal way to study the physics of an atomic electron in an external field is to Fourier transform the observables into the time or scaled action domain. Then, global oscillations in the "energy" domain observables are manifested as sharp features at the periods or scaled actions of certain classical orbits of the electron. In Chs. 4 and 5, this type of analysis was applied directly to the elements of the long-range S-matrix $S^{\rm LR}_{ll'}(w)$. As expected, both the accurate quantum $\underline{S}^{\rm LR}$ of Ch. 4 and the semiclassical $\underline{S}^{\rm LR}$ of Ch. 5 display sharp peaks, or **recurrences**, when their elements are Fourier transformed. In fact, there is reasonable quantitative agreement between the recurrences in the quantum and semiclassical long-range S-matrix.

Another main result of this thesis is a formula, Eq. (3.28), for the preconvolved photoabsorption cross section. The current chapter combines this exact quantum cross section with the semiclassical approximation to $\underline{S}^{\rm LR}$ to give a semiclassical approximation for the recurrence spectra of nonhydrogenic atoms. As in the previous few chapters, I will continue to focus on diamagnetic atoms exclusively in this chapter. However, the semiclassical cross section developed here is immediately applicable to atoms in

external electric fields.

Nonhydrogenic atoms have been challenging, if not difficult, for the semiclassical method of closed-orbit theory. As mentioned in the Introduction, closed-orbit theory accurately predicts the recurrence spectrum of hydrogen; typically to within a few percent [38, 37, 39]. In addition, the basic form of the theory has been extended to include nonzero quantum defects of single electron atoms other than hydrogen. This approach, which originated with Gao and Delos [136, 51], has been further developed by Dando *et al.* [53, 52] and also by Shaw and Robicheaux [54] (see also [55]). The physical content of these extensions of closed-orbit theory has been confirmed by both accurate quantum calculations and experiments. Essentially, the ionic core introduces new recurrence peaks that are associated with **primitive closed orbits** (closed orbits of hydrogen), being scattered into each other by the nonhydrogenic core. To include these **core-scattered orbits** in closed-orbit theory, practitioners have used the semiclassical wavefunctions of closed-orbit theory in conjunction with quantum-defect theory, and multiple scattering expansions of the photoabsorption cross section [54, 53]. The resulting formulas for the photoabsorption cross section are similar to the series expansion of the preconvolved cross section derived in Ch. 3 of this thesis. This extension of closed-orbit theory has been successfully applied to lithium ($\mu_s = 0.4$) in an electric field [53], singlet ($\mu_s = 0.14, \mu_p = -0.01$) and triplet ($\mu_s = 0.3, \mu_p = 0.07$) helium in an electric field [54, 49], and an odd parity diamagnetic cesium-like atom ($\mu_p = 0.5$) [53]. In all of these cases, a single quantum defect is large, and the semiclassical theory seems to agree well with accurate quantum calculations. However, for atoms having two or more large quantum defects, such as even parity rubidium ($\mu_s = 3.13, \mu_p = 1.34$), no semiclassical theory has successfully predicted the recurrence spectra. In fact, experiments on barium in an electric field [66, 65] and on rubidium in a magnetic field [137] show poor agreement with closed-orbit theory.

The main difficulty with the multiple scattering expansions of Dando *et al.* and of Shaw and Robicheaux, is that they appear to diverge when more than one large quantum defect is present. More specifically, the core scattered recurrence peaks increase in amplitude with each scattering of the electron off the ionic core. Thus, one cannot approximate the cross section by only including a few terms in the multiple scattering expansion. No progress been made in understanding this significant failure of the

extensions of closed-orbit theory to nonhydrogenic atoms. Thus, it is currently not known whether the divergence of the multiple scattering expansions is caused by the semiclassical approximations made, or if it is the basic nature of the series itself. This distinction must be understood in order to improve the theory.

In this chapter, I show how a convergent semiclassical photoabsorption cross section for nonhydrogenic atoms can be derived with the tools developed in this thesis. Two important elements are needed for this development, First, a surprising relationship between nonclassical ghost orbits and core-scattered orbits must be taken into account in the semiclassical cross section. The details of this relationship are given in Sec. 6.2. It will be seen that ghost orbits and core-scattered orbits are two aspects of the same physics. In Sec 6.3, this relationship between ghost and core-scattered orbits is used to obtain a resummed semiclassical cross section.

Second, the preconvolution of the cross section described in Ch. 3 is needed for the resummed semiclassical cross section to converge. The effect of the preconvolution technique is to damp out the long scaled action recurrence peaks that cause the unconvolved semiclassical theory to diverge. After the resummed semiclassical approximation is derived, it is applied to three diamagnetic atoms: hydrogen, lithium, and rubidium. In all of these cases, the resummed semiclassical cross section gives good agreement with accurate quantum calculations for both the cross section as a function of the scaled field w, $\sigma(w)$, as well as for the recurrence spectra.

6.1 Primitive semiclassical approximation

Obtaining a semiclassical expression for the cross section is more complicated than one might initially expect. The most obvious route is to use the semiclassical approximations for the long range S-matrix $\underline{S}^{\mathrm{LR}}(w)$ developed in the previous chapter (Ch. 5), Eqs. (5.41) and (5.50), in the expression for the preconvolved cross section of Ch. 3:

$$\sigma^{(\Delta w)}(w) = 4\pi^2\alpha\omega\,\mathrm{Re}\,\vec{d}\left[\underline{1} + 2\underline{S}^{\mathrm{core}}\underline{S}^{\mathrm{LR}}(w) + 2\left(\underline{S}^{\mathrm{core}}\underline{S}^{\mathrm{LR}}(w)\right)^2 + 2\left(\underline{S}^{\mathrm{core}}\underline{S}^{\mathrm{LR}}(w)\right)^3 + \cdots\right]\vec{d}^{\dagger}. \tag{6.1}$$

When the scaled field is evaluated at a complex value of $w + i\Delta w/2$, the resulting cross section is effectively convolved with a Lorentzian of width Δw. Each term in this expansion gives recurrence peaks that are associated with the electron scattering off the ionic core a number of times. The semiclassical S-matrix of the previous chapter is given as a sum over primitive closed orbits p and can be written in the form (see Eq. 5.41):

$$\underline{S}^{\mathrm{LR}}(w) = \sum_p \underline{A}_p(w) e^{iw\tilde{S}_p} \times e^{-\tilde{S}_p \Delta w/2}. \tag{6.2}$$

Here, the matrix $\underline{A}_p(w)$ contains all of the information about the closed orbits being summed over and depends only weakly on the scaled field. With this approximation, each term in the expansion of the cross section generates recurrence peaks at the repetitions ($n \times \tilde{S}_p$, $n = 1, 2, \ldots \infty$) and combinations ($\tilde{S}_p + \tilde{S}_q$, $\tilde{S}_p + \tilde{S}_q + \tilde{S}_r$, etc.) of the primitive closed orbits. Initially, it might seem like this is exactly the qualitative picture that is desired for the semiclassical cross section. However, there is a critical flaw in this primitive approach to the semiclassical cross section.

The difficulty with this primitive semiclassical approximation to the photoabsorption cross section is that it fails to give accurate recurrence spectra for hydrogen. It is expected that hydrogen should be the easiest atom to treat, as the effect of the "core" - which is just a lone proton - is completely trivial. However, the expansion of the cross section, Eq. (6.1), predicts the presence of core-scattered recurrences for this elementary atom. When the core region S-matrix for hydrogen, $\underline{S}^{\mathrm{core}} = \underline{1}$, is used in the cross section, Eq. (6.1), all of the terms that generate core scattered recurrence peaks, such as $\left(\underline{S}^{\mathrm{LR}}(w)\right)^2$ and $\left(\underline{S}^{\mathrm{LR}}(w)\right)^3$, are still present. This prediction of core-scattered recurrences in diamagnetic hydrogen is in conflict with both accurate quantum calculations and experiments. In the two decades that recurrence spectra have been studied, core-scattered recurrences have never been detected in hydrogen at any value of the scaled energy ϵ or scaled field w. Thus, this reflects a fundamental problem with this primitive semiclassical approximation.

A quantitative example of this difficulty is shown in Fig. 6.1, where the accurate quantum recurrence spectra is compared with the primitive semiclassical approximation described here for hydrogen at a scaled energy of $\epsilon = -0.3$. The recurrence strength $R(\tilde{S})$, Eq. (4.27), of the cross section $\sigma(w)$

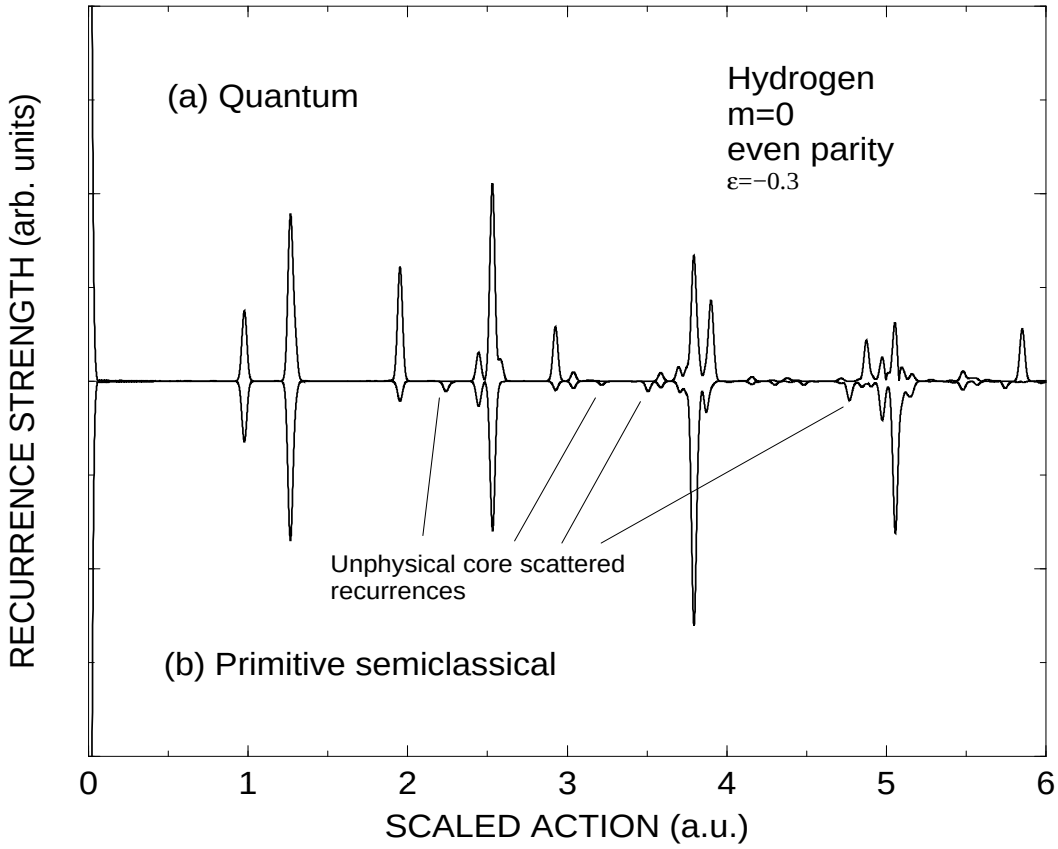

Figure 6.1: A comparison is shown between the accurate quantum (upright) and primitive semiclassical (inverted) recurrence strength for diamagnetic hydrogen at a scaled energy of $\epsilon = -0.3$. The purpose of this figure is to show the unphysical core-scattered recurrences that are predicted by the naive use of the semiclassical long-range S-matrix in the expansion of the cross section, Eq. (6.1). These peaks are not seen in accurate quantum calculations. The recurrence spectra are for photoabsorption from the $2p, m = 0$ state to $m = 0$, even parity final states.

is shown for even parity, $m = 0$ final states. The unphysical core-scattered peaks in the semiclassical recurrence strength are indicated by lines. The range of w that has been Fourier transformed here is $w = 100 - 500$ and the preconvolution width is $\Delta w = 0.4$. The agreement between the quantum and primitive semiclassical approximation is seen to be poor. This is in contrast to closed-orbit theory, which yields excellent predictions for diamagnetic hydrogen at this scaled energy. Clearly for my semiclassical theory for the cross section to succeed for complex atoms, the simple case of hydrogen must first be understood.

There is one clue that points the way to resolve this problem. The careful reader will have noticed that the analytical structure of the cross section suggests that core scattered recurrences should **also** be seen when accurate quantum S-matrices are used. The core scattered terms in the cross section, such as $\left(\underline{S}^{\mathrm{LR}}(w)\right)^2$ and $\left(\underline{S}^{\mathrm{LR}}(w)\right)^3$, are present whether approximate semiclassical S-matrices or accurate quantum S-matrices are used. However, as Fig. 6.1 demonstrates, the core-scattered orbits don't appear in the final cross section when accurate S-matrices are used. This suggests that some yet unknown feature in the accurate quantum calculation ensures that the core-scattered orbits are eliminated. In the following section, I use the accurate quantum S-matrices to study the preconvolved cross section for diamagnetic hydrogen. This study will reveal an intimate connection between the core-scattered orbits and other nonclassical orbits, the so-called ghost orbits.

6.2 Cancellation between ghost orbits and core scattered orbits

Chapter 3 discussed the physical insight available in the preconvolved photoabsorption cross section. It was argued that many of the ideas of closed-orbit theory are already available in the exact cross section. Because the scattering matrices $\underline{S}^{\mathrm{LR}}$ and $\underline{S}^{\mathrm{core}}$ give quantum amplitudes for the electron to scatter off the long-range potentials and ionic core, the cross section, Eq. (6.1), can be viewed as a Feynman-like sum over quantum paths. Each term in the expansion of $\sigma(w)$ contains information about certain classes of quantum paths. By studying the recurrences in each term, the contributions of certain types of paths can be detected. The main purpose of this section is to study the fate of core-scattered recurrences in hydrogen.

By studying the exact quantum recurrence spectra for hydrogen as well as the topologies of the core-scattered and ghost orbits, I will argue that the following statement is true: in the recurrence spectrum of diamagnetic hydrogen, both ghost and core-scattered orbits exist, but neither appear in the cross section because they always conspire to cancel each other out. While the presence of the core-scattered and ghost orbits cannot be directly measured by any physical observable, their effects are significant. This will be seen in the following section where this surprising cancellation effect is used to obtain an accurate semiclassical approximation for the cross section.

6.2.1 Observation in the quantum recurrence spectra

The best place to look for the presence of core-scattered or ghost orbits is in the exact quantum cross section. Here, both of these features are treated without approximation. In this subsection, I present the results of accurate quantum calculations for diamagnetic hydrogen. A study of the recurrence strengths in the cross section unambiguously shows the universal cancellation between ghost and core-scattered paths.

To perform this analysis, it is useful to write the total cross section, Eq. (6.1), in the form:

$$\sigma(w) = \sum_j \sigma_j(w), \tag{6.3}$$

where,

$$\sigma_0(w) = Re\left\{\vec{d}\vec{d}^{\dagger}\right\}, \tag{6.4}$$

$$\sigma_{j>0}(w) = 2Re\left\{\vec{d}\left(\underline{S}^{\text{core}}\underline{S}^{\text{LR}}\right)^j \vec{d}^{\dagger}\right\}. \tag{6.5}$$

Note that the factor $4\pi^2\alpha\omega$ that is present is the cross section has been left out of these equations. Following the work of others (see [39] for example), I will leave this factor out when studying the recurrences of the cross section. As stated above, each term in the expansion, Eq. (6.3), encapsulates different types of quantum paths. The zero order term σ_0 is constant with respect to w and corresponds to quantum paths with zero length. This piece gives the smooth background piece of the convolved cross section. The first order cross section $\sigma_1(w)$ contains information about the primitive quantum paths that are related to the closed classical orbits. Also, this piece exhibits recurrences due to the nonclassical

ghost orbits. Again these ghost orbits are not really classical orbits at all; they are quantum paths that appear in the long-range S-matrix but have no classical analogue. The second order cross section $\sigma_2(w)$ contains information about quantum paths that make two trips into the long-range region; these are the core-scattered orbits. Likewise, the higher order terms $\sigma_j(w)$ are made up of core-scattered orbits that scatter off the long-range region j times.

First, it is useful to verify that the exact quantum recurrence strength of the total cross section $\sigma(w)$ shows no core-scattered recurrences. To demonstrate this, Fig. 6.2 presents the recurrence strength $R(\tilde{S})$ of $\sigma(w)$ for diamagnetic hydrogen at a range of scaled energies. At the lowest scaled energy shown ($\epsilon = -0.9$), the classical dynamics is nearly integrable, with only two orbits, the quasi-Landau R_1 and parallel V_1 orbits (and their repetitions), giving strong peaks in the scaled action domain. As the scaled energy increases, the underlying classical dynamics become chaotic and more recurrence peaks appear through bifurcations of the closed orbits. Note that no divergences in the recurrence amplitudes are seen as these bifurcations take place. At all of the scaled energies shown, there are no core-scattered recurrences, which would appear at the scaled actions of combinations of the primitive closed orbits. This confirms the observations of previous calculations and experiments [39]. The calculations shown are for even parity, $m = 0$ states of hydrogen over the range $w = 100 - 500$. A preconvolution width of $\Delta w = 0.4$ has been used.

Next, the recurrence strength $R(\tilde{S})$ of the first order cross section $\sigma_1(w)$ is presented (Fig. 6.3) to isolate the contributions of ghost orbits to the cross section. The recurrence strengths are shown for the same parameters (even parity, $m = 0$, $\Delta w = 0.4$, $\epsilon = -0.9 \rightarrow = -0.3$) as the total cross section of Fig. 6.2 to allow a direct comparison between the full and first order cross sections. The strong similarity between the two suggests that most of the short scaled action recurrence peaks observed in the total cross section (Fig. 6.2) are due to primitive closed orbits represented in the linear cross section $\sigma_1(w)$. In addition to the primitive closed orbits ($R_1, V_1^1, \ldots$) that contribute to $\sigma_1(w)$, ghost orbit recurrence peaks are seen. I have labeled these peaks with the letter "g" and have used dashed lines to show their development with scaled energy. Comparison of Fig 6.2 (total) with Fig 6.3 (first order) shows that these ghost peaks do not survive in the total cross section. Note however, that very close to the bifurcation

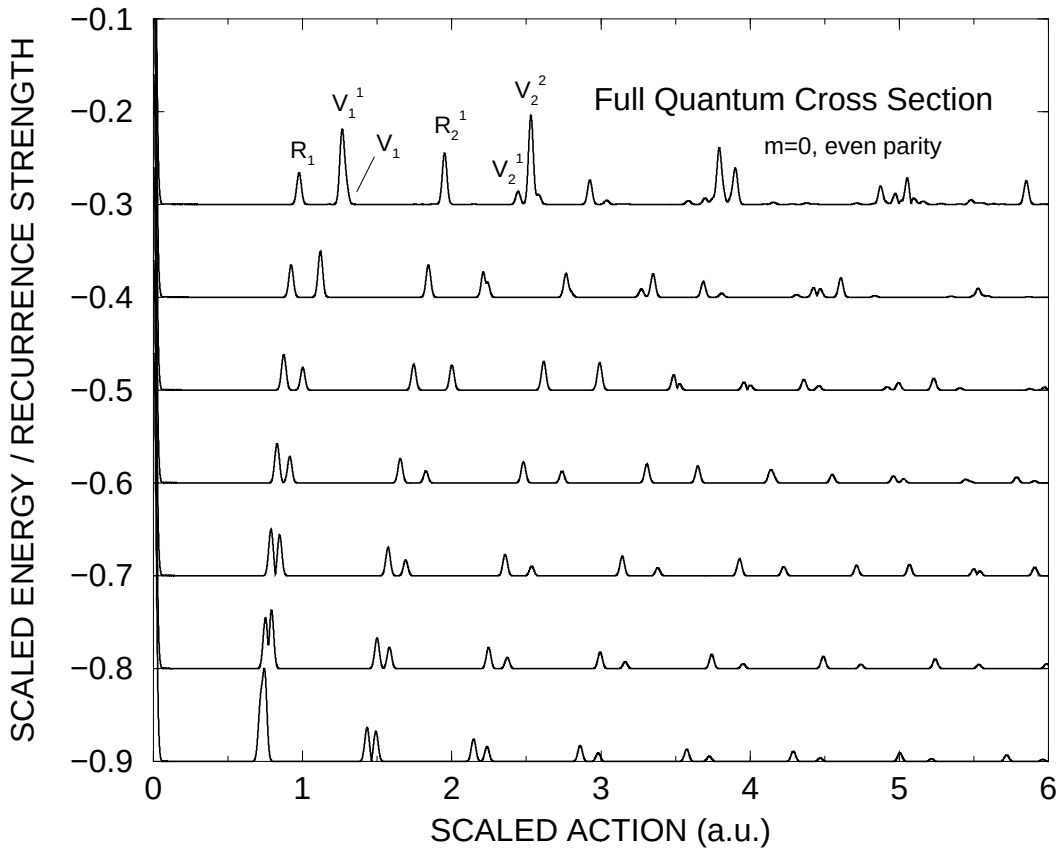

Figure 6.2: The Fourier transform, or recurrence strength, of the preconvolved photoabsorption cross section $\sigma(w)$ for diamagnetic hydrogen is given at seven scaled energies ($\epsilon = -0.9 \rightarrow -0.3$). These results were obtained by using an accurate quantum long-range S-matrix $\underline{S}^{\rm LR}$ and $\underline{S}^{\rm core} = \underline{1}$ in the exact formula for the photoabsorption cross section, Eq. (3.28). The shortest action primitive closed orbits underlying the quantum recurrence peaks are labeled ($R_1, V_1^1, \ldots$) using the notation of Appendix B. While all orders of core-scattering are included in these calculations through the matrix $\left(\underline{1} - \underline{S}^{\rm LR}\right)^{-1}$, core scattered peaks are not present in the final recurrence spectra. This is consistent with previous experiments and calculations. The dipole vector $\vec{d}$ needed for absorption from the $2p, m = 0$ state to the even parity, $m = 0$ final states shown here is given in [38, 37]. The range of w that has been Fourier transformed is $100 - 500$ and a smoothing width of $\Delta w = 0.4$ is used. Compare this recurrence spectra of the total cross section with that of the first order (Fig. 6.3) and second order (Fig. 6.4) terms of the cross section.

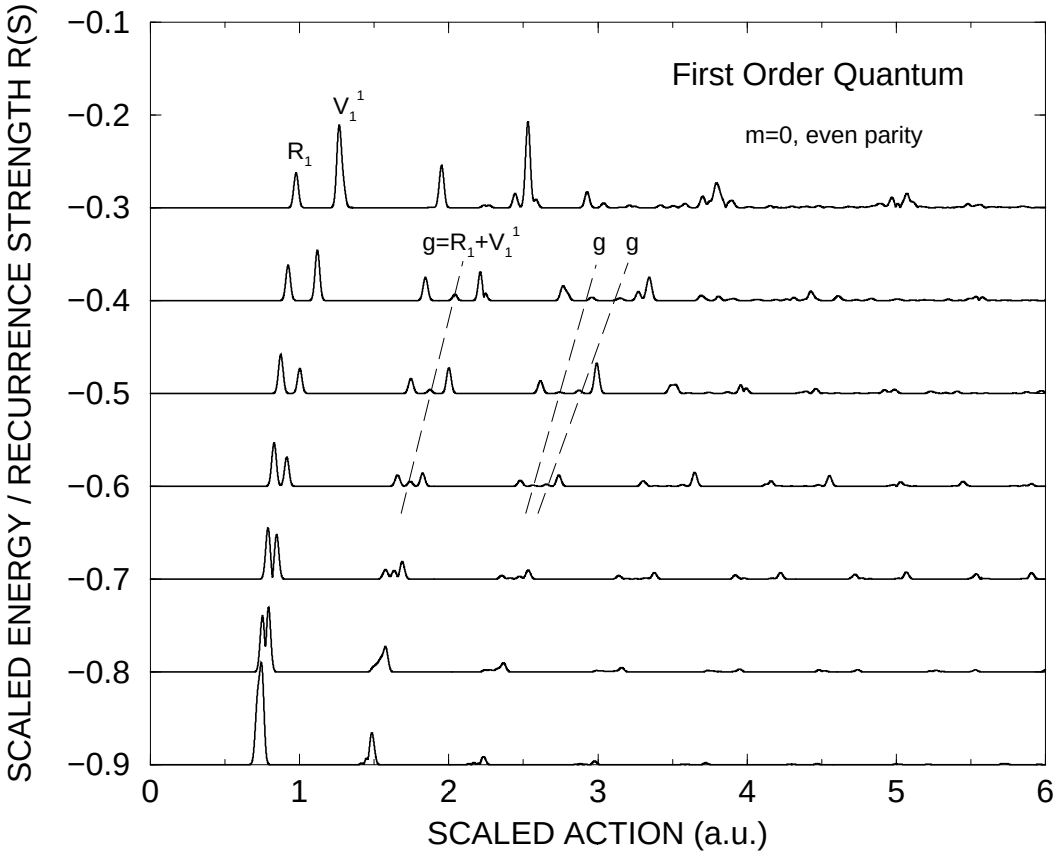

Figure 6.3: The recurrence strength of the linear term in the expansion of the photoabsorption cross section $2Re\vec{d}\underline{S}^{\rm LR}(w)\vec{d}^{\dagger}$ is plotted, again for diamagnetic hydrogen (even parity, $m = 0$) at the seven scaled energies shown in Fig. 6.2. The long-range S-matrix $\underline{S}^{\rm LR}$ is provided through accurate quantum calculations. Thus, nonclassical recurrences due to ghost orbits are seen (marked by dashed lines). Because only the linear term in the cross section is shown here, all of the complications of core-scattered recurrences are not present. A comparison with Fig 6.2 shows that the ghost orbits seen in this linear term of the cross section do not survive once the higher order terms in the cross section are included. This suggests that the ghost orbits are canceled by the core-scattered orbits. The range of w that has been Fourier transformed is $100 - 500$ and a smoothing width of $\Delta w = 0.4$ has been used.

points where the ghost orbits become real closed orbits, the bifurcating ghosts give small contributions to the total recurrence strength [63].

Finally, the recurrence strength of the second order cross section $\sigma_2(w)$ is shown (Fig. 6.4) to yield information about the core-scattered recurrences. Here, only the quantum paths that scatter off the long-range and core regions twice are represented. Two types of recurrences are seen in this second order cross section. First, repetitions of the primitive closed orbits ($2R_1, 2V_1^1$) are seen. These are relatively strong features in the recurrence strength, and they end up contributing to the total cross section. Second, smaller peaks, associated with core-scattered orbits appear in Fig. 6.4 and are labeled with the letters "cs." A comparison with Fig 6.2 shows that none of these core-scattered peaks survive in the total cross section. Furthermore, it is seen that the core-scattered peaks have the same scaled actions and amplitudes as the ghost orbits of Fig. 6.3.

These three figures (Figs. 6.2-6.4) give a clear account of why core-scattered orbits never appear in the recurrence strength of the total cross section. It is because ghost orbits and core-scattered orbits have identical scaled action and amplitudes, but give opposite contributions in the total cross section to cancel each other perfectly. This cancellation effect appears to be a universal feature of diamagnetic hydrogen. It is seen at all values of the scaled energy ϵ studied here.

6.2.2 Observation in the shapes of the classical orbits

The intimate relationship between core-scattered orbits and ghost orbits can also be seen by looking at the topologies of the classical trajectories. Some examples of plots of core-scattered orbits, and the ghost orbits they cancel with are shown in Fig. 6.5. Here, the paths of the trajectories are shown in cylindrical coordinates (ρ, z) allowing ρ to become negative. Without exception, the core-scattered trajectories (right) follow the same paths as their ghost counterparts (left). The only difference is that the core-scattered orbits return exactly to the origin at an intermediate time, whereas the ghost orbits only scatter by the core with high angular momentum at this intermediate time.

Of course these classical orbits are only representing the full quantum wavefunction that propagates in the outer region. The similarities between ghost and core-scattered orbits (their actions, ampli-

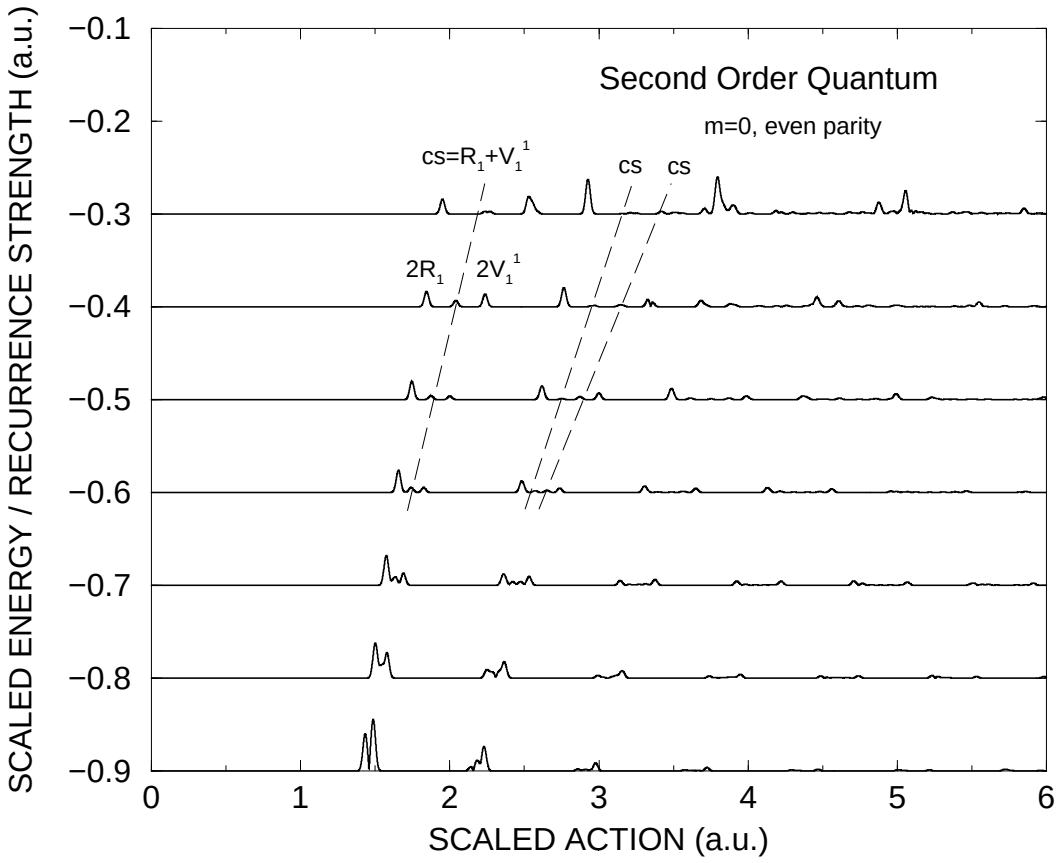

Figure 6.4: The recurrence strength of the quadratic term in the expansion of the photoabsorption cross section $2Re\vec{d}\left(\underline{S}^{\mathrm{LR}}(w)\right)^2\vec{d}^{\dagger}$ is plotted, again for diamagnetic hydrogen (even parity, $m = 0$) at the seven scaled energies shown in Figs. 6.2 and 6.3. The long-range S-matrix $\underline{S}^{\mathrm{LR}}$ is provided through accurate quantum calculations. Because just the quadratic term in the cross section is shown here, only recurrences associated with the repetitions ($2\tilde{S}_p$) and combinations ($\tilde{S}_p + \tilde{S}_q$) of two closed orbits are seen. The core scattered orbits, labeled with the letters "cs" and dashed lines, are seen to exist in exactly the same location as the nonclassical ghost orbits seen in the recurrence strength of the linear part of the cross section (see Fig. 6.3). In the recurrence strength of the total cross section, Fig. 6.2, the core-scattered recurrence peaks as well as the ghost orbits are not present. This is strong evidence that, at least in hydrogen, the core-scattered and ghost orbits universally cancel each other. The range of w represented and the smoothing width Δw is the same as in Figs. 6.2 and 6.3.

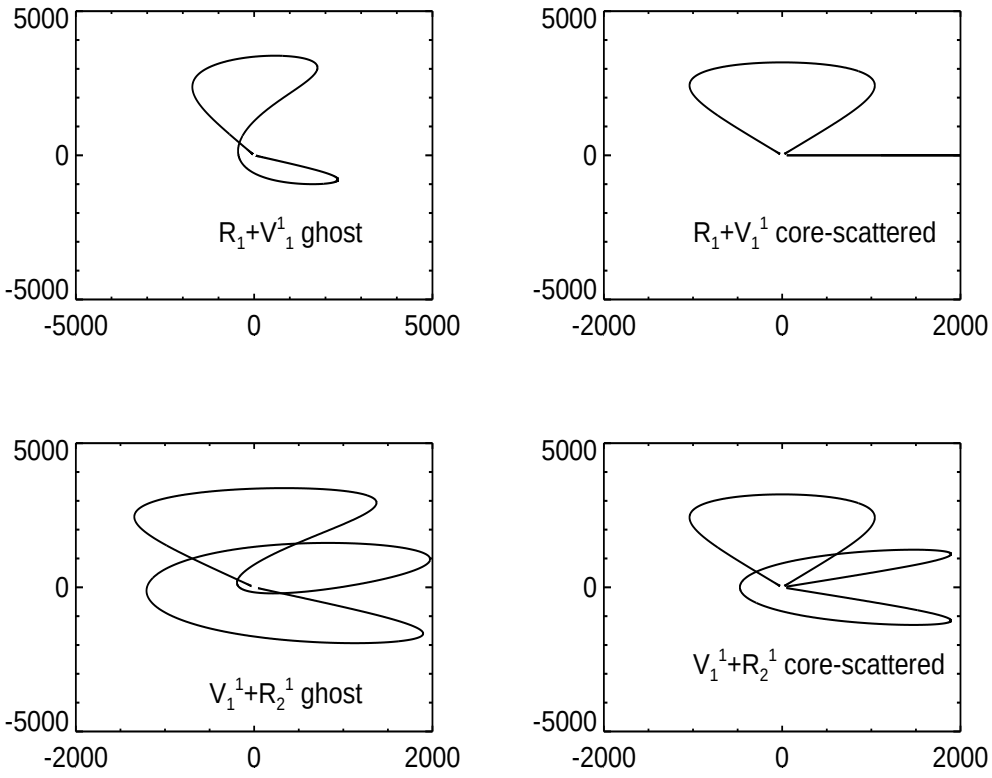

Figure 6.5: This figure shows the topological similarity between the ghost orbits (left) and the core-scattered orbits (right). The labeling scheme used here is described in Appendix B. While only two examples of this similarity are provided here, every ghost orbit that I have looked at is similar to some combination of primitive closed orbits. This suggests that the relationship is nearly universal in diamagnetic hydrogen.

tudes, and shapes) suggest that a single quantum wavefront is responsible for both of these effects. That is, from a quantum mechanical perspective, core-scattered and ghost orbits in hydrogen represent exactly the same physics.

6.2.3 Unanswered questions

Before moving on, it is useful to address some of the unanswered questions about this observed relationship between ghost orbits and core-scattered orbits. First, while it appears that the cross section includes core-scattered orbits semiclassically, ghost orbits are not included in the primitive semiclassical approximation. To further strengthen the argument for the universal cancellation effect seen in hydrogen, it would be advantageous to have a semiclassical theory for the ghost orbits. In the previous chapter, progress in this direction was given where S-matrices for bifurcations were discussed (Sec. 5.3.3). Indeed, all of the ghost orbits seen in the quantum recurrence spectra become real orbits at the bifurcation points. If a semiclassical theory of bifurcations was made quantitative, it might be possible to predict the cancellation effect rather than simply observe it. It would also be interesting to understand why this cancellation occurs. For instance, is this a general property of nonintegrable systems? Or is it related to the nature of the Coulomb potential experienced by the electron near the core?

Another point worth addressing is whether or not this cancellation between ghost and core-scattered orbits is significant. In closed-orbit theory, neither of these effects is included in the semiclassical treatment, and the theory works very well for hydrogen. Because experiments can only observe the total photoabsorption cross section, the core-scattered recurrences seen in the theoretical second order cross section $\sigma_2(w)$ can never be directly observed. Thus one might argue that the "existence" of the core-scattered orbits rests on shaky grounds at best. If certain predictions of a theory can never be observed in a physical system, are those predictions true or even meaningful? Whether or not this is the case, I will leave to the philosophers of science.

The important point here is that incorporation of this observed cancellation effect into the theory allows an improved semiclassical formula for the cross section to be derived. In the final section of this chapter (Sec. 6.3), I derive this improved semiclassical theory and show that even though the core-

scattered recurrences in diamagnetic hydrogen can never be observed, their existence has important consequences for semiclassical approximations to the photoabsorption cross section.

6.3 Resummed semiclassical cross section

This chapter began by presenting a primitive semiclassical approximation to the photoabsorption cross section of an atom in an external magnetic field. In the primitive approximation, the semiclassical approximation of $\underline{S}^{\mathrm{LR}}$, Eq. (6.1), was used directly in the exact expression for the energy smoothed photoabsorption cross section, Eq. (6.1). Immediately, this approximation was seen to predict unphysical core-scattered recurrences for diamagnetic hydrogen. Furthermore, any attempt to use this primitive semiclassical approach for atoms other than hydrogen would fail as well. Luckily, this is not the end of the story for semiclassical approximations of the cross section.

In the previous section, an interesting relationship between core scattered orbits and so called ghost orbits was uncovered using a term by term analysis of the recurrence spectra determined through an accurate quantum calculation. Here the mystery of core-scattered orbits in hydrogen was uncovered. A seemingly universal phenomenon was observed: the core-scattered recurrence peaks are canceled by ghost orbit recurrences. These ghost peaks correspond to quantum mechanical paths of the electron in the long-range region that have no associated classical closed orbit. In this final section, this observed effect is put into mathematical terms and used to obtain an accurate semiclassical cross section.

6.3.1 General approach

The improved semiclassical cross section can be derived by rearranging the expansion of the cross section, Eq. (6.1), to take the cancellation into account. This amounts to a **resummation** of the cross section. For this task, it is useful to focus on the matrix,

$$\begin{aligned}\left[\underline{1}-\underline{S}^{\mathrm{core}}\underline{S}^{\mathrm{LR}}\right]^{-1}\left[\underline{1}+\underline{S}^{\mathrm{core}}\underline{S}^{\mathrm{LR}}\right] &= \underline{1}+2\underline{S}^{\mathrm{core}}\underline{S}^{\mathrm{LR}} \\ &+ 2\underline{S}^{\mathrm{core}}\underline{S}^{\mathrm{LR}}\underline{S}^{\mathrm{core}}\underline{S}^{\mathrm{LR}} \\ &+ 2\underline{S}^{\mathrm{core}}\underline{S}^{\mathrm{LR}}\underline{S}^{\mathrm{core}}\underline{S}^{\mathrm{LR}}\underline{S}^{\mathrm{core}}\underline{S}^{\mathrm{LR}}+\cdots,\end{aligned} \tag{6.6}$$

that is present in the total cross section. With the ghost orbits in mind the semiclassical S-matrix can be written as a sum over both primitive closed orbits "p" and prebifurcated ghost orbits "g":

$$\underline{S}^{\mathrm{LR}} = \sum_p \underline{S}_p + \sum_g \underline{S}_g . \tag{6.7}$$

The semiclassical S-matrix $\underline{S}_p$ for each of the terms in the sum over primitive closed orbits is given by the semiclassical formulas developed the previous chapter (Eq. 5.39). For the ghost pieces $\underline{S}_g$, there is currently no semiclassical approximation. However, this is not a problem because these terms will drop out of the final result due to the cancellation effect. The key in performing the resummation of the cross section is to write the core region S-matrix in terms of a hydrogenic piece (the identity matrix, $\underline{1}$) and a nonhydrogenic piece, which I will denote as the matrix $\underline{\Delta}$:

$$\underline{S}^{\mathrm{core}} = \underline{1} + \underline{\Delta}. \tag{6.8}$$

The resummation of Eq. (6.6) consists of using this form of $\underline{S}^{\mathrm{core}}$, along with the long-range S-matrix of Eq. (6.7). After terms are multiplied out, the series is reordered in increasing powers of the matrix $\underline{\Delta}$. For example, the quadratic term in Eq. (6.6) becomes,

$$2\underline{S}^{\mathrm{core}}\,\underline{S}^{\mathrm{LR}}\,\underline{S}^{\mathrm{core}}\,\underline{S}^{\mathrm{LR}} = 2\underline{S}^{\mathrm{core}}\left(\underline{S}^{\mathrm{LR}}\right)^2 + 2\underline{S}^{\mathrm{core}}\,\underline{S}^{\mathrm{LR}}\underline{\Delta S}^{\mathrm{LR}}. \tag{6.9}$$

Likewise, the cubic term becomes,

$$\begin{aligned} 2\left(\underline{S}^{\mathrm{core}}\underline{S}^{\mathrm{LR}}\right)^3 &= 2\underline{S}^{\mathrm{core}}\left(\underline{S}^{\mathrm{LR}}\right)^3 + 2\underline{S}^{\mathrm{core}}\left(\underline{S}^{\mathrm{LR}}\right)^2\underline{\Delta S}^{\mathrm{LR}} \\ &+ 2\underline{S}^{\mathrm{core}}\,\underline{S}^{\mathrm{LR}}\underline{\Delta}\left(\underline{S}^{\mathrm{LR}}\right)^2 + 2\underline{S}^{\mathrm{core}}\,\underline{S}^{\mathrm{LR}}\underline{\Delta S}^{\mathrm{LR}}\underline{\Delta}. \end{aligned} \tag{6.10}$$

When this procedure is carried out to all orders, and the result is ordered in powers of the matrix $\underline{\Delta}$, Eq. (6.6) takes the form,

$$\begin{aligned} \left[\underline{1} - \underline{S}^{\mathrm{core}}\underline{S}^{\mathrm{LR}}\right]^{-1}\left[\underline{1} + \underline{S}^{\mathrm{core}}\underline{S}^{\mathrm{LR}}\right] &= \underline{1} + 2\underline{S}^{\mathrm{core}}\tilde{\underline{S}}^{\mathrm{LR}} \\ &+ 2\underline{S}^{\mathrm{core}}\tilde{\underline{S}}^{\mathrm{LR}}\underline{\Delta\tilde{S}}^{\mathrm{LR}} \\ &+ 2\underline{S}^{\mathrm{core}}\tilde{\underline{S}}^{\mathrm{LR}}\underline{\Delta\tilde{S}}^{\mathrm{LR}}\underline{\Delta\tilde{S}}^{\mathrm{LR}}, \\ &+ \cdots \end{aligned} \tag{6.11}$$

where the **resummed semiclassical S-matrix** $\underline{\tilde{S}}^{\mathrm{LR}}$ now involves powers of the long-range S-matrix of Eq. (6.7):

$$\underline{\tilde{S}}^{\mathrm{LR}} = \underline{S}^{\mathrm{LR}} + \left(\underline{S}^{\mathrm{LR}}\right)^2 + \left(\underline{S}^{\mathrm{LR}}\right)^3 + \left(\underline{S}^{\mathrm{LR}}\right)^4 + \cdots . \tag{6.12}$$

Now the cancellation of the ghost and core-scattered orbits can be taken into account. Using the form of $\underline{S}^{\mathrm{LR}}$, Eq. (6.7), in the resummed S-matrix $\underline{\tilde{S}}^{\mathrm{LR}}$, Eq. (6.12), and focusing on the first two terms, the following expression is found:

$$\underline{\tilde{S}}^{\mathrm{LR}} = \sum_p \underline{S}_p + \sum_g \underline{S}_g + \sum_{p \neq q} \underline{S}_p \underline{S}_q + \sum_p \left(\underline{S}_p\right)^2 . \tag{6.13}$$

Here, the first order ghost orbit contributions $\underline{S}_g$ are displayed right next to the second order core-scattered orbits $\underline{S}_p \underline{S}_q$, with which they must cancel. Thus, the cancellation between ghost orbits and core-scattered orbits can be expressed mathematically as:

$$\sum_g \underline{S}_g + \sum_{p \neq q} \underline{S}_p \underline{S}_q = 0. \tag{6.14}$$

It is important to note that this condition has not been derived from first principles; it is imposed on the expansion of the cross section based on the observed cancellation described above. A derivation of this relationship is desirable, but it remains unsolved and will probably be a difficult result to achieve. When this cancellation condition, Eq. (6.14), is taken into account, the resummed long range S-matrix becomes,

$$\underline{\tilde{S}}^{\mathrm{LR}} = \sum_p \underline{S}_p + \sum_p \left(\underline{S}_p\right)^2 + \sum_p \left(\underline{S}_p\right)^3 \cdots , \tag{6.15}$$

where the powers of the S-matrices $\underline{S}_p$ in this expression generate the repetitions of the primitive closed orbits. With one final approximation the final form of the improved semiclassical cross section can be given; although initially, as a series expansion. The nth repetition of the pth primitive closed orbit will be included by running that closed orbit through n times **classically** rather than multiplying the S-matrix n times such as in $\left(\underline{S}_p\right)^n$. Then the information of the classically repeated orbit is used in the semiclassical formula for the S-matrix of the previous chapter. That is, once a repetition of an orbit has been calculated classically, it is treated just like a primitive closed orbit and is summed over in the long-range S-matrix.

Then the resummed semiclassical long-range S-matrix, Eq. (6.15), has the simple form,

$$\underline{\tilde{S}}^{\mathrm{LR}} = \sum_p \sum_n \underline{S}_p^{(n)}, \tag{6.16}$$

where the notation $\underline{S}_p^{(n)}$ denotes the nth repetition of the pth closed orbit.

The improved semiclassical cross section can then be written down using Eq. (6.11) for the expansion of the cross section, Eq. (6.8) for the matrix $\underline{\Delta}$, and Eq. (6.16) for the resummed long-range S-matrix $\underline{\tilde{S}}^{\mathrm{LR}}$:

$$\begin{aligned}\sigma^{\Delta w}(w) \sim \mathrm{Re}\vec{d}\Big(\underline{1} + 2\underline{S}^{\mathrm{core}}\underline{\tilde{S}}^{\mathrm{LR}} \quad &+ \quad 2\underline{S}^{\mathrm{core}}\underline{\tilde{S}}^{\mathrm{LR}}\left(\underline{S}^{\mathrm{core}} - \underline{1}\right)\underline{\tilde{S}}^{\mathrm{LR}} \\ &+ \quad 2\underline{S}^{\mathrm{core}}\underline{\tilde{S}}^{\mathrm{LR}}\left(\underline{S}^{\mathrm{core}} - \underline{1}\right)\underline{\tilde{S}}^{\mathrm{LR}}\left(\underline{S}^{\mathrm{core}} - \underline{1}\right)\underline{\tilde{S}}^{\mathrm{LR}} + \cdots\Big)\vec{d}^{\dagger}.\end{aligned} \tag{6.17}$$

This form of the cross section is again a power series, and takes the cancellation in hydrogen between the core-scattered orbits and the ghost orbits into account at all orders. A number of features of this formula are worth noting. First, for hydrogen ($\underline{S}^{\mathrm{core}} = \underline{1}$), the cross section is simply,

$$\sigma^{\Delta w}(w) \sim \mathrm{Re}\vec{d}\left(\underline{1} + 2\underline{\tilde{S}}^{\mathrm{LR}}\right)\vec{d}^{\dagger}, \tag{6.18}$$

which reproduces the cross section of closed-orbit theory first derived by Du and Delos [38]. As in their approach, the repetitions of the primitive orbits are taken into account classically, by running each primitive closed orbit through classically the desired number of times. Of course, closed-orbit theory is not formulated in terms of scattering matrices, so some algebra is required to translate my result into their language.

Second, the higher order terms in the improved cross section, which vanish for hydrogen, show that the primitive closed orbits scatter into each other through the matrix $(\underline{S}^{\mathrm{core}} - \underline{1})$ rather than simply through the core region S-matrix as in the primitive approximation. This matrix also appears in the semiclassical approximations of Dando *et al.* [53] and of Shaw and Robicheaux [54]. In fact, on the surface, my semiclassical approximation seems to give the same result as their extensions of closed orbit theory to nonhydrogenic atoms. I have emphasized previously that the extensions of closed orbit theory diverge for atoms having two or more large quantum defects. The main difference in my semiclassical

S-matrix theory for the cross section is that these divergences can be handled in simple and elegant manner.

The main advance of the semiclassical approximation derived here, Eq. (6.17), is that it can be resummed analytically to include all orders of core-scattering automatically. The series, Eq. (6.17), is simply a geometric series that can be written in the compact form,

$$\sigma^{\Delta w}(w) \sim \mathrm{Re}\vec{d}\left(\underline{1} + 2\underline{S}^{\mathrm{core}}\underline{\tilde{S}}^{\mathrm{LR}}\left[\underline{1} - (\underline{S}^{\mathrm{core}} - \underline{1})\,\underline{\tilde{S}}^{\mathrm{LR}}\right]^{-1}\right)\vec{d}^{\dagger}. \tag{6.19}$$

This, along with the semiclassical formulas for the long-range S-matrix constitute the main result of this thesis. I will refer to this as the **resummed semiclassical approximation**. This formula represents a semiclassical method of calculating both the w domain and recurrence spectra of nonhydrogenic atoms in an external magnetic or electric field. This result shows that there is no need to use multiple scattering expansions of the cross section in conjunction with semiclassical approximations. Before applying this formula to treat a number of diamagnetic atoms it is useful to discuss the convergence properties of this improved semiclassical approximation.

The closed form of the cross section, Eq. (6.19), was derived by rearranging the power series expansion of the cross section, Eq. (6.1), canceling the ghost and core-scattered orbits, and then re-summing the resulting series. The initial form of the result, Eq. (6.17), is a power series in the matrix $(\underline{S}^{\mathrm{core}} - \underline{1})\,\underline{\tilde{S}}^{\mathrm{LR}}$. Because this power series is just the geometric series, it will converge when the following condition is met:

$$\kappa \equiv \left|(\underline{S}^{\mathrm{core}} - \underline{1})\,\underline{\tilde{S}}^{\mathrm{LR}}\right| < 1. \tag{6.20}$$

This matrix norm is defined in Eq. (3.32) and can be calculated simply as the largest eigenvalue of the matrix $(\underline{S}^{\mathrm{core}} - \underline{1})\,\underline{\tilde{S}}^{\mathrm{LR}}$. However, I emphasize, that even when the power series of the improved cross section, Eq. (6.17), does not converge, the resummed semiclassical cross section, Eq. (6.13), can be used to obtain "reasonable" finite predictions.

There are two critical parameters that affect the success of the improved semiclassical cross section. These parameters are the scaled field w, and the smoothing width Δw. Both of these parameters can be used to decrease the convergence factor κ and thus improve the convergence properties of the

semiclassical approach. First, the scaled field w is important because the semiclassical S-matrix $\underline{S}^{\rm LR}(w)$ is proportional to $1/\sqrt{w}$ (or $1/w$ for the parallel orbit). Thus, at larger values of w the semiclassical method is expected to give better results. This makes perfect sense, as the quantity $2\pi/w$ acts like as an effective $\hbar$ in the Schrödinger equation. So higher values of w correspond to physics that is more classical. The importance of using high values of w to obtain good semiclassical results has been noted by other researchers. In particular, Dando *et al.* [53] claim that this factor in the core-scattered terms of the cross section should be sufficient to converge the expansion of the semiclassical expansion of the cross section. Unfortunately, this has not been the case - when multiple quantum defects are turned on, simply having high values of w does not seem to be enough to cause the semiclassical expansions to converge.

The preconvolution approach to the cross section shows why high values of w are not necessarily sufficient to get a convergent semiclassical cross section for nonhydrogenic atoms. The main difficulty is that core-scattering introduces infinitely many long scaled actions into the theory. Even when core scattering is not present, it is well known that there are infinitely many closed orbits in a chaotic system. The difficulty of summing over an infinite number of orbits also occurs in the semiclassical trace formula. In that case, the exponential growth in the number of orbits causes the trace formula to be formally divergent. This divergence of the trace formula has been dealt with using either complicated resummation techniques or by convolving the trace formula with a smoothing function [24]. The situation for diamagnetic atoms other than hydrogen is actually much worse because the infinitely many closed orbits are all coupled into each other by the ionic core. Thus, yet another infinite set of long action orbits must be dealt with when quantum defects are turned on.

The key to resolving this dilemma is as follows: the formula that I have derived is meant, from the beginning, to give the cross section convolved over some width Δw. Thus, it is inappropriate to expect the semiclassical cross section, Eq. (6.19), to give reasonable results for $\Delta w = 0$. As Ch. 5 shows, the effect of the smoothing on the semiclassical S-matrix is to to introduce a damping factor $\exp(-\tilde{S}_p \Delta w/2)$ into the long-range S-matrix. As the following results demonstrate, this factor takes care of the convergence problems associated with the proliferation of long scaled action orbits in nonhy-

drogenic atoms.

6.3.2 Application to diamagnetic hydrogen

First, I present results for the case of diamagnetic hydrogen. In these results, the resummed semiclassical cross section, Eq. (6.19), is compared with accurate quantum calculations. Results for both the recurrence spectrum (Fig. 6.6) and the w-domain cross section $\sigma(w)$ (Fig. 6.7) are given. The dipole vectors $\vec{d}$ needed for the cross section are given by analytical formulas in [38]. The initial state $2p, m = 0$ has been excited by linearly polarized laser light to even parity, $m = 0$ final states. The recurrence spectra in Fig. 6.6 are shown at three different scaled energies ($\epsilon = -0.3, -0.5, -0.7$). The semiclassical calculations predict both the positions and amplitudes of the recurrence peaks to within a few percent in most cases. Larger discrepancies are seen near bifurcations and for lower scaled energies ($\epsilon = -0.7$) where the classical dynamics are mostly regular. Then, the stationary phase approximations used to obtain the semiclassical S-matrix begin to break down. Thus, in general, the predictions of the semiclassical approach improve at higher scaled energies.

While most of the features in the recurrence spectrum are insensitive to constant phase factors, such as the Maslov index μ in the semiclassical S-matrix, the w-domain cross section is sensitive to such phases. The good agreement seen in Fig. 6.7 in both the positions and amplitudes of the absorption peaks in the cross section $\sigma(w)$ demonstrates that the semiclassical phases have been treated correctly. The cross section $\sigma(w)$, as well as the recurrence spectra, is important to calculate, because divergences of the semiclassical approach are much more dramatic in $\sigma(w)$ than in the recurrence strength.

6.3.3 Diamagnetic lithium-like atom

Next, a lithium-like atom is treated. Figures 6.8, 6.9, and 6.10 give a sampling of semiclassical results for this atom that has a single large nonzero quantum defect ($\mu_s = 0.4$). All of these calculations are for even parity $m = 0$ final states at a scaled energy of $\epsilon = -0.3$. The dipole vector $\vec{d}$ from the $2p, m = 0$ initial state has been approximated by that of hydrogen [38].

First, Figs. 6.8 and 6.9 show the improved semiclassical cross section $\sigma(w)$ as a function of the

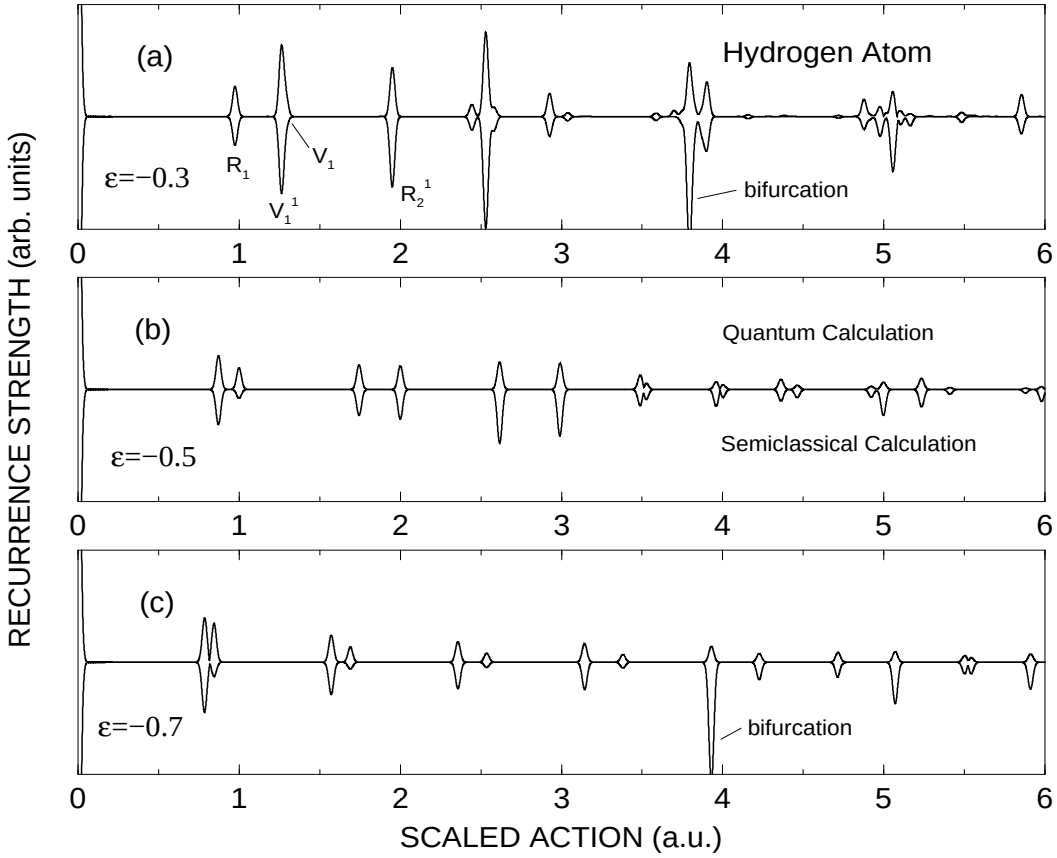

Figure 6.6: The quantum (upright) and semiclassical (inverted) recurrence spectra for diamagnetic hydrogen is plotted at three scaled energies ($\epsilon = -0.7, -0.5, -0.3$). The resummed semiclassical cross section, Eq. (6.19) along with the semiclassical long-range S-matrix of Ch. 5 has been used in the semiclassical calculation. The semiclassical results are shown along with accurate quantum calculations described in Ch. 4. In both cases, a preconvolution width of $\Delta w = 0.4$ has been used. The recurrence strengths have been obtained by Fourier transforming the cross section in the interval $w = 100 - 500$. The results are for even parity, $m = 0$ final states and an initial state of $2p, m = 0$. The agreement seen here is similar to what closed-orbit theory gives for hydrogen. The biggest discrepancies occur near the bifurcations of the closed orbits, where the primitive semiclassical S-matrix diverges.

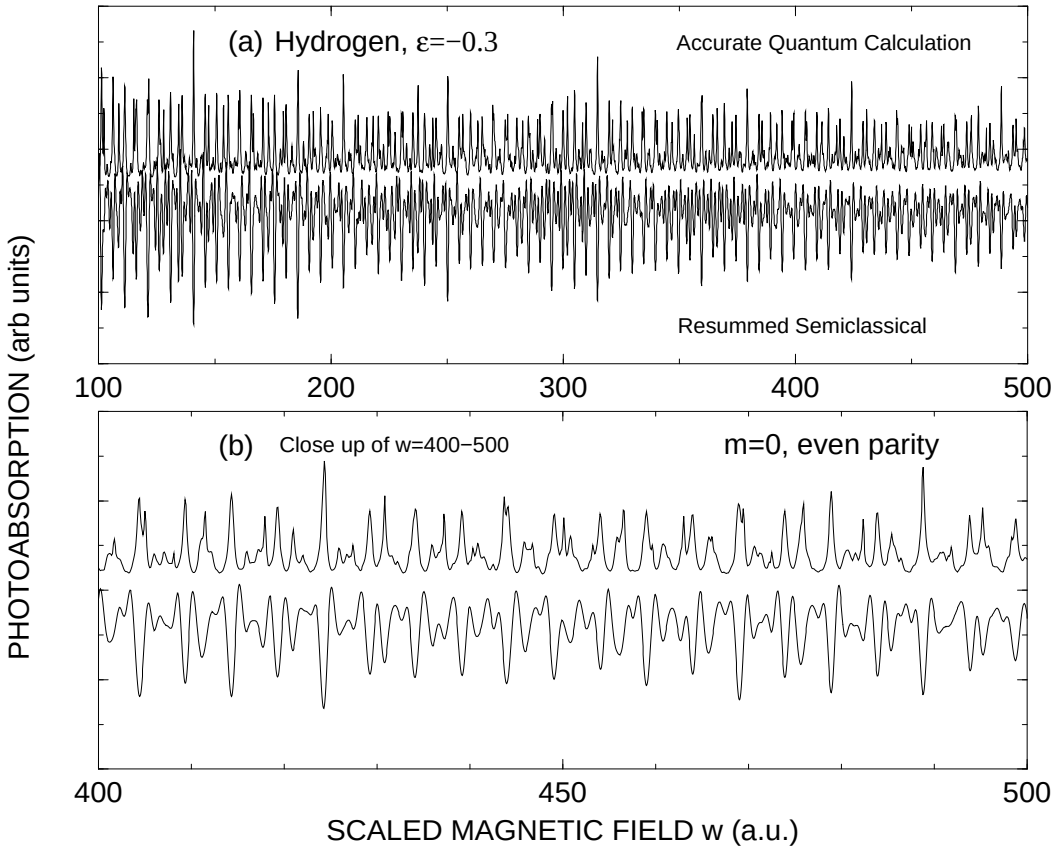

Figure 6.7: The photoabsorption cross section $\sigma(w)$ for diamagnetic hydrogen is shown at a scaled energy $\epsilon = -0.3$ as a function of the scaled field w. Again, a preconvolution width of $\Delta w = 0.4$ is used in the calculations. (a) Accurate quantum calculations (upright) are compared with the resummed semiclassical cross section (inverted), Eq. (6.19), over the range $w = 100 - 500$. (b) A close up of the range $w = 400 - 500$ shows more detail. Excellent agreement is seen between the quantum and semiclassical approaches. This complements the recurrence spectra for hydrogen presented in Fig. 6.6. Even parity, $m = 0$ final states are shown.

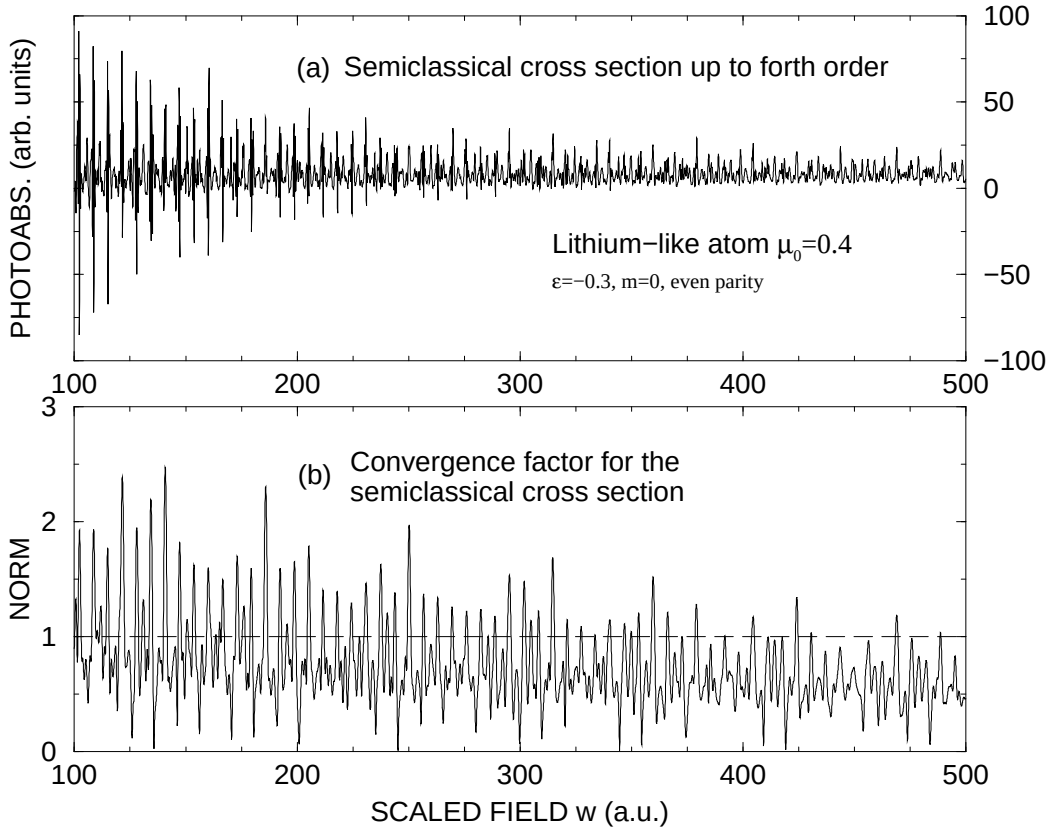

Figure 6.8: The semiclassical cross section $\sigma(w)$, Eq. (6.17), is shown along with the convergence factor κ, Eq. (6.20), for a lithium-like atom ($\mu_s = 0.4$) over the range $w = 100 - 500$. A scaled energy of $\epsilon = -0.3$ and even parity, $m = 0$ states are shown. (a) The semiclassical cross section has been constructed using the first four terms of the expansion of the improved semiclassical approximation, Eq. (6.17). The cross section is seen to be have unphysical negative values at low values of w. A smoothing width of $\Delta w = 0.6$ has been used, but at the lower values of w the cross section still does not converge. (b) The convergence factor κ, Eq. (6.20), which determines the convergence of the semiclassical cross section. When this factor reaches above unity (shown as a horizontal line), the semiclassical cross section becomes unphysical.

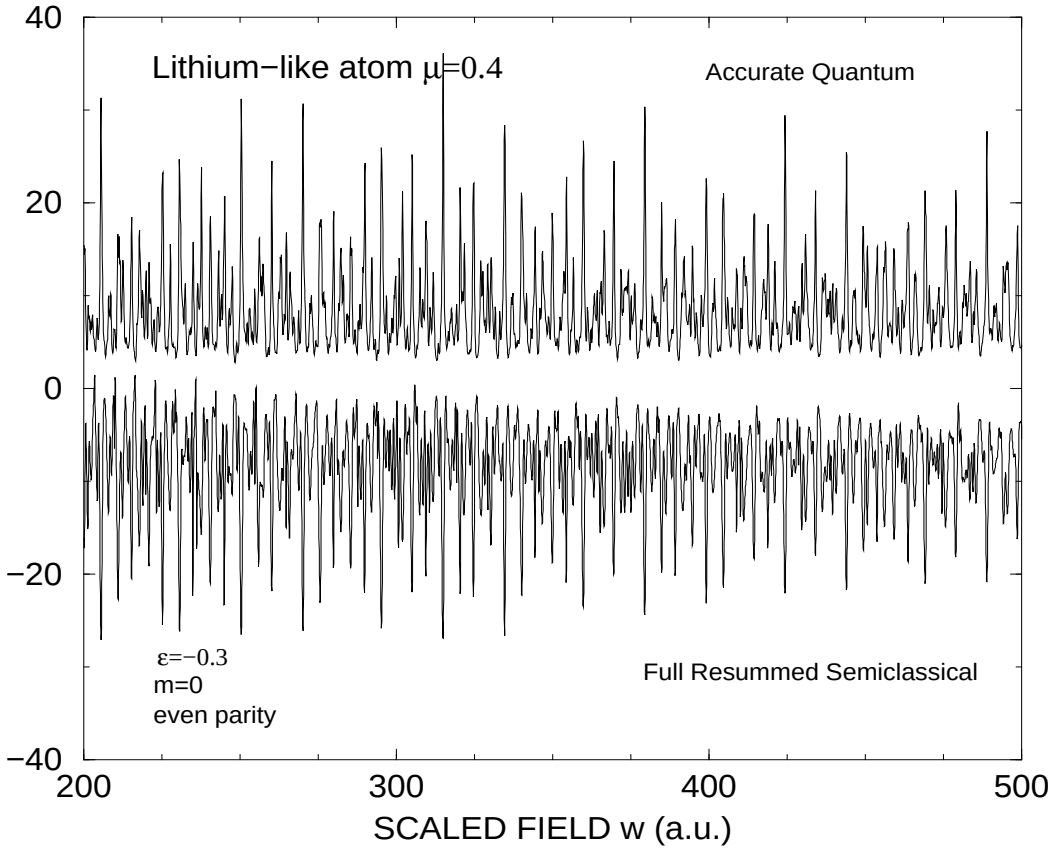

Figure 6.9: A comparison is shown between the improved semiclassical (inverted) cross section, Eq. (6.19), and an accurate quantum calculation for $m = 0$, even parity final states of a lithium-like atom ($\mu_s = 0.4$). All of the parameters ($\epsilon = -0.3, \Delta w = 0.6$) are the same as in Fig. 6.8, except that the closed form expression for the semiclassical cross section, Eq. (6.19), is used here. By calculating the matrix inverse in this equation, many of the unphysical features in the series expansion of the semiclassical cross section are repaired. I emphasize that without the preconvolution damping factor of $\exp(-\tilde{S}\Delta w/2)$ in the semiclassical S-matrix, the semiclassical result would show poor agreement with the quantum calculations.

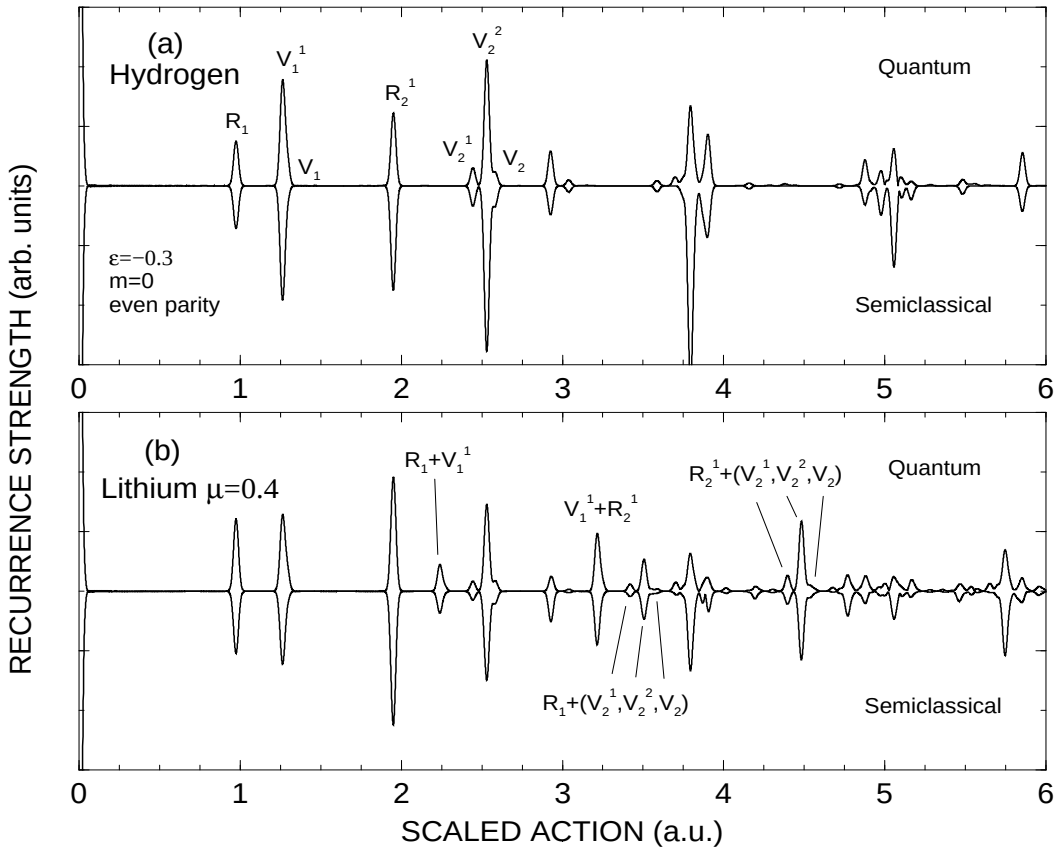

Figure 6.10: The quantum (upright) and semiclassical (inverted) recurrence strength for H and Li of the total photoabsorption cross section $\sigma(w)$ is shown at a scaled energy of $\epsilon = -0.3$. (a) Diamagnetic hydrogen recurrence spectra for $m = 0$, even parity final states ($\Delta w = 0.6, w = 100 - 500$). (b) Diamagnetic lithium-like atom ($\mu_s = 0.4$), again for $m = 0$, even parity final states. The dipole vectors for hydrogen have been used to obtain the lithium spectrum. The hydrogen recurrence spectra is shown alongside the lithium spectra to highlight the core scattered peaks present in lithium. The semiclassical recurrence strength for both atoms is calculated using the closed form expression, Eq. (6.19), of the improved semiclassical theory. The primitive closed orbits of hydrogen ($R_1, V_1^1, V_1, \ldots$) are labeled in graph (a) and their properties can be found in Fig. B.2. New core-scattered recurrence peaks are seen in the lithium case (b) due to the nonzero quantum defect. These peaks are combinations of the primitive closed orbits of hydrogen and are labeled according to which orbits have combined ($R_1 + V_1^1, V_1^1 + R_2^1, \ldots$) to give the new peak.

scaled magnetic field w. In both of these figures, a smoothing width of $\Delta w = 0.6$ has been used. The only difference between the semiclassical calculations in these two figures is that in the first figure (Fig. 6.8), the power series expansion of the improved cross section, Eq. (6.17), is used, including only the first four terms in the expansion. The slow convergence of the series is seen in the negative cross section and sharp spikes in the cross section (panel (a)). Panel (b) of that figure elucidates why the series expansion appears to not be converging for the values of w and $\Delta w = 0.6$ used here. The convergence factor κ, Eq. (6.20), is plotted as a function of w in panel (b). Because its value is greater than unity at low values of w, the series form of the improved semiclassical cross section, Eq. (6.17), cannot be expected to converge.

The second figure in this series, Fig. 6.9, uses the full resummed semiclassical theory, Eq. (6.19), rather than its series form. All of the divergence problems are seen to be completely eliminated, and good agreement between the quantum and semiclassical calculations is achieved. The corresponding recurrence spectrum for this case is shown in Fig. 6.10 and again exhibits excellent agreement with the accurate quantum calculations. Both the positions and amplitudes of the core scattered recurrences are predicted by the resummed semiclassical theory to within a few percent.

These examples show that the resummed semiclassical theory can be used to give quantitative predictions of the spectra of diamagnetic atoms other than hydrogen; both the recurrence spectrum and "energy" domain cross section $\sigma(w)$ show no signs of divergences when the resummed version of the theory is used. While Dando *et al.* [53] have given similar recurrence spectra for this case, no semiclassical calculations of the w-domain cross section $\sigma(w)$ have been reported previously. Most likely, their theory would give poor results for $\sigma(w)$ as no preconvolution or resummation of the theory has been performed. Next, I apply the semiclassical theory to a slightly more complex atom: rubidium.

6.3.4 Diamagnetic rubidium atom

One of the greatest challenges for closed orbit theory has been its extension to atoms other than hydrogen. I have given descriptions of how the basic form of closed-orbit theory has been applied to very light atoms such as helium and lithium. While these extensions give good results (at least for the

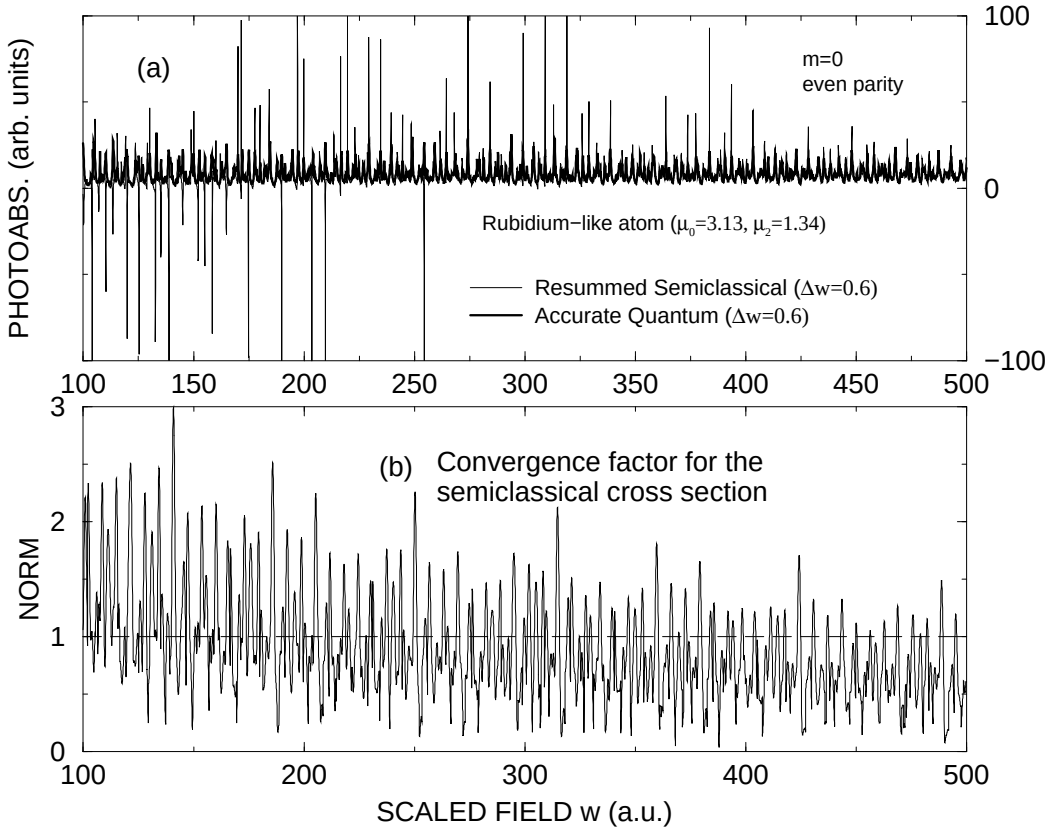

Figure 6.11: The scaled variable photoabsorption cross section $\sigma(w)$ is shown for $m = 0$, even parity states of a diamagnetic rubidium-like atom ($\mu_s = 3.13, \mu_d = 1.34$). For simplicity, the dipole vectors for hydrogen have been used to calculate these results. A scaled energy of $\epsilon = -0.3$ and smoothing width of $\Delta w = 0.6$ is used. (a) An accurate quantum calculation (thick line) is shown on top of the resummed semiclassical cross section (thin line), Eq. (6.19). As expected, the predictions of the semiclassical formula improve as w is increased, but at low values of w (100-250) the semiclassical result shows an unphysical negative valued cross section. At intermediate w (250-400), the negative cross section is not present, but sharp spikes in the semiclassical result are still seen. Above $w > 400$, the semiclassical result is beginning to converge to the quantum result. (b) The semiclassical convergence factor κ over the same range of w. At low values of w this factor is greater than unity (dashed line), so the semiclassical cross section (a) gives poor results.

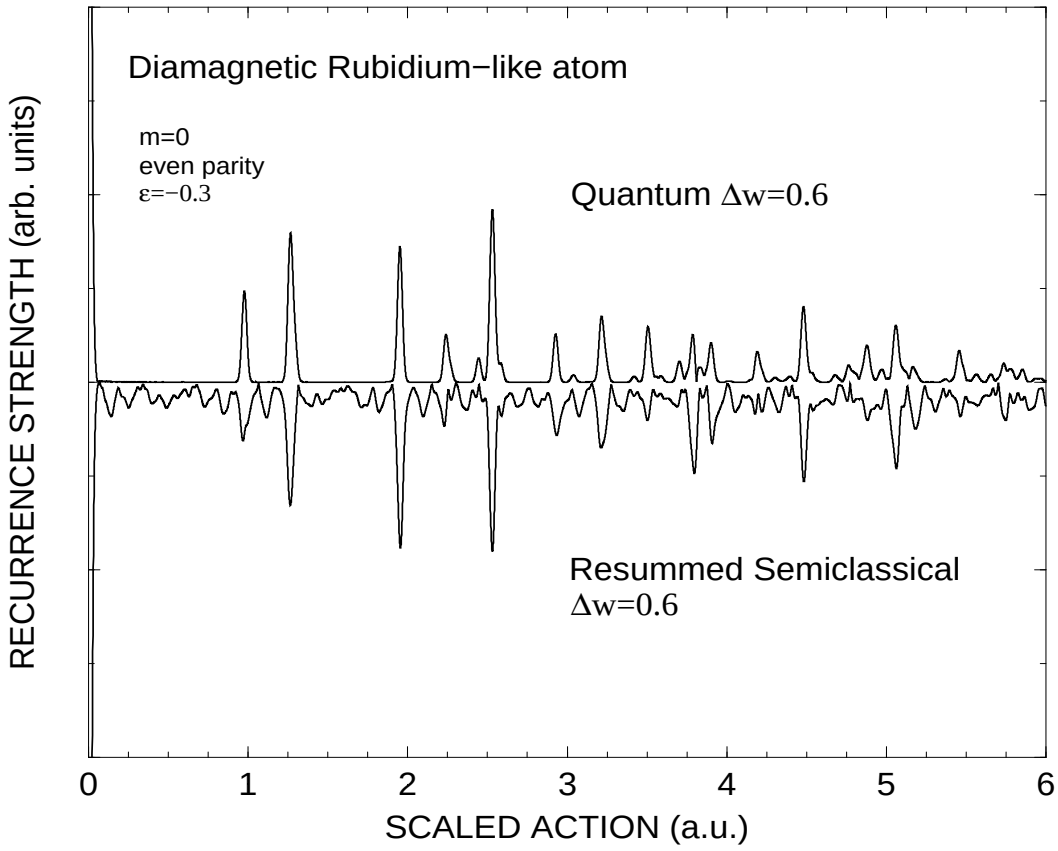

Figure 6.12: The quantum (upright) and semiclassical (inverted) recurrence strength is given of the scaled photoabsorption spectrum shown in Fig. 6.11. The sharp spikes and negative values cross section of the semiclassical cross section in Fig. 6.11 show up as noise in the semiclassical recurrence spectra. Even parity, $m = 0$ states of diamagnetic rubidium are shown at a scaled energy of $\epsilon = -0.3$ and a smoothing width of $\Delta w = 0.6$. This figure, along with Fig. 6.11, illustrates the convergence problems found in the semiclassical approach when more than one quantum defect is appreciable and the smoothing width is not sufficiently large.

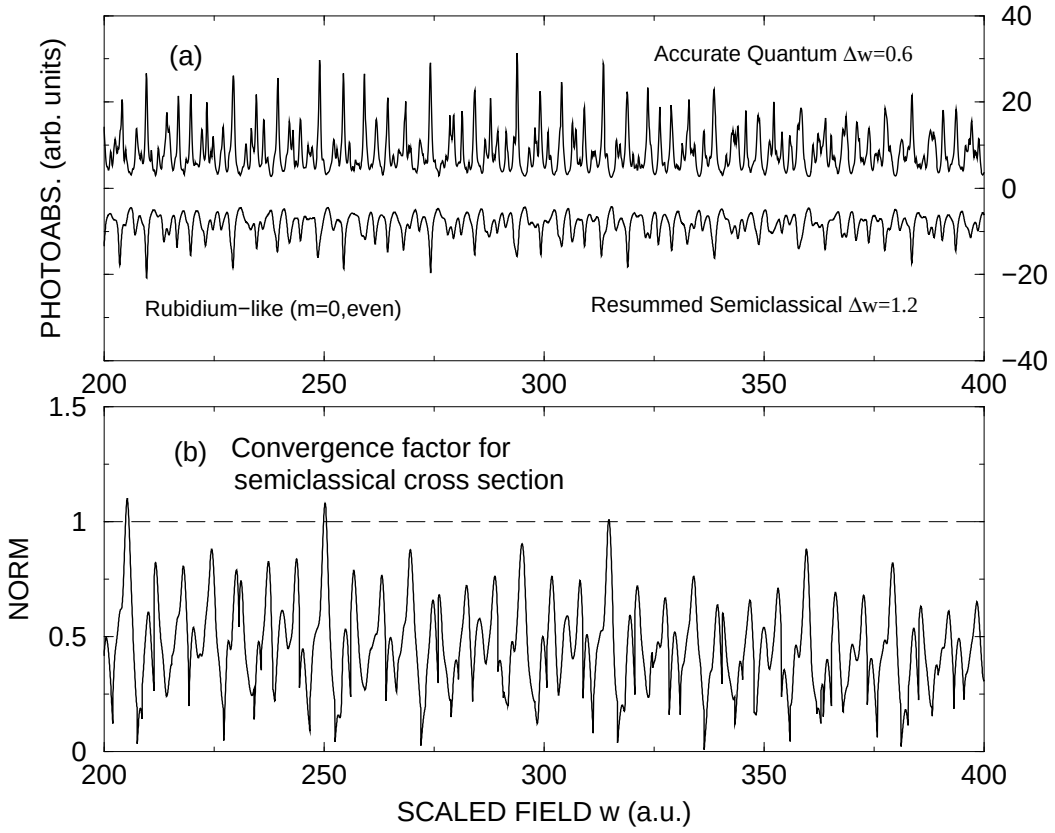

Figure 6.13: The scaled variable photoabsorption cross section $\sigma(w)$ of diamagnetic rubidium is plotted at a scaled energy of $\epsilon = -0.3$ ($m = 0$, even parity). (a) Accurate quantum result (upright, $\Delta w = 0.6$) is compared with the resummed semiclassical formula (inverted), Eq. (6.19). The smoothing width in the semiclassical calculation has been increased to $\Delta w = 1.2$ to improve the convergence of the semiclassical result compared to that of Fig. 6.11. This smoothing width is more than sufficient to eliminate the negative valued cross section (remember the semiclassical is shown inverted) and large spikes seen in the semiclassical cross section with a smaller smoothing width of $\Delta w = 0.6$. (b) The semiclassical convergence factor κ is less than unity over this range of w (200-400) confirming that the semiclassical cross section should give good results at this smoothing width.

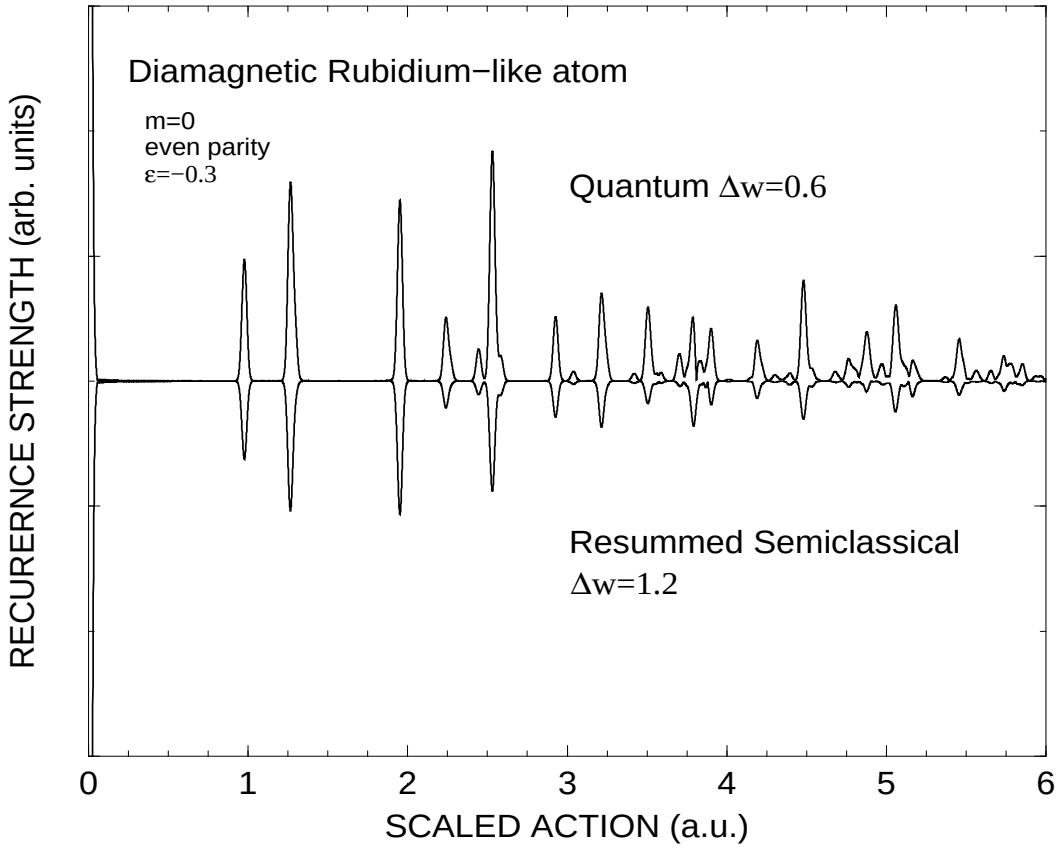

Figure 6.14: The recurrence strength of the scaled variable cross section $\sigma(w)$ shown in Fig. 6.13 is plotted. The accurate quantum (upright) recurrence strength ($\Delta w = 0.6$) is shown along with the resummed semiclassical result (inverted, $\Delta w = 1.2$), Eq. (6.19), at a scaled energy of $\epsilon = -0.3$. These calculations are for even parity, $m = 0$ states of rubidium. The only difference between these results and those of Fig. 6.12 is the larger smoothing width used in the semiclassical calculations. Increasing the smoothing width provides a convenient, yet physically grounded way of improving the predictions of the semiclassical result.

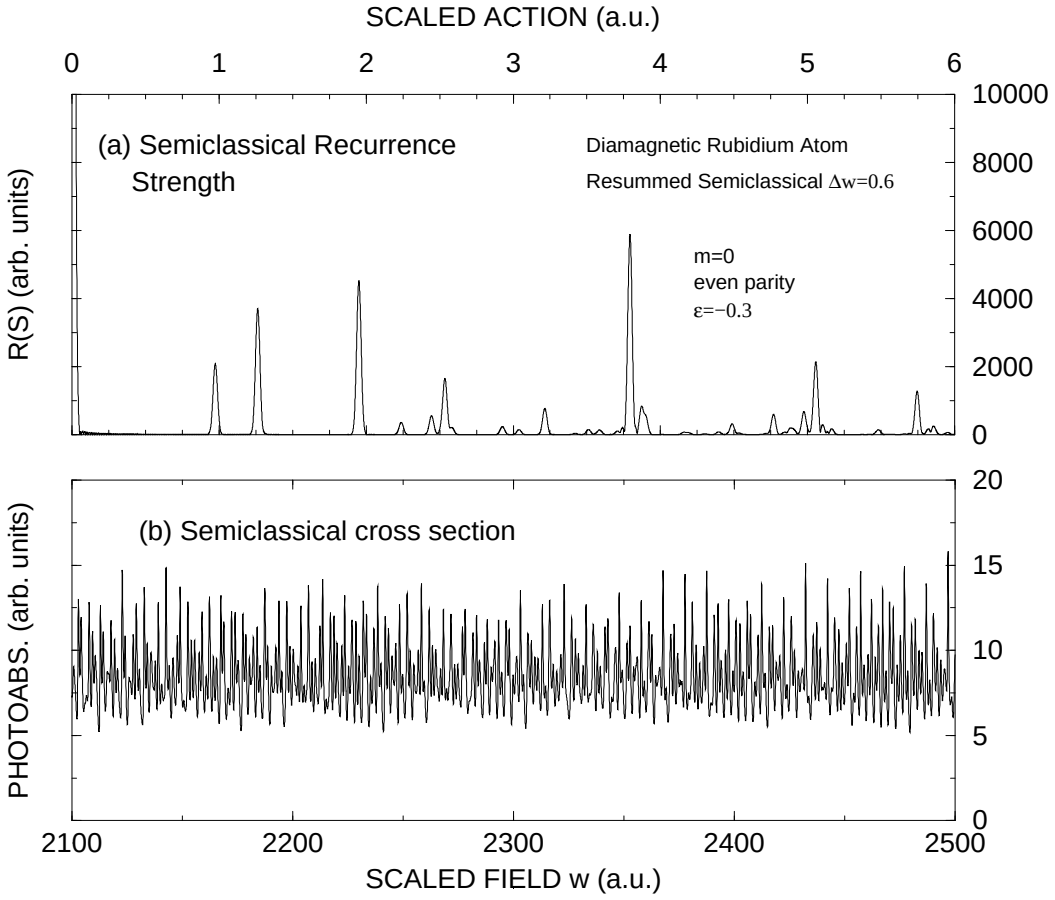

Figure 6.15: A resummed semiclassical calculation is given for rubidium at a relatively high value of $w = 2100 - 2500$, where no quantum calculations are available. At these values of w, a small smoothing width of $\Delta w = 0.6$ is sufficient to converge the semiclassical result. (a) Semiclassical recurrence strength of the total cross section $\sigma(w)$ (b) Total photoabsorption cross section as a function of w. Again, even parity, $m = 0$ states are shown at a scaled energy of $\epsilon = -0.3$.

recurrence strength) in these cases, no such success has been achieved for heavier atoms. In this section I report the first semiclassical treatment of the spectrum of diamagnetic rubidium.

For the calculations presented in this subsection, the following parameters are used. First, even parity $m = 0$ states of rubidium are treated, so that the relevant quantum defects are ($\mu_s = 3.13, \mu_d = 1.34$). Results for a single scaled energy of $\epsilon = -0.3$ are presented. The relevant closed orbits for this case are summarized in Appendix B. To simplify the calculations, the dipole vectors $\vec{d}$ for hydrogen have again been used [38].

As discussed above, there are two factors that determine the convergence of the improved semiclassical theory of this chapter. In general, the theory is expected to give good results at large values of w and for moderate smoothing widths Δw. In this case, the critical convergence factor κ is expected to be less than unity, indicating the convergence of the geometric series.

First, I show results of the photoabsorption cross section $\sigma(w)$ for low values of both w and Δw in Fig. 6.11. Here, the resummed semiclassical theory is shown (thin line) overlayed by the accurate quantum calculation (thick line). At the smoothing width used here $\Delta w = 0.6$, the semiclassical theory shows dramatic signs of divergence problems. The plot of the convergence factor κ confirms these problems as its value is greater than unity. The signatures of the divergence of the semiclassical theory in the recurrence spectrum are shown in Fig. 6.12. While many of the recurrence peaks predicted by the semiclassical theory are in good agreement with the quantum calculations there is a large amount of "noise" in the semiclassical recurrence spectra.

The next series of figures (Figs. 6.13, 6.14, and 6.15) shows that these divergence problems can be eliminated simply by increasing either the range of w used, or by increasing the smoothing width Δw. I emphasize that increasing these parameters is not an artificial construct used to get the semiclassical theory to work. Rather, this treatment is motivated by the correct understanding of the preconvolved semiclassical theory.

First, in Fig. 6.13, the scaled photoabsorption cross section $\sigma(w)$ is presented at low values of $w = 100 - 500$, but for a large convolution width of $\Delta w = 1.2$. Immediately, it is seen that the resummed semiclassical theory, based on Eq. (6.19), which was used to obtain this result, gives a

positive cross section that shows none of the unphysical features seen when a smaller value of Δw is used. In addition, the convergence factor κ is seen to be well below unity for this range of w. While the heights of the semiclassical absorption peaks are somewhat smaller than the quantum result, this is expected since the quantum calculations were performed at a smaller smoothing width ($\Delta w = 0.6$). In spite of this, the basic features in the cross section are present in both the quantum and semiclassical calculation. The corresponding Fourier transform, or recurrence strength, of this spectra is shown in Fig. 6.14. Again, while the semiclassical recurrence peaks are somewhat smaller than the quantum, the agreement is generally very good; no unphysical noise is seen is the resummed semiclassical results.

Finally, I show that simply increasing the value of w used can also improve the convergence of the semiclassical theory. This simply corresponds to decreasing the effective $\hbar$ in the Schrödinger equation (see Appendix A). Figure 6.15 gives both the w-domain cross section $\sigma(w)$ (a) and the recurrence strength (b) for diamagnetic rubidium at smoothing width of $\Delta w = 0.6$. The range of w used is much larger ($w = 2100 - 2500$) than previously used. The resummed semiclassical theory has been used to obtain these results. At this time, no accurate quantum calculations for this range of w have been performed for any atom. The important point of this figure is that the resummed semiclassical theory is completely convergent.

6.4 Conclusion

This chapter has used the tools of this thesis, namely the S-matrices and the preconvolved photoabsorption cross section, to develop a convergent semiclassical theory for the photoabsorption spectra of atoms in external magnetic fields. The main result, is a resummed semiclassical theoretical formula, Eq. (6.19), for nonhydrogenic atoms. An interesting relationship between core-scattered orbits and ghost orbits was uncovered. This enabled the primitive semiclassical theory to be improved through a rearrangement of the expansion of the cross section. While the path taken to get this result has been circuitous, the final result has a simple form. Indeed, given the subtleties found along the way, it is no surprise that a convergent semiclassical theory for nonhydrogenic atoms has not been given previously.

The main advance of this thesis, which enabled the semiclassical theory to be derived, has been

the use of S-matrices to describe the motion of the electron. I have shown that the S-matrices, along with the preconvolved photoabsorption cross section, form a complete and powerful framework for understanding atoms in external fields. While the final result is a semiclassical theory, this development has depended critically on the use of accurate quantum mechanical S-matrices. Without the accurate quantum calculations, the surprising cancellation effect between ghost and core-scattered orbits could not have been detected, and the semiclassical theory would have remained in a sad and incomplete state.

From this point, there are many directions to proceed. First, it is desirable to find experimental tests of this theory. Recently, experimental results have been reported for the heavier atoms barium [66] and argon [67] in an external electric field. Tests such as these would provide an excellent test of the semiclassical theory developed in this dissertation. Second, the success of semiclassical methods for general systems hinges strongly on the development of an accurate treatment of bifurcations. While I have given a basic outline for incorporating their effects into this theory, a more thorough investigation is in order. A question that is intimately related to the treatment of bifurcations is the prediction of ghost orbits. Hopefully, a more thorough understanding of bifurcations will show **why** the core-scattered orbits and ghost orbits always cancel each other in hydrogen.

Accurate quantum calculations could also be improved, particularly above the ionization threshold. To date, only a few calculations of atoms in external magnetic fields have been performed in this regime where the electron can escape to infinity. It would be very interesting to include the additional time scales present in a multichannel atom with more than one ionization threshold. The scattering matrices developed in this thesis should provide an efficient way of performing and interpreting such calculations. It would also be of interest to study other systems in atomic physics, such as two electron escape from helium, using the methods developed in these chapters.

My hope is that the reader of this thesis has been able to see through all of the complicated derivations to the underlying physical concepts. It is these concepts, rather than the derivations that have made this work a pleasure to develop and write. Of course, a rigorous mathematical treatment is necessary - but it is not sufficient to provide insight into complex physical systems.

Bibliography

[1] J. J. Sakurai, in Modern quantum mechanics, edited by San Fu Taun (Addison-Wesley, New York, 1994).

[2] A. Einstein, Verh. Dtsch. Ges. **19**, 82 (1917).

[3] M. V. Berry and K. E. Mount, Rep. Prog. Phys. **35**, 315 (1972).

[4] L. Brillouin, J. Phys. Radium **7**, 353 (1926).

[5] J. B. Keller, Ann. Phys. **4**, 180 (1958).

[6] I. C. Percival, Adv. Chem. Phys. **36**, 1 (1977).

[7] H. Poincare, Les Methodes Nouvelles de la Mechanique Celeste (Gauthier-Villars, Paris, 1892).

[8] A. N. Kolmogorov, Dokl. Akad. Nauk. SSSR **98**, 527 (1954).

[9] V. I. Arnol'd, Russ. Math. Survey **18**, 85 (1963).

[10] V. I. Arnol'd, Russ. Math. Survey **18**, 9 (1963).

[11] J. Moser, Nachr. Akad. Wiss. Gottingen II, Math. Phys. Kd **1**, 1 (1968).

[12] A. J. Lichtenberg and M. A. Lieberman, Regular and Chaotic Dynamics, Vol. 38 of Applied Mathematical Sciences, 2nd ed. (Springer-Verlag, New York, 1983).

[13] E. N. Lorenz, J. Atmos. Sci. **20**, 130 (1963).

[14] R. Balian and C. Bloch, Ann. Phys. **60**, 401 (1970).

[15] R. Balian and C. Bloch, Ann. Phys. **64**, 271 (1971).

[16] R. Balian and C. Bloch, Ann. Phys. **69**, 76 (1972).

[17] R. Balian and C. Bloch, Ann. Phys. **85**, 514 (1974).

[18] M. C. Gutzwiller, J. Math Phys. **8**, 1979 (1967).

[19] M. C. Gutzwiller, J. Math Phys. **10**, 1004 (1969).

[20] M. C. Gutzwiller, J. Math Phys. **11**, 1791 (1970).

[21] M. C. Gutzwiller, J. Math Phys. **12**, 343 (1971).

[22] M. C. Gutzwiller, Chaos in Classical and Quantum Mechanics (Springer-Verlag, New York, 1990).

[23] L. E. Reichl, The Transition to Chaos in Conservative Classical Systems: Quantum Manifestations (Springer-Verlag, New York, 1992).

[24] M. Brack and R. K. Bhaduri, Semiclassical Physics (Addison-Wesley, Reading, Massachusetts, 1997).

[25] M. V. Berry and M. Tabor, Proc. R. Soc. Lond. A. **349**, 101 (1976).

[26] M. V. Berry and M. Tabor, J. Phys. A **10**, 371 (1977).

[27] W. R. S. Garton and F. S. Tomkins, Astrophys. J. **158**, 839 (1969).

[28] K. T. Lu, F. S. Tomkins, and W. R. S. Garton, Proc. R. Soc. London, Sect. A **364**, 421 (1978).

[29] K. T. Lu, F. S. Tomkins, H. M. Crosswhite, and H. Crosswhite, Phys. Rev. Lett. **41**, 1034 (1978).

[30] A. R. Edmonds, Journale de Physique **31**, 71 (1970).

[31] A. F. Starace, J. Phys B **6**, 585 (1973).

[32] C. Iu *et al.*, Phys. Rev. Lett. **66**, 145 (1991).

[33] A. Holle *et al.*, Phys. Rev. Lett. **56**, 2596 (1986).

[34] J. Main, G. Wiebusch, A. Holle, and K. H. Welge, Phys. Rev. Lett. **57**, 2789 (1986).

[35] A. Holle *et al.*, Phys. Rev. Lett. **61**, 161 (1988).

[36] E. B. Bogomolny, Sov. Phys. JETP **69**, 275 (1989).

[37] M. L. Du and J. B. Delos, Phys. Rev. A **38**, 1896 (1988).

[38] M. L. Du and J. B. Delos, Phys. Rev. A **38**, 1913 (1988).

[39] J. Main *et al.*, Phys. Rev. A **49**, 847 (1994).

[40] M. Courtney and D. Kleppner, Phys. Rev. A **53**, 178 (1996).

[41] T. van der Veldt W. Vassen and W. Hogervorst, J. Phys. B **25**, 3295 (1992).

[42] T. van der Veldt, W. Vassen, and W. Hogervorst, Europhys. Lett. **21**, 903 (1993).

[43] K. Karremans, W. Vassen, and W. Hogervorst, Phys. Rev. Lett. **81**, 4843 (1998).

[44] K. Karremans, W. Vassen, and W. Hogervorst, Phys. Rev. A **60**, 2275 (1999).

[45] K. Karremans, W. Vassen, and W. Hogervorst, Phys. Rev. A **60**, 4764 (1999).

[46] M. Courtney, H. Jiao, N. Spellmeyer, and D. Kleppner, Phys. Rev. Lett. **73**, 1340 (1994).

[47] M. Courtney *et al.*, Phys. Rev. Lett. **74**, 1538 (1995).

[48] M. Courtney, N. Spellmeyer, H. Jiao, and D. Kleppner, Phys. Rev. A **51**, 3604 (1995).

[49] A. Kips, W. Vassen, and W. Hogervorst, Phys. Rev. A **59**, 2948 (1999).

[50] M. J. Seaton, Rep. Prog. Phys. **46**, 167 (1983).

[51] J. Gao and J. B. Delos, Phys. Rev. A **46**, 1455 (1992).

[52] P. A. Dando, T. S. Monteiro, D. Delande, and K. T. Taylor, Phys. Rev. Lett. **74**, 1099 (1995).

[53] P. A. Dando, T. S. Monteiro, D. Delande, and K. T. Taylor, Phys. Rev. A **54**, 127 (1996).

[54] J. A. Shaw and F. Robicheaux, Phys. Rev. A **58**, 3561 (1998).

[55] B. Hupper, J. Main, and G. Wunner, Phys. Rev. A **53**, 744 (1996).

[56] A. Kips, W. Vassen, and W. Hogervorst, Phys. Rev. A **58**, 3043 (1998).

[57] A. M. Ozorio de Almeida and J. H. Hannay, J. Phys. A **20**, 5873 (1987).

[58] M. Sieber, J. Phys. A **29**, 4715 (1996).

[59] H. Schomerus and M. Sieber, J. Phys. A **30**, 4537 (1997).

[60] J. M. Mao and J. B. Delos, Phys. Rev. A **45**, 1746 (1992).

[61] D. A. Sadovskii and J. B. Delos, Phys. Rev. E **54**, 2033 (1996).

[62] J. Gao and J. B. Delos, Phy. Rev. A. **56**, 356 (1997).

[63] J. Main and G. Wunner, Phys. Rev. A **55**, 1743 (1997).

[64] G. J. Kuik, A. Kips, W. Vassen, and W. Hogervorst, J. Phys. B **29**, 2159 (1996).

[65] A. Kips, W. Vassen, and W. Hogervorst, J. Phys. B **33**, 109 (2000).

[66] K. A. Bates, J. J. Masae, C. Vasilescu, and D. Schumacher (unpublished).

[67] J. D. Wright, W. Huang, H. Flores-Rueda, and T. J. Morgan, in Bulletin of the American Physical Society (APS, Maryland, 2001), No. 3, p. 74, 2001.

[68] M. Aymar, C. H. Greene, and E. Luc-Koenig, Rev. Mod. Phys. **68**, 1015 (1996).

[69] C. W. Clark and K. T. Taylor, J. Phys. B **13**, L737 (1980).

[70] C. W. Clark and K. T. Taylor, J. Phys. B **15**, 1175 (1982).

[71] P. F. O'Mahony, Phys. Rev. Lett. **63**, 2653 (1989).

[72] P. F. O'Mahony and F. Mota-Furtado, Phys Rev. Lett. **67**, 2283 (1991).

[73] D. Delande, A. Bommier, and J. C. Gay, Phys. Rev. Lett. **66**, 141 (1991).

[74] S. Watanabe and H. Komine, Phys. Rev. Lett. **67**, 3227 (1991).

[75] D. Delande *et al.*, J. Phys. B **27**, 2771 (1994).

[76] M. H. Halley, D. Delande, and K. T. Taylor, J. Phys. B **26**, 1775 (1993).

[77] P. F. O'Mahony and K. T. Taylor, Phys. Rev. Lett. **57**, 2931 (1986).

[78] D. J. Armstrong and C. H. Greene, Phys. Rev. A **50**, 4956 (1994).

[79] F. Robicheaux, C. Wesdorp, and L. D. Noordam, Phys. Rev. A **60**, 1420 (1999).

[80] A. Nussenzweig, E. E. Eyler, T. Bergeman, and E. Pollack, Phys. Rev. A **41**, 4944 (1990).

[81] H. H. Fielding and T. P. Softley, Phys. Rev. A **49**, 969 (1994).

[82] F. Robicheaux and J. A. Shaw, Phys. Rev A **58**, 1043 (1998).

[83] D. A. Harmin, Phys. Rev. A **26**, 2656 (1982).

[84] U. Fano, Phys. Rev. A **24**, 619 (1981).

[85] M. J. Seaton, C. R. Acad. Sci **240**, 1317 (1955).

[86] M. J. Seaton, Mon. Not. R. Astron. Soc. **118**, 504 (1958).

[87] M. J. Seaton, Proc. Phys. Soc. London **88**, 801 (1966).

[88] M. J. Seaton, J. Phys. B **2**, 5 (1969).

[89] L. S. Rodberg and R. M. Thaler, Introduction to the Quantum Theory of Scattering, Vol. 26 of Pure and Applied Physics (Academic Press, New York, 1967).

[90] C. H. Greene, U. Fano, and G. Strinati, Phys. Rev. A **19**, 1485 (1979).

[91] C. H. Greene, A. R. P. Rau, and U. Fano, Phys. Rev. A **26**, 2441 (1982).

[92] H. A. Bethe and E. E. Salpeter, Quantum mechanics of one- and two-electron atoms (Plenum, New York, 1977).

[93] Handbook of mathematical Functions, edited by M. Abramowitz and I. Stegun (U. S. Department of Commerce, Washinton D. C., 1964), Vol. AMS-55.

[94] F. S. Ham, in Solid State Physics, edited by F. Seitz and D. Turnbull (Academic, New York, 1955), p. 127.

[95] R. J. Rydberg, K. Svenska Vetensk. Akad. Handl. **23**, 11 (1189).

[96] H. Friedrich, Theoretical atomic physics, 2nd. ed. (Springer-Verlag, New York, 1998).

[97] E. B. Bogomolny, Nonlinearity **5**, 805 (1992).

[98] A. M. Ozorio de Almeida, J. Phys. A **27**, 2891 (1994).

[99] T. Prosen, J. Phys. A **28**, 4133 (1995).

[100] C. Rouvinez and U. Smilansky, J. Phys A. **28**, 77 (1995).

[101] A. Selberg, J. Indian Math. Soc. **20**, 47 (1956).

[102] M. V. Berry and J. P. Keating, J. Phys. A **23**, 4839 (1990).

[103] H. M. Edwards, Riemann's zeta function (Academic Press, New York, 1974).

[104] F. T. Smith, Phys. Rev. **118**, 349 (1960).

[105] F. Robicheaux, Phys. Rev. A **48**, 4162 (1993).

[106] P. Labastie and G. Jalbert, Phys. Rev. A **46**, 2581 (1992).

[107] P. M. Morse and H. Feshbach, Methods of Theoretical Physics (McGraw-Hill, New York, 1953).

[108] G. Wunner *et al.*, in Atomic Spectra and Collisions in External Fields, edited by K. Taylor, M. Nayfeh, and C. Clark (Plenum Press, New York, 1988).

[109] L. Perko, Differential Equations and Dynamical Systems (Springer-Verlag, New York, 1996).

[110] B. H. Bransden and C. J. Joachain, Physics of atoms and molecules (Longman Group Limited, Essex, 1983).

[111] E. P. Wigner, Phy. Rev. **70**, 15 (1946).

[112] E. P. Wigner, Phys. Rev. **70**, 606 (1946).

[113] E. P. Wigner and L. Eisenbud, Phys. Rev. **72**, 29 (1947).

[114] M. Danos and W. Greiner, Phys. Rev. **146**, 708 (1966).

[115] U. Fano and C. M., Phys. Rev. Lett. **31**, 1573 (1973).

[116] C. H. Greene, in Fundamental Processes of Atomic Dynmics, edited by J. Briggs, H. Kleinpoppen, and H. Lutz (Plenum, Plenum, 1988), p. 105.

[117] W. Kohn, Phys. Rev. **74**, 1763 (1948).

[118] C. de Boor, A Practical Guide to Splines (Springer, New York, 1978).

[119] J. Sapirstein and W. R. Jonhson, J. Phys. B **29**, 5213 (1996).

[120] D. A. Varshalovich, A. N. Moskalev, and V. K. Khersonskii, Quantum Theory of Angular Momentum (World Scientific, Singapore, 1988).

[121] E. Anderson *et al.*, LAPACK Users Guide (SIAM, Philadelphia, 1999).

[122] W. H. Miller, Advan. Chem. Phys. **25**, 69 (1974).

[123] J. M. Rost, Phys. Rev. Lett. **72**, 1998 (1994).

[124] J. M. Rost, Phys. Rep. **297**, 271 (1998).

[125] R. A. Jalabert, H. U. Baranger, and A. D. Stone, Phys. Rev. Lett. **65**, 2442 (1990).

[126] W. A. Lin and J. B. Delos, Chaos **3**, 655 (1993).

[127] H. U. Baranger, R. A. Jalabert, and A. D. Stone, Chaos **3**, 665 (1993).

[128] C. D. Schwieters, J. A. Alford, and J. B. Delos, Phys. Rev. B **54**, 10652 (1996).

[129] L. Wirtz, J. Tang, and J. Burgdörfer, Phys. Rev. B **56**, 7589 (1997).

[130] R. Landauer, J. Res. Dev. **1**, 223 (1957).

[131] A. G. Magner, V. M. Kolomietz, and V. M. Strutinskii, Sov. J. Nucl. Phys. **28**, 764 (1979).

[132] S. C. Creagh, J. Phys. A **26**, 95 (1993).

[133] S. C. Creagh and R. G. Littlejohn, Phys. Rev. A **44**, 836 (1991).

[134] J. A. Shaw, J. B. Delos, M. Courtney, and D. Kleppner, Phys. Rev. A **52**, 3695 (1995).

[135] A. M. Ozorio de Almeida, Hamiltonian systems: chaos and quantization (Cambridge University Press, New York, 1988).

[136] J. Gao, J. B. Delos, and M. Baruch, Phys. Rev. A **46**, 1449 (1992).

[137] H. Held, J. Schlichter, G. Raithel, and H. Walther, Europhys. Lett. **43**, 392 (1998).

[138] H. Hasegawa, S. Adachi, and H. Harada, J. Phys. A **16**, L503 (1983).

[139] H. Goldstein, Classical Mechanics, 2nd ed. (Addison-Wesley, Reading, MA, 1980).

[140] H. Friedrich and D. Wintgen, Phys. Rep. **183**, 37 (1989).

[141] R. V. Jensen *et al.*, Phys. Rev. A **62**, 053410 (2000).

[142] J. M. Mao, J. Shaw, and J. B. Delos, J. Stat. Phys. **68**, 51 (1992).

[143] R. G. Littlejohn, J. Math Phys. **31**, 2952 (1990).

Appendix A

Scaled variables for diamagnetic hydrogen

Scaled variables are an important part of the study of atoms in external fields. These transformations lead to numerical efficiencies and conceptual simplifications. This Appendix gives the relevant transformations for the case of an atomic electron in a static magnetic field. These results are well known and are collected in a number of articles besides this Appendix [138, 35, 39].

To begin with, the classical Hamiltonian for an atomic electron in a static magnetic field applied along the z-axis is:

$$H = \frac{1}{2}\left(p_\rho^2 + p_z^2\right) + \frac{L_z^2}{2\rho^2} - \frac{1}{r} + \frac{1}{2}BL_z + \frac{1}{8}B^2\rho^2, \tag{A.1}$$

As always, I use atomic units ($e = \hbar = m = 1$) so that the magnetic field strength is $B = B(\text{Tesla})/2.35\times 10^{-5}$. This Hamiltonian neglects the spin of the electron, relativistic effects, and the finite mass of the nucleus. Of course, the classical equations of motion are given by Hamilton's equations [139]:

$$\dot{\vec{x}} = \frac{\partial H(\vec{x},\vec{p})}{\partial \vec{p}}, \tag{A.2}$$

$$\dot{\vec{p}} = -\frac{\partial H(\vec{x},\vec{p})}{\partial \vec{x}}. \tag{A.3}$$

Once these equations have been solved (see Appendix B) to give the orbit $(\vec{x}(t),\vec{p}(t))$, the classical action is simply,

$$S(\vec{x},\vec{x}') = \int_{\vec{x}'}^{\vec{x}} \vec{p}'' \cdot d\vec{x}''. \tag{A.4}$$

With the Hamiltonian of Eq. (A.1) the classical action S and period T of the electron depend on both the energy E and magnetic field strength B. Scaled variables reduce this dependence to a single parameter,

the scaled energy ϵ. The scaled variables are defined by the relations,

$$w = 2\pi B^{-1/3} \tag{A.5}$$

$$\epsilon = EB^{-2/3} = E\left(\frac{w}{2\pi}\right)^2 \tag{A.6}$$

$$\tilde{x} = xB^{2/3} = x\left(\frac{2\pi}{w}\right)^2 \tag{A.7}$$

$$\tilde{p} = pB^{-1/3} = p\left(\frac{w}{2\pi}\right) \tag{A.8}$$

$$\tilde{L}_z = L_z B^{1/3} = L_z\left(\frac{2\pi}{w}\right). \tag{A.9}$$

When these scaled variables (A.5-A.9) are used to transform the Hamiltonian, Eq. (A.1), and the equations of motion, Eqs. (A.2) and (A.3), it is seen that both the time t and action S must be rescaled as well:

$$\tau = t/B, \tag{A.10}$$

$$\tilde{S} = S/w. \tag{A.11}$$

This ensures that the scaled equations of motion for $(\tilde{x}(t), \tilde{p}(t))$ can be derived from the scaled Hamiltonian,

$$\tilde{H} = \epsilon = \frac{1}{2}\left(\tilde{p}_z^2 + \tilde{p}_\rho^2\right) + \frac{\tilde{L}_z^2}{2\tilde{\rho}^2} - \frac{1}{\tilde{r}} + \frac{\tilde{L}_z}{2} + \frac{1}{8}\tilde{\rho}^2, \tag{A.12}$$

using Hamilton's equations (A.2) and (A.3) (but now with scaled variables everywhere). The most important feature of this scaling transformation is that the scaled Hamiltonian, Eq. (A.12), depends only on the scaled energy ϵ and not the scaled magnetic field w. This implies that the scaled action (A.11),

$$\tilde{S}(\tilde{x}, \tilde{x}') = \frac{1}{2\pi}\int_{\tilde{x}'}^{\tilde{x}} \tilde{p}'' \cdot d\tilde{x}'', \tag{A.13}$$

depends only on the scaled energy ($\tilde{S} = \tilde{S}(\epsilon)$) as well. Thus, when photoabsorption spectra are measured or calculated at a fixed scaled energy ϵ as a function of w, the classical dynamics of the electron remains the same for all values of w. Once a set of classical closed orbits has been calculated at a given value of ϵ, those same orbits can be used to construct the semiclassical S-matrix of Ch. 4 at any value of w.

The scaled energy ϵ alone, then, controls the degree to which the classical dynamics are regular or chaotic. The transition to global chaos for the scaled Hamiltonian, Eq. (A.12), has been studied in depth

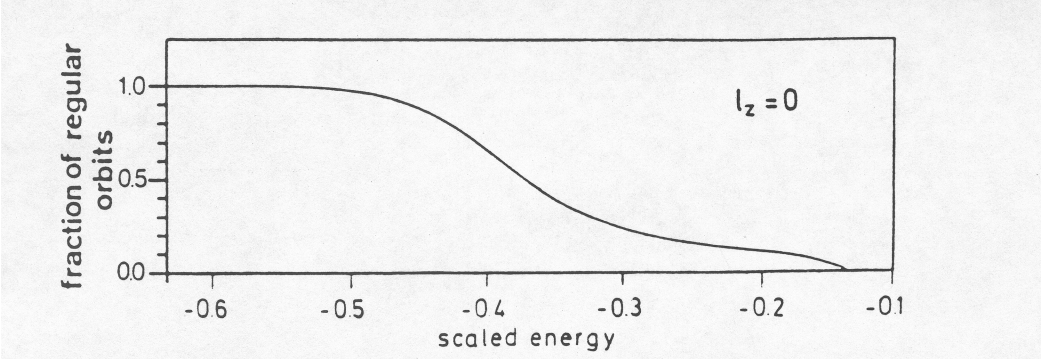

Figure A.1: The fraction of classical phase space that is regular for diamagnetic hydrogen is plotted as a function of the scaled energy $\epsilon = EB^{-2/3}$. As the scaled energy approaches zero from below, the classical dynamics evolve from being regular ($\epsilon < -0.5$) to being globally chaotic ($\epsilon > -0.15$). This graph is taken from [140].

by a number of researchers [39, 60, 61]. An excellent review of the subject can be found an the article by Friedrich and Wintgen [140]. A qualitative picture of the effects of changing ϵ can be gained by looking at the fraction of classical phase space having regular dynamics (vanishing Lyapounov exponent). Figure A.1 shows this fraction as a function of the scaled energy ϵ. At low scaled energies ($\epsilon < -0.5$) almost all of phase space exhibits regular dynamics. As the scaled energy is increased from $\epsilon = -0.5$ to $\epsilon \approx -0.15$ the fraction of regular phase space gradually approaches zero. Finally, above $\epsilon = -0.15$, the Hamiltonian is globally chaotic. This classical transition from regular to chaotic behavior in diamagnetic hydrogen is important to keep in mind when viewing scaled recurrence spectra of the system.

While the scaled magnetic field w is not relevant to the classical dynamics of diamagnetic hydrogen, its significance can be seen by exploring the effect of the scaling transformation Eqs. (A.5-A.11) on the Schrödinger equation. The scaled Schrödinger equation for the diamagnetic Hamiltonian (A.1) reads:

$$\left(\frac{1}{2}\left(\frac{2\pi\hbar}{w}\right)^2 \nabla^2_{\tilde{x}} + \epsilon - \frac{1}{\tilde{r}} - \frac{\tilde{L}_z}{2} - \frac{1}{8}\tilde{\rho}\right)\psi(\tilde{x}) = 0. \tag{A.14}$$

This shows that the combination $2\pi\hbar/w$ can be viewed as an effective Plank's constant,

$$\hbar_{eff} = \frac{2\pi\hbar}{w}, \tag{A.15}$$

whose value can be tuned by changing the scaled magnetic field w. This provides a convenient method

of studying the passage from the quantum mechanical ($\hbar_{eff} \approx 1$ in a.u.) to the classical ($\hbar_{eff} \to 0$) world. As a note, for most of the calculations in this thesis, w is in the range $100 - 500$ a.u. so that $\hbar_{eff} = 0.06283 - 0.01257$.

Two limitations of scaled variables are worth mentioning at this point. First, because photoabsorption experiments are done at fixed values of L_z (rather than $\tilde{L}_z$), the scaled classical Hamiltonian, Eq. (A.12), is independent of w only for the specific case $L_z = 0$. When $L_z \neq 0$ the terms representing the centrifugal potential and the linear Zeeman effect destroy the simple scaling laws that exist for the $L_z = 0$ case. Because most experiments to date have studied the $L_z = 0$ case, this breakdown of the classical scaling has not been addressed in depth. One notable exception to this has been the recent experimental study of $L_z = 1$ states of helium in a static electric field [65, 141]. The main lesson learned so far is that the nonscaling terms in the Hamiltonian, Eq. (A.12), become unimportant in the classical limit ($\hbar_{eff} = 2\pi/w \to 0$).

Another scenario for which the classical equations of motion depend on both the scaled energy ϵ and the scaled field w is when the ionic core is something other than hydrogen. This introduces additional short range ion-electron interactions that, in general, do not obey simple scaling relationships. However, the classical scaling laws still hold in the long-range region where the core effects can be neglected. This, combined with the weak energy dependence of the electron-ion interaction (contained in $\underline{S}^{\text{core}}$) preserves the usefulness of scaled variables for lighter nonhydrogenic atoms. That is, even though the classical dynamics of a diamagnetic electron in a one electron atom depends on the scaled field w, this dependence is weak and can often be neglected. However, in heavier multichannel atoms with multiple ionization thresholds, the usefulness of scaled variables is more questionable and must be studied carefully.

Appendix B

A survey of classical closed orbits in diamagnetic hydrogen

The methods and techniques for calculating the closed orbits for diamagnetic hydrogen are well documented in the literature [37, 38, 39]. Because I use the same approach as others, the following just presents a brief summary of the method adopted to calculate the closed orbits needed for the semiclassical approximations of the long-range S-matrix.

The main difficulty one encounters in integrating the equations of motion for the Hamiltonian of diamagnetic hydrogen, Eq. (A.12), is the Coulomb singularity at the origin. As a classical electron approaches the origin, its velocity becomes infinite, which necessitates the use of arbitrarily fine time steps in a numerical integration of the classical equations of motion. This difficulty is handled easily by the use of scaled semiparabolic coordinates [39]. These coordinates are defined in terms of the scaled radius $\tilde{r}$ and polar angle θ of spherical polar coordinates:

$$\tilde{u} = \sqrt{\tilde{r}(1+\cos\theta)}, \tag{B.1}$$

$$\tilde{v} = \sqrt{\tilde{r}(1-\cos\theta)}. \tag{B.2}$$

The scaled diamagnetic Hamiltonian, Eq. (A.12), in these coordinates reads,

$$\tilde{H} \equiv 2 = \frac{1}{2}\left(\tilde{p}_u^2 + \tilde{p}_v^2\right) - \epsilon\left(\tilde{u}^2 + \tilde{v}^2\right) + \frac{1}{8}\tilde{u}^2\tilde{v}^2\left(\tilde{u}^2 + \tilde{v}^2\right) + \frac{\tilde{L}_z^2}{2\tilde{u}^2\tilde{v}^2}\left(\tilde{u}^2 + \tilde{v}^2\right), \tag{B.3}$$

where the scaled time τ, Eq. (A.10), has been rescaled to the variable τ' according to the relation:

$$\frac{d\tau'}{d\tau} = \frac{1}{(\tilde{u}^2 + \tilde{v}^2)}. \tag{B.4}$$

This transformation of time, along with the fixed pseudoenergy of the Hamiltonian ($\tilde{H} = 2$) ensures that the equations of motion for the variables ($\tilde{u}, \tilde{v}, \tilde{p}_u, \tilde{p}_v$) are Hamiltonian in structure. In these coordinates the Hamiltonian corresponds to two harmonic oscillators coupled by a quartic potential term. Because the singularities of the Coulomb potential have been removed from the Hamiltonian, Eq. (B.3), the equations of motion for ($\tilde{u}, \tilde{v}, \tilde{p}_u, \tilde{p}_v$) can be integrated with a standard fourth-order Runge-Kutta integration. I have found that a fixed step size $\Delta\tau' = 0.001$ gives an energy that is conserved to eight significant figures.

Using these coordinates, the closed orbits can be found in a straightforward manner. I launch classical trajectories radially outward from a sphere $\tilde{r} = 0.001$ at a scaled energy ϵ for a range of initial polar angles θ_i. At some later point, the orbits return to the sphere with various values of the scaled angular momentum $\tilde{p}_\theta$. The closed orbits that return radially are then found numerically as the roots of the equation:

$$\tilde{p}_\theta(\theta_i) = 0. \tag{B.5}$$

Once the initial θ_i and final θ_f polar angles of the closed orbits have been found, the quantities needed for the semiclassical S-matrix are calculated. The scaled action $\tilde{S}$ is given as the integral,

$$\tilde{S} = \frac{1}{2\pi} \int \tilde{\tilde{p}}_u d\tilde{u} + \tilde{p}_v d\tilde{v},$$

along each trajectory. The semiclassical amplitude,

$$A = \frac{2\pi}{w}\tilde{A} = \frac{2\pi}{w} \left. \frac{\partial \theta_i}{\partial \tilde{p}_{\theta_f}} \right|_{\tilde{p}_{\theta_i}=0},$$

is calculated numerically by launching nearby trajectories with slightly different initial angles. Finally, the Maslov index μ is calculated using the method described by Mao *et al.* [142]. As Du and Delos [37, 38] first reported, a general rule of thumb can be given for finding the Maslov index of the closed orbits. The rule is this: μ increments by one every time the orbit crosses the z-axis or passes through a turning point in the ρ direction. Except for a few special cases, such as for repetitions of the closed orbits, this rule gives the Maslov indices accurately. For the repetitions, the winding number of the classical trajectory must be tracked along each trajectory to find the Malsov index correctly. More detailed information about how this is handled in general can be found in [142].

When interpreting the recurrences of the long-range S-matrix and the photoabsorption cross section, it is useful to have an idea of the closed orbits that contribute at a given scaled energy ϵ. As a general reference, Fig. B.1 shows the scaled actions $\tilde{S}$ of classical closed orbits for a range of scaled energies from $\epsilon = -0.4 \rightarrow 0.0$. The scaled action of $\epsilon = -0.3$, where most of my semiclassical calculations are performed, is shown by a dashed line. Furthermore, the shapes of some of the orbits at this scaled energy, along with their scaled actions, are shown in Fig. B.2. These two figures provide a useful resource when assigning closed orbits to recurrence peaks.

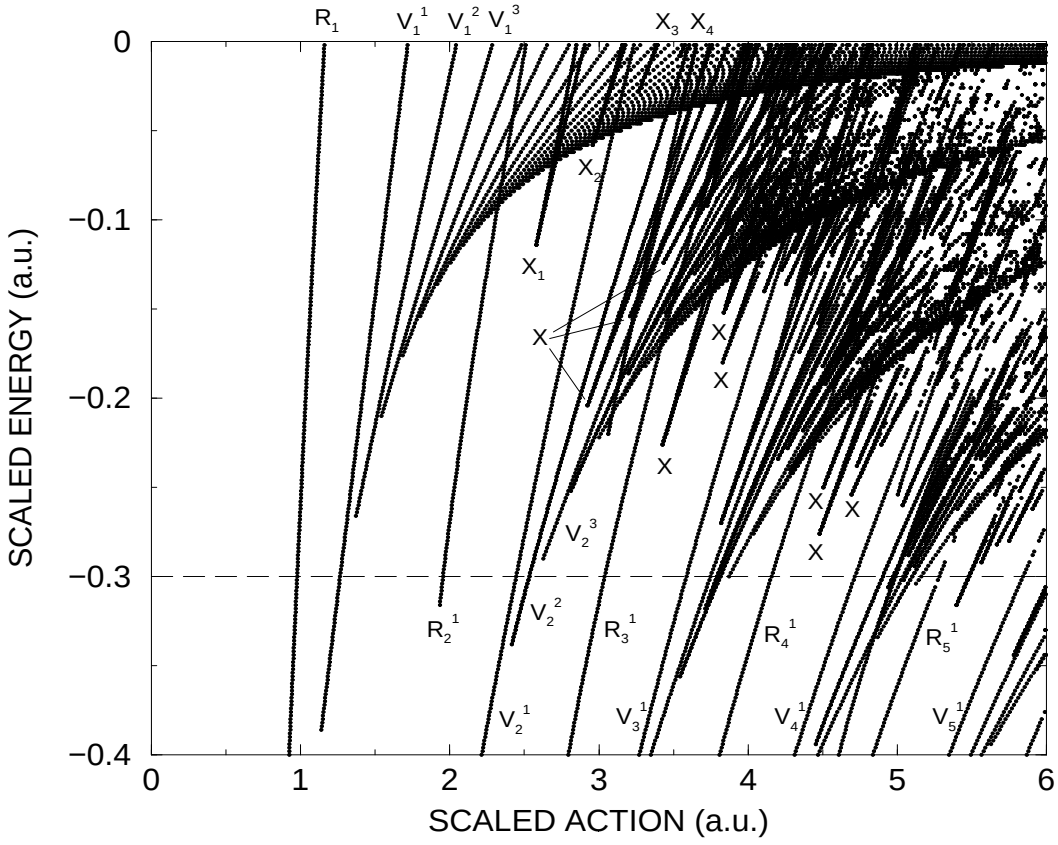

Figure B.1: The scaled actions $\tilde{S}$ of classical closed orbits of diamagnetic hydrogen are plotted as a function of the scaled energy ϵ. As the scaled energy increases, new orbits bifurcate into existence. By the time the scaled energy has reached $\epsilon = 0$, the classical dynamics are globally chaotic and there are infinitely many closed orbits. The labeling scheme used here follows that of Welge's group [35]. Three classes of orbits are identified. First, the rotators (R_n^k) are orbits that bifurcate out of the nth repetition of the orbit perpendicular to the magnetic field R_1, the so called quasi-Landau orbit. Likewise, the vibrators (V_n^k) bifurcate out of the nth repetition of the orbit parallel to the magnetic field, the so called parallel orbit. In both of these cases, the superscript k denotes which bifurcation of the nth repetition that has occurred. Thus, the label V_2^3 denotes the third bifurcation of the second repetition of the parallel orbit. The third class of orbits are the so called exotic orbits and are labeled by X. The bifurcations of these orbits occur in isolation from other orbits through saddle node bifurcations. There is a variety of labeling schemes for these orbits. I choose to simple label the first few sequentially ($X_1, X_2, X_3, \ldots$).

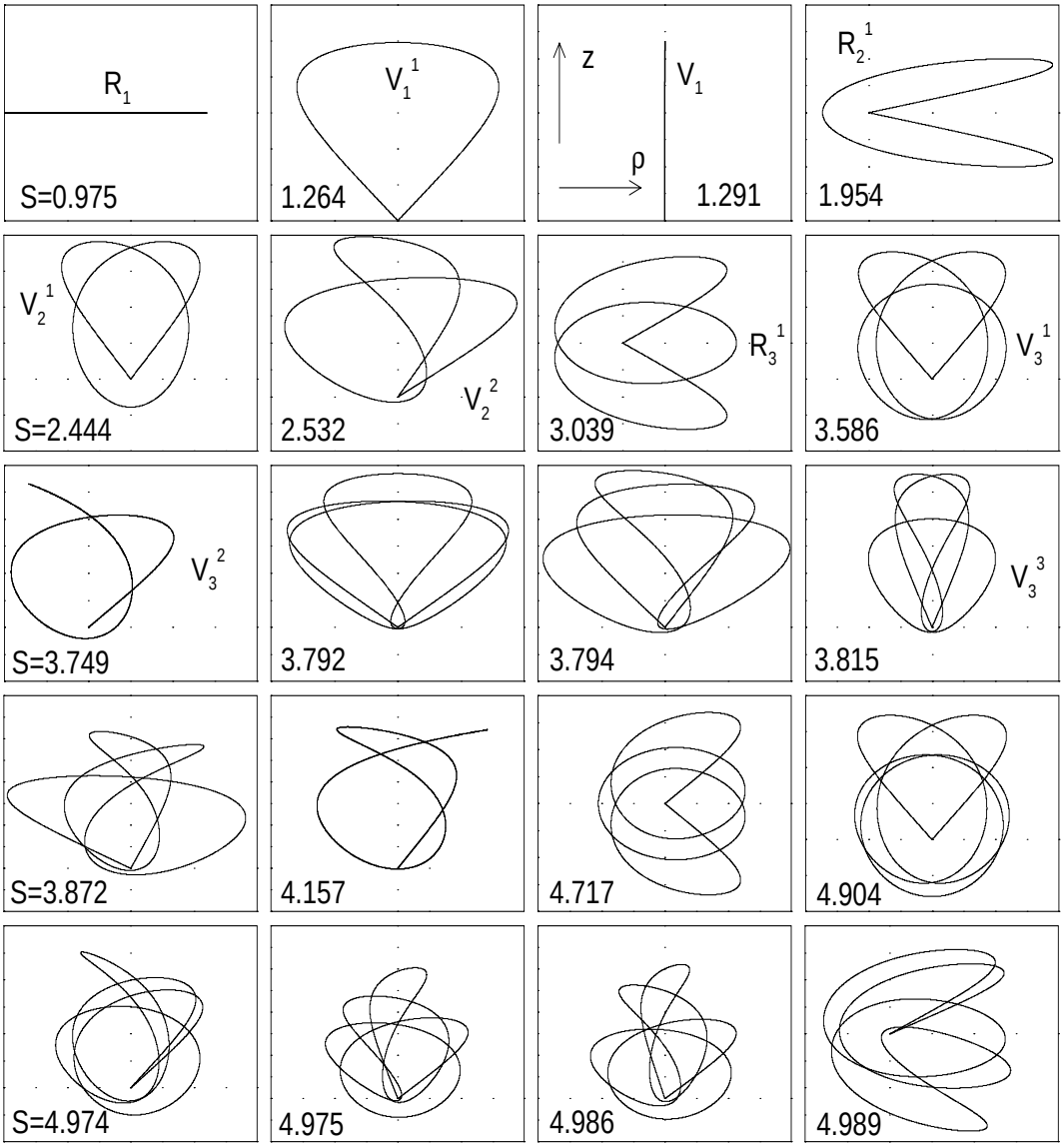

Figure B.2: The first 20 closed orbits of diamagnetic hydrogen are shown at a scaled energy of $\epsilon = -0.3$. The orbits are plotted in cylindrical coordinates (ρ, z) allowing ρ to become negative when an orbit crosses the z-axis. At this scaled energy, approximately 80% of the classical phase space is chaotic. The scaled actions of each orbit are shown as a number in each frame along with its label $(R_1, V_1, V_1^1, \ldots)$.

Appendix C

Semiclassical Green's function amplitude

In Ch. 5, the semiclassical Green's function of Gutzwiller [20, 21, 22] was used to calculate the semiclassical approximation to the long range S-matrix. This Green's function involves a two dimensional Jacobian determinant that measures the stability of the classical orbits contributing to the Green's function. Many of the properties and manipulations of this stability amplitude are subtle and difficult. With this in mind, this Appendix describes some of the simplifications and manipulations of the semiclassical amplitude used in this thesis. For more details on the properties of the semiclassical Green's function, the texts of Brack and Bhaduri [24] and also of Reichl [23] are invaluable. An article by Littlejohn [143] gives a complete, but more mathematical, analysis of the amplitudes described here.

The amplitude of the two-dimensional, semiclassical Green's function, Eq. (5.17), is:

$$|D| = \left| \frac{\partial(p'_\rho, p'_z, t)}{\partial(\rho, z, E)} \right| = \begin{vmatrix} \frac{\partial p'_\rho}{\partial \rho} & \frac{\partial p'_\rho}{\partial z} & \frac{\partial p'_\rho}{\partial E} \\ \frac{\partial p'_z}{\partial \rho} & \frac{\partial p'_z}{\partial z} & \frac{\partial p'_z}{\partial E} \\ \frac{\partial t}{\partial \rho} & \frac{\partial t}{\partial z} & \frac{\partial t}{\partial E} \end{vmatrix} . \tag{C.1}$$

Here and throughout this Appendix, the vertical bars $||$ denote the absolute value of the determinant. The coordinates (ρ, z) and conjugate momenta (p_ρ, p_z) are the standard cylindrical coordinates. It can be shown that the two-by-two subdeterminant in the upper left hand corner of Eq. (C.1) vanishes [24]:

$$\begin{vmatrix} \frac{\partial p'_\rho}{\partial \rho} & \frac{\partial p'_\rho}{\partial z} \\ \frac{\partial p'_z}{\partial \rho} & \frac{\partial p'_z}{\partial z} \end{vmatrix} = 0. \tag{C.2}$$

This is a general property of the semiclassical amplitude that holds in any coordinate system as a consequence of energy conservation. To take this vanishing subdeterminant into account, the derivative $\partial t / \partial E$

in Eq. (C.1) can be set to zero (although it is finite) without consequence.

In addition, a more symmetric form of Eq. (C.1) can be achieved by using the relations:

$$\frac{\partial p'_\rho}{\partial E} = -\frac{\partial^2 S}{\partial E \partial \rho'} = -\frac{\partial t}{\partial \rho'} = -\frac{1}{\dot{\rho}'}, \tag{C.3}$$

$$\frac{\partial p'_z}{\partial E} = -\frac{\partial^2 S}{\partial E \partial z'} = -\frac{\partial t}{\partial z'} = -\frac{1}{\dot{z}'}. \tag{C.4}$$

Then the amplitude $|D|$, Eq. (C.1), reads:

$$|D| = \begin{vmatrix} \frac{\partial p'_\rho}{\partial \rho} & \frac{\partial p'_\rho}{\partial z} & -\frac{1}{\dot{\rho}'} \\ \frac{\partial p'_z}{\partial \rho} & \frac{\partial p'_z}{\partial z} & -\frac{1}{\dot{z}'} \\ \frac{1}{\dot{\rho}} & \frac{1}{\dot{z}} & 0 \end{vmatrix} = \left| -\frac{1}{\dot{\rho}} \left(\frac{\partial p'_\rho}{\partial z} \frac{1}{\dot{z}'} - \frac{\partial p'_z}{\partial z} \frac{1}{\dot{\rho}'} \right) + \frac{1}{\dot{z}} \left(\frac{\partial p'_\rho}{\partial \rho} \frac{1}{\dot{z}'} - \frac{\partial p'_z}{\partial \rho} \frac{1}{\dot{\rho}'} \right) \right| \tag{C.5}$$

Littlejohn [143] has shown that this derivative can be simplified further. This final simplification leads to the form of the amplitude used in Eq. (5.19) to derive the long range S-matrix of Ch. 5. Using energy conservation and various partial derivatives of the Hamiltonian, Littlejohn simplifies the amplitude $|D|$ of Eq. (C.5) into a form that involves the velocity in one direction and a simple partial derivative in the other direction. Two such forms can be derived, corresponding to separating out the velocity in the ρ direction,

$$|D| = \left| \frac{1}{\dot{\rho}} \frac{1}{\dot{\rho}'} \right| \left| \frac{\partial p'_z}{\partial z} \right|_{z'}, \tag{C.6}$$

or in the z direction,

$$|D| = \left| \frac{1}{\dot{z}} \frac{1}{\dot{z}'} \right| \left| \frac{\partial p'_\rho}{\partial \rho} \right|_{\rho'}. \tag{C.7}$$

Although it is not obvious, these two forms of the amplitude $|D|$ are identical. In fact, Littlejohn shows that the velocity in **any** direction can be separated out. Thus when spherical polar coordinates (r, θ) are used, the semiclassical amplitude takes the form:

$$|D| = \left| \frac{1}{\dot{r}\dot{r}'} \right| \left| \frac{\partial p'_\theta}{\partial \theta} \right|_{\theta'} \tag{C.8}$$

This form (C.8) of the amplitude appears in the semiclassical Green's function, Eq. (5.19), used to derive the semiclassical approximation to $\underline{S}^{\mathrm{LR}}$.

Appendix D

Related publications

- "Extending closed-orbit theory using quantum-defect ideas: Basic concepts and derivations," B. E. Granger, C. H. Greene, Phys. Rev. A **62**, 012511 (2000).
- "Quantum and semiclassical analysis of long-range Rydberg molecules," B. E. Granger, E. L. Hamilton, C. H. Greene, Phys. Rev. A (in press).